MID-LATITUDE IONOSPHERIC IRREGULARITIES DEDUCED FROM SPACED-RECEIVER SCINTILLATION MEASUREMENTS

by

Hiroshi KUMAGAI

March 1988

Radio Research Laboratory

Koganei, Tokyo, Japan

MID-LATITUDE IONOSPHERIC IRREGULARITIES DEDUCED FROM SPACED-RECEIVER SCINTILLATION MEASUREMENTS

by

Hiroshi KUMAGAI

March 1988

Radio Research Laboratory

Koganei, Tokyo, Japan

ACKNOWLEDGMENTS

The author wishes to express his hearty and sincere gratitude to Professor Iwane Kimura of Kyoto University for his guidance and supervision throughout the work.

The author is deeply indebted to Professor Noboru Wakai, Tohkai University, the former Director General of Radio Research Laboratory, and to Dr. Kenji Sinno, the former Associate Director General of Radio Research Laboratory for their continual guidance and encouragement.

The author also would like to express his hearty appreciation to Drs. Nobuyoshi Fugono, Shigeru Miyazaki, and Mr. Tsuyoshi Ishimine for their useful advice and encouragement.

The author is grateful to the late Mr. Choshichi Ouchi for his useful comments and guidance.

The author is indebted to the staff of the National Space Development Agency of Japan for their ETS-2 satellite control and operations.

The author also wishes to acknowledge Mr. Hisamitsu Minakoshi, and Drs. Tadahiko Ogawa and Sigeo Ito for their stimulating suggestions, discussions, and co-works.

Thanks are also due to Messrs. Susumu Isozaki, Koji Ohbu, Eiji Ouchi, Takeshi Isobe, and Toshihiro Hori, who were engaged in the installation of the experimental system and observation.

All the computations were made by the ACOS-850 system in

Radio Research Laboratory.

PREFACE

Studies of ionospheric scintillations appearing on satellite radiowaves have been continued for a long time, and have contributed to developments of the physics of ionospheric irregularities, evaluation of performance of satellite communication links, and so on. From a theoretical point of view, observational data of scintillations have been quite useful to construct more complete theory of electromagnetic wave scatterings from random media.

The present thesis deals with observations and analyses of the mid-latitude ionospheric scintillations of VHF satellite radiowave. The former half of the thesis is devoted to both the observation of mid-latitude ionospheric scintillations by means of spaced-receivers and the investigation of spatial structures of the ionospheric irregularities causing scintillations. In the latter half, an interpretation of observational results is presented by using a strong scattering theory, and also a comparison between observational and theoretical results is made to construct a scintillation model.

In Chapter 2, analysis method of scintillation data obtained by spaced-receivers is described. This method, so called the correlation analysis, was developed in the 1950's and 1960's. Through this analysis, various informations of spatial structures such as shape, size and movement of the irregularities are

obtained. Then, the experimental setup at the Hiraiso Branch of the Radio Research Laboratory, and the observation and data processing technique are presented.

Observational results of the spatial structures of the irregularities are described in Chapter 3. From observations under geomagnetically quiet conditions, it is confirmed that the irregularities causing nighttime scintillation are well elongated along the geomagnetic lines of force at F-region height. Mean axial ratio and minor radius of them are 24 and 180 m, respectively. With increasing in S_4 index, the axial ratio increases while the minor radius decreases, suggesting that multiple scattering plays an important role in the production of intense scintillations. During a geomagnetic storm, much faster drift velocities and larger spectral indices of the scintillation spectra are obtained, which suggests stronger ionospheric electric fields and highly-structured irregularities.

In Chapter 4, the fourth-order moment equation is numerically solved to apply to ionospheric scintillation problem. With the aid of this computation, observational results obtained in intense scintillation regime are successfully interpreted. It is confirmed that the decrease in transverse correlation distance (minor radius) with increasing scintillation intensity is caused by the effect of multiple scattering. Finally, models of ionospheric irregularities and frequency dependence of scintillation intensity, which are valid for intense

scintillations, are offered.

CONTENTS

CHAPTER 1

GENERAL INTRODUCTION

1.1. IONOSPHERIC SCINTILLATION PHENOMENA OF SATELLITE RADIOWAVES

Irregular fluctuations, called scintillations, of amplitude, phase, and angle of arrival are sometimes observed on radiowaves propagating through the ionosphere. Scintillations are considered to be caused by the irregular electron density distribution (ionospheric irregularities) formed in the ionosphere. Among these scintillations, the amplitude scintillations have been most widely studied. Originally, ionospheric scintillations were observed and investigated using radiowaves from radio stars in HF and VHF bands. The advent of various artificial satellites has allowed to collect world-wide data of the scintillations in a wide frequency range from VHF to microwave band. Since the ionospheric effect upon radiowave propagation is more remarkable at lower frequencies, scintillations appear most frequently and intensely in HF band and are rare at frequencies above the microwave band. Nevertheless, recent observations have found the ionospheric scintillations at frequencies above 10 GHz [Ogawa et al., 1980].

From a global point of view, there are three major sectors

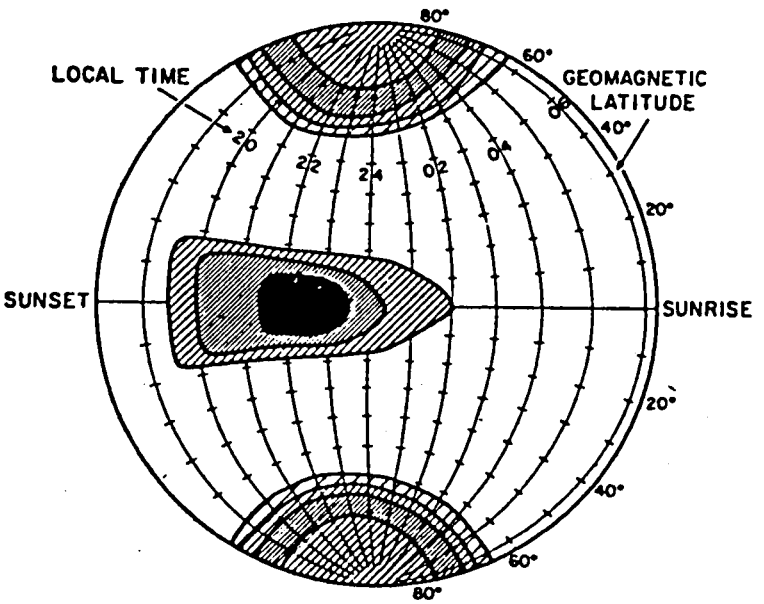

Fig. 1.1. Global distribution of scintillation occurrence (after Aarons, 1982).

of scintillation activity [Aarons, 1982]. Global distribution of the ionospheric scintillation occurrence is shown in Figure 1.1, in which higher activity appears in both the equatorial and high-latitude regions. The equatorial region has been defined, for the purpose of describing the scintillation, within the area in $\pm 20°$ wide around the dip equator, and the high-latitude region with geomagnetic latitudes of more than $\pm 60°$. In mid-latitudes, the area other than those mentioned above, the scintillation activity has been known to be less intense. In all sectors, there is a pronounced nighttime maximum.

In the equatorial region, the range type spread-F on ionogram is well correlated with the scintillation activity. This fact confirms that scintillation is produced by the electron density irregularities formed at the F-region height. The equatorial scintillation and/or spread-F start to occur after the sunset, and the peak occurrences of them appear in the premidnight hours. The activity in the postmidnight hours are weaker than that in the premidnight hours. Recent radar observations and theories have revealed that nighttime ionospheric irregularities in the equatorial region emerging after the sunset start to develop from the bottomside of the F-region probably through the Rayleigh-Taylor plasma instability mechanism [Basu and Kelley, 1979]. The plume-like irregularities developing from secondary plasma instabilities associated with the depleted density region, called plasma bubble, rise into the

region above the peak of the F2 layer. Steep gradients on the edges of the bubble help to generate the plume-like small scale irregularities which produce scintillations.

The other pronounced feature for the equatorial scintillation is that the annual occurrence shows a clear longitudinal dependence [Aarons et al., 1980]. In the American and Atlantic zones, the maximum occurrence appears in winter or spring (November-April) in the northern hemisphere and the minimum in summer (May- July) while, in the Pacific zone, the maximum occurs in summer and the minimum in winter. Scintillation occurrence shows a positive correlation with solar activity. The correlation between geomagnetic activity and scintillation activity shows a somewhat complex feature; increased magnetic activity inhibits scintillation activity before midnight except during those months with very low scintillation activity. After midnight, scintillation activity generally increases slightly with the presence of magnetic storms [Aarons, 1982].

Mid-latitude scintillation activity is not so intense as that in the equatorial and high-latitude regions. Therefore, attention has not been paid so much to the mid-latitude scintillations, and thus both the morphology and mechanism of them remain unsolved. A difficulty in describing the mid-latitude scintillation activity stems from that what takes place at mid-latitudes may be an extension of phenomena at equatorial and/or auroral latitudes. In fact, the scintillations observed around

Japan have features somewhat similar to those appearing in the equatorial regions [Kumagai, 1986]. For example, annual scintillation occurrence pattern and the geomagnetic activity dependence in the mid-latitude regions are almost similar to those in the equatorial regions. A correlation between the scintillation occurrence and the spread-F also has been pointed out in the mid-latitude regions [Sinno and Kan, 1980]. At higher mid-latitude, invasion of the auroral region toward the mid-latitude was observed depending on solar activity and geomagnetic activity [Aarons, 1982].

Apart from the effects spreading from the equatorial and auroral regions, localized mid-latitude plasma instabilities can generate scintillations. Possible instabilities are the gradient drift instability [Costa and Kelley, 1978; Basu et al., 1981] and the so-called Perkins instability [Perkins, 1973; Behnke, 1979]. Temporal fluctuations of the neutral atmosphere such as medium-scale gravity waves may be another cause of mid-latitude irregularities [Kersley et al., 1980].

Another factor being considered in the mid-latitude scintillation morphology is the effect of sporadic-E, which produces scintillation [Das Gupta and Kersley, 1976; Sinno and Kan, 1980]. The behavior of sporadic-E is completely different from the morphology of F-region irregularities. Sporadic-E at mid-latitude shows a high occurrence during daytime, which results in a second maximum of daily scintillation occurrence.

High-latitude scintillations appear in the auroral and polar cap regions. Energetic electron precipitations and current systems can be dominant factors in producing the ionospheric irregularities in these regions [Aarons, 1982]. The seasonal variation of auroral zone scintillation is not clear. It was reported that the low-latitude boundary of auroral scintillations can be extended equatorward under geomagnetically disturbed conditions [Rino and Matthews, 1980].

1.2. APPLICATIONS OF SCINTILLATION STUDY

Results of ionospheric scintillation study have been applied to the fields covering both science and engineering. In this section, after three applications of the scintillation study are outlined, the objectives of the present study are described.

First, scintillation observation makes possible to study the dynamics of ionospheric irregularities. Experimental techniques for studying the ionospheric irregularities can be grouped into two categories: remote sensing technique and in-situ technique. Among a variety of remote sensing techniques, the scintillation measurement requires relatively simple and cheap instrument. Since the radiowave coming through the ionosphere contains information of irregularities at various heights, many parameters of the irregularities such as intensity of density fluctuations,

scale size, and movement of the irregularities can be obtained through the analysis of received radiowave. Irregularity scale sizes mostly effective to create scintillation are around the sizes of the first Fresnel zone, which vary depending on the radiowave frequency and the height of irregularities. Typical values of them are about 1 km at 136 MHz and 200 m at 4 GHz for the F-region irregularities. These values are larger than the scale sizes being explored by incoherent scatter radar and ionosonde observations.

Second application of the scintillation study is to evaluate the ionospheric effects on satellite-earth radiowave propagation. [Whitney and Basu, 1977]. It has been reported that during severe scintillation the satellite operation of GMS-2 (Geostationary Meteorological Satellite-2) using a 1.7 GHz link was considerably disturbed [Ueda et al., 1983]. Scintillation data obtained during this event can give information necessary to design the communication link. It is known that the probability distribution of amplitude scintillation shows a good agreement with the Nakagami-m distribution. A Rayleigh distribution appears to describe the severest scintillations [Reddi et al., 1980]. These results make it possible to estimate the fading margin for earth-satellite communication links.

Radio frequency dependence of the scintillation intensity is also an important measure to estimate the effects on earth-satellite links [e.g., Fujita et al., 1982]. Measurement of the

spectral index (n) of scintillation intensity (I(f)) indicates that for weak and moderate scintillations $I(f) \propto f^{-n}$ (f is radio frequency) where n=1-2, while $n \sim 0$ (strong scattering limit) for intense scintillations [Whitney and Basu, 1977]. Apart from the satellite communications described above, highly accurate measurements of amplitude, phase and angle of arrival of satellite radiowaves are required for the purposes of navigation, geodesy, and remote sensing of the sea surface. In these cases, the correction of the ionospheric effects is indispensable. Hereafter, it will become more and more important to evaluate the ionospheric effects on radiowave propagations.

Third application of the scintillation data is to test the existing radiowave propagation theories in random media and to construct a more complete theory. Ionospheric scintillation was first studied theoretically in terms of a thin phase-screen theory [Salpeter, 1967; Cronyn, 1970]. The advance in the study of wave propagation in random media has helped to develop a more refined theory. For weak scintillation, a weak scatter theory is quite well established and experimental verifications of theoretical predictions have been demonstrated in many instances [Barabanenkov et al., 1971]. For strong scintillation, although the theory of strong scattering including multiple scattering effects has made much progress in recent years, there still remains quite a few unresolved problems. One objective of this thesis is to clarify how the present theory can interpret the

observational results of strong scintillations. Through the efforts made in this application, much better understanding of other two applications mentioned above will be obtained.

The former half of the present study deals with the first application item, namely, the behavior and characteristics of mid-latitude ionospheric irregularities. The results obtained there are useful to understand the irregularity physics. The latter half is devoted mainly to the application of third kind. The strong scattering theory of radiowave in random media is applied to the present scintillation observation. Using this theory it is possible to interpret various results observed during the strong scintillation events, which have not been explained by the conventional theories. In addition, through the comparison between the theory and observation, a more complete model of the scintillation and/or ionospheric irregularities is suggested.

1.3. SCINTILLATION THEORIES

1.3.1. Introduction to scintillation theory

Let us start the theoretical approach to the ionospheric scintillation mechanism by setting up the geometry shown in Figure 1.2 [Yeh and Liu, 1982]. A region of random irregular

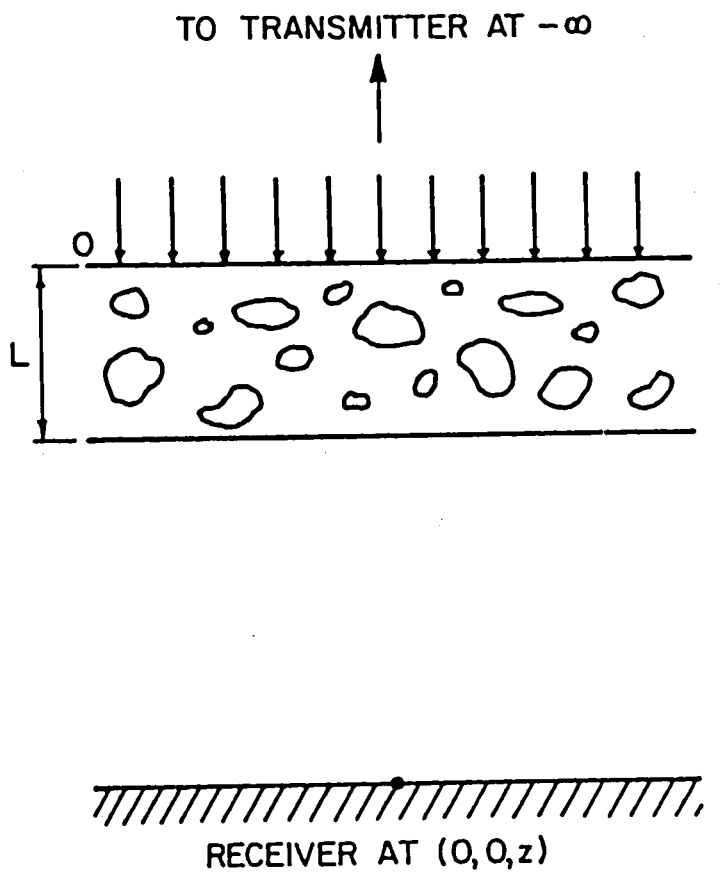

Fig. 1.2. Geometry of ionospheric scintillation problem (after Yeh and Liu, 1982).

electron density structures is located from z=0 to z=L. A time-harmonic electromagnetic wave is incident in the irregular slab at z=0 and is received on the ground. The irregularity slab can be characterized by the electric permittivity as

$$\varepsilon = \langle \varepsilon \rangle \{1 + \varepsilon_1 (\mathbf{r}, t)\} \tag{1.1}$$

where $\mathbf{r}$ denotes the three-dimensional position, $\langle \varepsilon \rangle$ the average dielectric permittivity for the background ionosphere which is given by

$$\langle \varepsilon \rangle = (1 - f_{PO}^2 / f^2)\, \varepsilon_0 \tag{1.2}$$

and $\varepsilon_1(\mathbf{r},t)$ the fluctuating part characterizing random variations caused by the irregularities which is written as

$$\varepsilon_1 = \frac{(f_{PO}/f)^2 \Delta n (\mathbf{r}, t)/n_0}{1 - (f_{PO}/f)^2} \tag{1.3}$$

Here, f_{po} is the plasma frequency corresponding to the background electron density n_o and f is the frequency of the incident radiowave. The temporal variation of $\varepsilon_1(\mathbf{r},t)$, i.e., $\Delta n(\mathbf{r},t)$, is assumed to be much slower than the period of the radiowave.

As the wave propagates through the irregularity slab, to the first order, only the phase is affected by the random fluctuations in the refractive index. Therefore, after the wave has emerged from the random slab, its phase front is randomly

modulated. As this wave propagates toward the ground, the distorted wave front begins to set up an interference pattern resulting in amplitude fluctuations. This diffraction process varies with the size and strength distributions of the irregularities. A simple geometric computation indicates that the major contribution to amplitude scintillations on the ground comes from the irregularities of sizes of the order of $d_F=\sqrt{\lambda(z-L/2)}$ (λ is the wavelength of radiowave), the size of the first Fresnel zone [Briggs, 1975]. This simple picture describes qualitatively the amplitude scintillation phenomenon when phase deviation is small, i.e., $|\varepsilon_1|<<1$. In this case, wave front remains to be somewhat coherent even after crossing the irregularities which act to focus or defocus the rays.

However, when the irregularities are strong, i.e., when $\varepsilon_1(\mathbf{r},t)$ is relatively large, the phase deviation across the irregularities may become so large that the phase front is no longer coherent. These irregularities cannot focus or defocus the rays. Consequently, the scenario of the amplitude scintillation mentioned above is no longer valid and the saturation of scintillation amplitude is expected. At this stage, multiple scattering of radiowave may take place in the slab [Vats, 1981]. Another case for which weak scattering is not valid happens when the irregularity slab is thick. In this case, the amplitude fluctuations may develop even inside the slab, and when the wave emerges from the slab it suffers both phase and amplitude

fluctuations.

The starting equation to analyze these phenomena is the wave equation of electrodynamics. On the assumptions that

(1) temporal variations of the irregularities are much slower than the wave period, and

(2) characteristic size of the irregularities is much greater than the wavelength,

the following scalar wave equation is valid for describing the electric field inside the irregularity slab [Yeh and Liu, 1982].

$$\nabla^2 E + k^2 \{1 + \varepsilon_1(\mathbf{r})\} E = 0 \qquad 0 < z < L \qquad (1.4)$$

where E is a component of the electric field vector and $k^2 = k_o^2 < \varepsilon >$ (k_o is the wavenumber in free space). Equation (1.4) is a partial differential equation with random coefficient, the solution of which will form the basis of the scintillation theory. Unfortunately, it is impossible to get the general solution of (1.4). One has to seek various approximate solutions for different applications. To discuss these solutions, we first treat the case of normal incidence. It is convenient to introduce the complex amplitude of the wave field, $u(\mathbf{r})$

$$E = u(\mathbf{r}) \exp(-jkz) \qquad (1.5)$$

On the assumption (2), Equation (1.4) then yields an equation for the complex amplitude

$$-2jk\frac{\partial u}{\partial z}+\nabla_{\perp}^{2}u=-k^{2}\varepsilon_{1}(\mathbf{r})\,u \qquad 0<z<L \tag{1.6}$$

where $\nabla_{\perp}^{2}=\frac{\partial^{2}}{\partial x^{2}}+\frac{\partial^{2}}{\partial y^{2}}$ is the transverse Laplacian operator. Below the irregularity slab, the complex amplitude satisfies

$$-2jk\frac{\partial u}{\partial z}+\nabla_{\perp}^{2}u=0 \qquad z>L \tag{1.7}$$

The initial condition for (1.7) is given by the solution of (1.6) evaluated at z=L. Therefore, (1.6) and (1.7) are the basic equations by which the ionospheric scintillation theories are described.

In the following of the present section, two well-established scintillation theories are introduced. First, the thin phase-screen theory is outlined [Salpeter, 1967; Cronyn, 1970]. Scintillation power spectra based on this theory is described. Next, the weak scintillation theory using the Rytov approximation is outlined and the frequency dependence of the scintillation strength is presented [Wernik and Liu, 1974; Crane, 1977; Yeh and Liu, 1982]. These two theories help us to interpret a pretty large part of scintillation observation results which will be described in the following chapters. However, some peculiar features observed for intense scintillations cannot be explained by these theories [Kumagai and Ogawa, 1986]. An explanation of these features will be given in Chapter 4 by using the parabolic equation method, in which the effects of multiple

scattering are taken into account [Kumagai, 1987].

1.3.2. Phase screen theory

The phase screen theory is based on the idea that the phase fluctuation is caused by a thin phase-changing screen [Salpeter, 1967; Cronyn, 1970]. The radiowave is assumed to suffer the phase fluctuation only when it passes through the screen. The phase fluctuation is converted into amplitude scintillation as the wave propagates toward the observer after emerging from the irregularity screen. The geometries of the screen and radio propagation path are shown in Figure 1.3. From this theory, a relation between the irregularity wavenumber spectrum in the screen and the scintillation spectrum at the observer is derived as follows.

Consider that $n(\mathbf{r})$ is the electron density fluctuation at a point r in the screen. An auto-correlation function of $n(\mathbf{r})$ is given as

$$B(\mathbf{r}) = < n(\mathbf{r}) \; n(\mathbf{r}+\mathbf{r}') > \tag{1.8}$$

$B(\mathbf{r})$ and $\Phi(\mathbf{k})$, the three-dimensional wavenumber spectrum of $\Delta n(\mathbf{r})$, make a Fourier transform pair

$$B(\mathbf{r}) = \int\int\int_{-\infty}^{\infty} \Phi(\mathbf{k}) \exp(j\,\mathbf{k}\,\mathbf{r})\, d^3k \tag{1.9}$$

$$\Phi(\mathbf{k}) = (2\pi)^{-3} \int\int\int_{-\infty}^{\infty} B(\mathbf{r}) \exp(-j\,\mathbf{k}\,\mathbf{r})\, d^3r \tag{1.10}$$

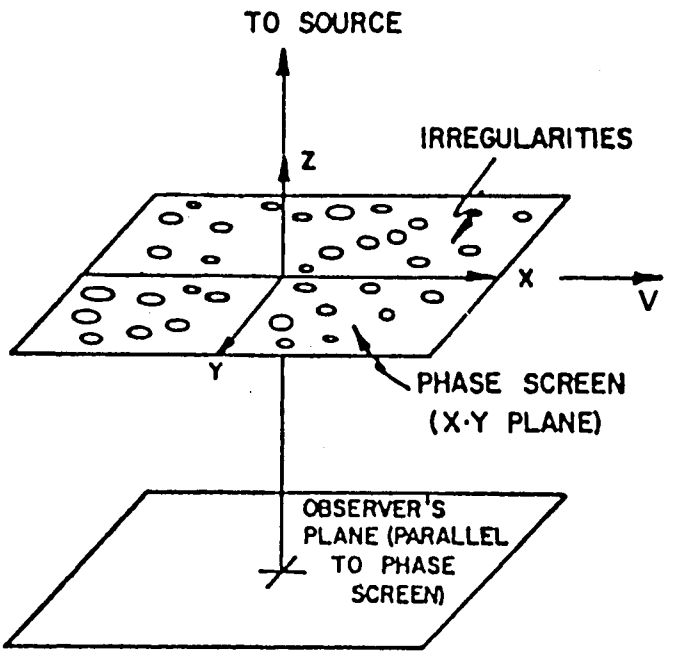

Fig. 1.3. Geometry of the phase screen. Observer's plane and phase screen are transverse to ray trajectory (after Cronyn, 1970).

In some applications, only one-dimensional wavenumber spectrum is considered. Then its wavenumber spectrum is given as

$$U(k_x, y, z) = (2\pi)^{-1} \int_{-\infty}^{\infty} B(r) \exp(-j k_x x)\, dx \qquad (1.11)$$

Two-dimensional power spectrum of the phase fluctuation of radiowave inflicted by the density fluctuation in the screen is given as [Tatarskii, 1961]

$$\Delta\phi(k_x, k_y) = 2\pi L (r_e \lambda)^2 \Phi(k_x, k_y, 0) \qquad (1.12)$$

where, $r_e = \dfrac{e^2}{4\pi\varepsilon_0 m c^2}$, λ, and L are the classical electron radius, wavelength, and the thickness of the screen, respectively. Since L is assumed to be very small, z component of $\mathbf{k}$, k_z, is regarded as 0 and then two-dimensional treatment is allowed.

Suppose that the two-dimensional screen is moving past a stationary observer with a steady velocity V in the x-direction. Then, the resultant temporal spectrum of the radiowave phase, $\Delta\phi_t(\nu)$, is obtained by integrating $\Delta\phi(k_x, k_y)$ over k_y and substituting a relation between k_x and a temporal Fourier component (frequency) ν, $k_x = 2\pi\nu/V$, as follows:

$$\Delta\phi_t(\nu) = \frac{2\pi}{V} \int_{-\infty}^{\infty} \Delta\phi(2\pi\nu/V, k_y)\, dk_y$$

$$= (2\pi r_e \lambda)^2 L/V \int_{-\infty}^{\infty} \Phi(2\pi\nu/V, k_y, 0)\, dk_y \qquad (1.13)$$

If the three-dimensional wavenumber spectrum, $\Phi(k)$, obeys an ellipsoidal power-law spectrum with index p which is given as

$$\Phi(k) \propto (1+\alpha k_x^2+\beta k_y^2+\gamma k_z^2)^{-p/2} \tag{1.14}$$

then, the one-dimensional spectrum becomes $U(k_x,y,z) \propto k_x^{p-2}$. Substituting (1.14) into (1.13), it is easy to show

$$\Delta\phi_t(\nu) \propto \{1+(2\pi\alpha\nu/V)^2\}^{-(p-1)/2} \tag{1.15}$$

Thus the index of asymptotic frequency power spectrum of the phase fluctuation becomes p-1 which is smaller by 1 than the index of the three-dimensional power spectrum of the density fluctuation.

In scintillation observations, the intensity fluctuations which arise from the phase fluctuations are usually observed. A simple relationship between the phase spectrum $\Delta\phi(k_x,k_y)$ and the intensity power spectrum $P(k_x,k_y)$ is derived under a weak-scatter condition ($\Delta\phi << 1$) as [Salpeter, 1967],

$$P(k_x, k_y) = \Delta\phi(k_x, k_y)\, F(k_x, k_y) \tag{1.16}$$

where, $F(k_x,k_y)$ is called the Fresnel filtering factor and is defined as

$$F(k_x, k_y) = 4\sin^2(k_\perp^2/k_f^2)$$

$$\simeq \begin{cases} 4\,(k_\perp^2/k_f^2) & k_\perp < k_f \\ 2 & k_\perp > k_f \end{cases} \tag{1.17}$$

Where k_f is the "Fresnel wave number", $k_f^2 = 4\pi/\lambda z$, $k_\perp^2 = k_x^2 + k_y^2$, and z is the distance to the screen. $F(k_x,k_y)$ behaves differently in two wavenumber ranges. For $k_\perp > k_f$, i.e., the irregularity scale is smaller than the Fresnel size, the phase fluctuation $\Delta\phi(k_x,k_y)$ is directly transformed into the amplitude fluctuation $P(k_x,k_y)$. On the other hand, for $k_\perp < k_f$, i.e. the irregularity scale is larger than the Fresnel size, the amplitude fluctuation does not reflect the phase fluctuation and is greatly attenuated with decrease in $k_\perp$.

The temporal spectrum of the amplitude scintillation under a weak-scatter condition is given by, similar to (1.13),

$$P_t(\nu) = \frac{2\pi}{V}\int_{-\infty}^{\infty} P(2\pi\nu/V, k_y)\, dk_y$$

$$= (2\pi r_e\lambda)^2 (L/V) \int_{-\infty}^{\infty} \Delta\phi(k_x, k_y)\, F(k_x, k_y)\, dk_y \qquad (1.18)$$

A qualitative explanation of this temporal spectrum is as follows: in the frequency range $\nu > \nu_f$ $(= Vk_f/2\pi)$, the spectrum $P_t(\nu)$ reflects the phase fluctuation spectrum $\Delta\phi_t(k_x,k_y)$, i.e., the wavenumber spectrum of the irregularities $\Phi(\mathbf{k})$. When the wavenumber spectrum of the irregularities obeys a power-law whose index is p, the index of the frequency spectrum becomes p-1. In the frequency range of $\nu < \nu_f$, however, the frequency spectrum does not reflect the wavenumber spectrum. The steep decrease in $P(k_\perp)$ in the vicinity of $k_\perp = 0$ (see (1.16)) does not appear in $P_t(\nu)$ in the vicinity of $\nu = 0$ due to the integration by k_y.

1.3.3. Weak scintillation theory - Rytov solution

When wave amplitude fluctuation due to the scattering develops even inside the irregularity slab, one has to go back to (1.6) and (1.7) to treat the scintillation phenomena. Let us write the field $u(\rho, z)$ in the form

$$u(\rho, z) \equiv A_0 \exp\{\Psi(\rho, z)\} \equiv A_0 \exp\{X(\rho, z) - j S_1(\rho, z)\} \tag{1.19}$$

where $\rho = (x, y)$ is the transverse coordinate and $X(\rho, z)$ is referred to as the log-amplitude and $S_1(\rho, z)$ as the phase deviation of the wave. The substitution of (1.19) into (1.6) makes

$$-2jk \frac{\partial \Psi}{\partial z} + \nabla_\perp^2 \Psi + (\nabla_\perp \Psi)^2 = -k^2 \varepsilon_1(r) \tag{1.20}$$

On the assumption of weak scintillation for which the higher order term $(\nabla_\perp \Psi)^2$ in (1.20) can be neglected, we obtain the following equation giving the Rytov solution [Barabanenkov et al., 1971]

$$-2jk \frac{\partial \Psi}{\partial z} + \nabla_\perp^2 \Psi = -k^2 \varepsilon_1(r) \tag{1.21}$$

The Rytov solution may be applied even to moderately strong ionospheric scintillations [Crane, 1976]. The general solution of (1.21) can be obtained as [Yeh and Liu, 1982]

$$\Psi(\rho, z) = \frac{jk}{2\pi z} \int\int_{-\infty}^{\infty} \Psi_0(\rho) \exp\{-jk|\rho-\rho'|^2/2z\}\, d^2\rho'$$

$$+ \frac{k^2}{4\pi} \int_0^z \frac{d\zeta}{z-\zeta} \int\int_{-\infty}^{\infty} \varepsilon_1(\rho', \zeta)$$

$$\cdot \exp\{-jk|\rho-\rho'|^2/2(z-\zeta)\}\, d^2\rho' \qquad (1.22)$$

where $\Psi_0(\rho)$ $(=\ln u(\rho, 0))$ represents the incident wave. The field emerging from the bottomside of the slab is given by exp $[\Psi(\rho, L)]$. The field pattern on the ground can be obtained by solving (1.7) with an initial condition, $u(\rho, L) = \exp[\Psi(\rho, L)]$. The Rytov solution for (1.7) is

$$\Psi(\rho, z) = \frac{jk}{2\pi(z-L)} \int\int \Psi(\rho', L)$$

$$\cdot \exp\{-jk|\rho-\rho'|^2/2(z-L)\}\, d^2\rho' \qquad (1.23)$$

where $\Psi(\rho', L)$ is obtained from (1.22). Equation (1.23) gives the formal solution for the ionospheric scintillation problem under the Rytov approximation. It can be used to derive various statistical parameters for the wave field. For instance, the mean-square fluctuation of $X(\rho, z)$ on the ground are given by [Wernik and Liu, 1974]

$$\langle X^2 \rangle \simeq 2\pi^2 r_e^2 \lambda^2 L \int_{-\infty}^{\infty} \left[1 - \frac{2k}{k_\perp^2 L} \sin\left(\frac{k_\perp^2 L}{2k}\right)\right.$$

$$\left. \cdot \cos\frac{k_\perp^2}{k}(z - L/2)\right] \Phi(k_\perp, 0)\, d^2k_\perp \qquad (1.24)$$

Using (1.24), the index of scintillation intensity and its frequency dependence are derived. The scintillation index, S_4, is defined as the normalized variance of signal intensity [Bischoff and Chytil, 1969]

$$S_4^2 = \frac{\langle I^2 \rangle - \langle I \rangle^2}{\langle I \rangle^2} \tag{1.25}$$

where I is the signal intensity. S_4 is one of the most important parameters to describe the scintillation intensity. When fluctuations of the field are small, an approximate expression of S_4^2 becomes [Rino and Fremouw, 1973]

$$S_4^2 \simeq 4 \langle X^2 \rangle \tag{1.26}$$

Next, the frequency dependence of the scintillation index is derived as follows [Yeh and Liu, 1982]. $\langle X^2 \rangle$ in (1.24) is roughly determined by the product of the two terms on the right hand side of (1.24), the filter function in the square brackets and the density fluctuation spectrum. Although the filter function oscillates with $k_\perp$, its first peak is most effective to determine $\langle X^2 \rangle$ because the density fluctuation spectrum is, in general, of a power-law type, which decays as $k_\perp$ increases. This means that the irregularities with sizes around the first Fresnel zone is most effective for the scintillation; the first peak of the filter function corresponds to this size. Therefore, it may be concluded that the filter function has no frequency dependence

as far as the scintillation caused by the irregularities having scale sizes around the first Fresnel zone is taken into account. Consequently, for the irregularity power spectrum of $\Phi(k_\perp, 0) \sim k_\perp^{-p}$, it is possible to show from (1.24) that

$$S_4 \propto \lambda^{(2+p)/4} \propto f^{-(2+p)/4} \tag{1.27}$$

Namely, if p=4, which is the most possible value obtained by in-situ observations [Dyson et al., 1974], the frequency dependence obeys $f^{-1.5}$. Such dependences have been observed in many experiments for which the scintillation indices are not very high [Crane, 1977; Fujita et al., 1982].

1.4. RECENT OBSERVATIONAL RESULTS OF MID-LATITUDE SCINTILLATION

In mid-latitudes, the ionospheric scintillation activity has been known to be less intense than those in equatorial and high-latitude regions. Therefore, attention has not been paid so much to mid-latitude scintillations. Thus, the morphology and mechanism of them remain unsolved. Since the Japanese experimental test satellite ETS-2 (KIKU-2) was launched in 1977, intensive studies of ionospheric scintillations started in the mid-latitude and equatorial anomaly regions, mainly in Asia. Among them, a group in the Radio Research Laboratory, Japan, has made a great contribution to the study of the mid-latitude

scintillations and ionospheric irregularities. In this section, some results of these studies are reviewed.

1.4.1. Observations of VHF scintillation and Faraday rotation

Soon after the start of the scintillation and Faraday rotation observations of 136 MHz beacon radiowave emitted from ETS-2, a close association between the scintillations and the fluctuations of Faraday rotation was found as shown in Figure 1.4 [Sinno and Kan, 1978]. These phenomena were also associated with spread-F. Similar fluctuations were also observed at Arecibo [Basu et al., 1981]. Statistical features of the VHF scintillations observed in Japan were summarized by Sinno and Kan [1980] as follows: (1) Ionospheric scintillations with long duration occurred most frequently in the summer nighttime and those with short duration occurred in the summer daytime. (2) Scintillations in nighttime are closely associated with the occurrences of Faraday rotation fluctuation and also with spread-F, and those in daytime are associated with the occurrences of sporadic-E in the ionograms. These results are shown in Figure 1.5, in which the daily variations of three quantities are depicted in the highest and lowest active months, i.e., June and December, respectively. Almost similar daily and seasonal variations in scintillation occurrence were observed on the 1.5 GHz earth-satellite path between the MARISAT satellite over the

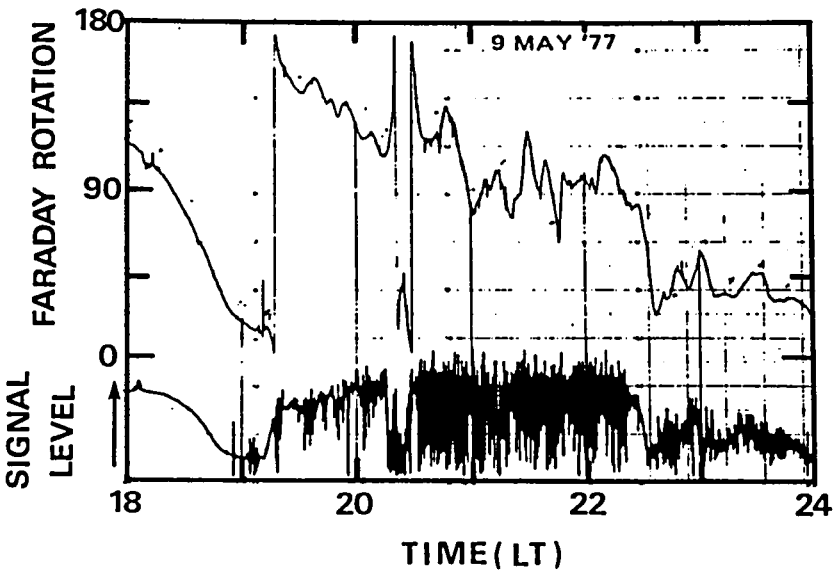

Fig. 1.4. Record of Faraday angle fluctuation associating with amplitude scintillation on May 9, 1977 (after Sinno and Kan, 1978).

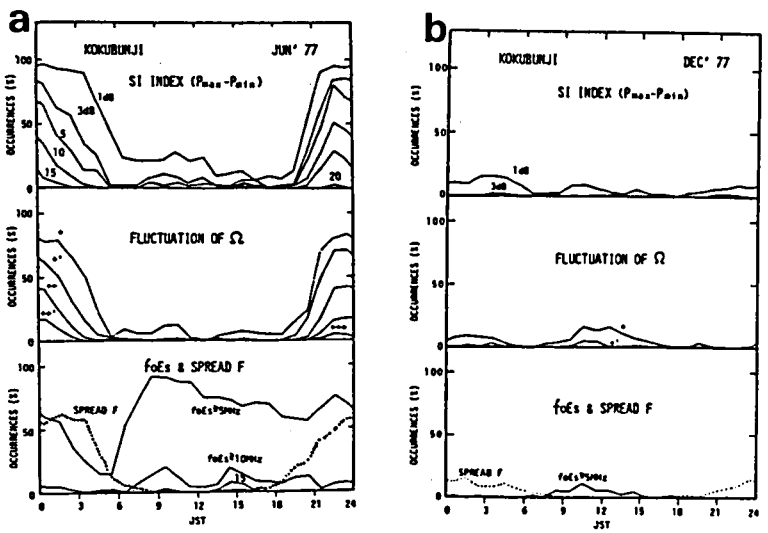

Fig. 1.5. Monthly mean diurnal variances of percentage occurrences of scintillation (top), fluctuation of Faraday rotation (middle) and ionospheric f_oE_s and spread F (bottom). (a) June, 1977, (b) December, 1977 (after Sinno and Kan, 1980).

Indian Ocean and Yamaguchi, Japan [Karasawa et al., 1985]. (3) Typical dimensions of the ionospheric irregularities obtained by the Faraday rotation measurement are estimated to be about 10 km in the horizontal plane and 2 km in the vertical plane in the sporadic-E layer, and about 200 km along the field lines and 30 km perpendicular to them in the F-region. (4) Fluctuations of the electron density accompanying with severe nighttime scintillations are expected to be as large as a few tens of percent of the background density.

Peculiar situation for the ETS-2 experiment around Japan is that the radio path from ETS-2 is almost parallel to the geomagnetic field lines. For such situation, it is pointed out that the scintillation intensity is more enhanced as compared with cases of off-parallel, because irregularities are generally extended along the field lines [Briggs and Parkin, 1963; Crain et al., 1979]. Sinno and Minakoshi [1983] have certified this effect by using multi-station receptions of the ETS-2 beacon. The enhancement factor observed is consistent with that expected from the weak scatter theory for daytime scintillations, while for the nighttime scintillations more marked enhancement due to the strong refractive scattering was obtained.

1.4.2. Mid-latitude scintillations related to geomagnetic activity

Effects of geomagnetic activity on mid-latitude

scintillations have been investigated using ETS-2 [Kumagai, 1986]. Statistics of nearly one-year data (from April 1982 to February 1983) reveal that (1) geomagnetic activity dependence of the scintillation around Japan has properties similar to those of the equatorial scintillation; i.e., the occurrence tends to be suppressed with the increase in geomagnetic activity in summer (the season of high scintillation activity), especially in the premidnight hours, and (2) there is a negative correlation between K_p index and the scintillation occurrence in the range of $0 \leq K_p \leq 4$, while the correlation becomes positive in the range of $K_p \geq 5$, so that we may have two peaks of the occurrence at K_p =1 or 2, and $K_p \geq 8$. These situations appear in Figure 1.6. The former peak depends obviously on the season, whereas the latter does slightly. These results will give an indication that the scintillation tends to occur more frequently during severe geomagnetic storms in any season.

Oyama et al. [1984] studied the scintillations by using the radio signals from an equator-orbiting satellite, and reported the statistical results showing that the occurrence rate and the spatial extent of the scintillation increased rapidly when K_p was larger than 6. Although these results were concerned with the scintillation observed in the region between 0 and 20 N geomagnetic latitudes, they seem consistent with the results described above.

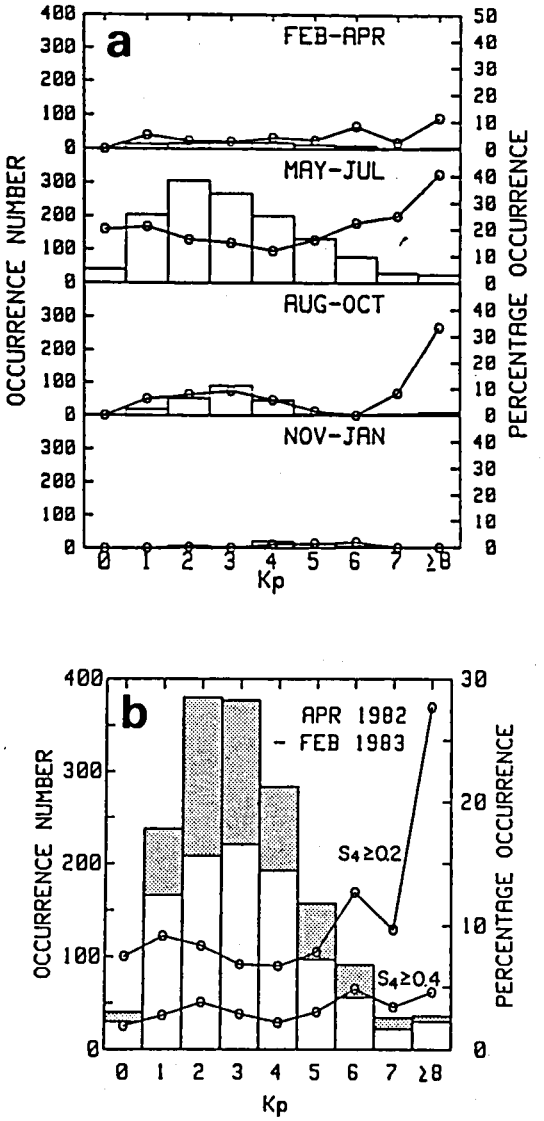

Fig. 1.6. The occurrence number (histogram) and rate (open circle and solid line) of the scintillation against K_p index. (a) Plots are made for each season only in the case of $S_4 \geq 0.2$. (b) The totaled occurrence number and the averaged rate throughout the year are plotted. The results are shown in the two cases of $S_4 \geq 0.2$ and $S_4 \geq 0.4$. Empty (shaded) portion of the histogram indicates $S_4 \geq 0.2$ ($S_4 \geq 0.4$), respectively (after Kumagai, 1986).

1.4.3. Severe scintillations during geomagnetic storms

Severe nighttime scintillations of VHF and GHz waves (136 MHz, 1.7, 4, and 11.5 GHz) emitted from the three Japanese geostationary satellites were observed during a geomagnetic storm on February 15, 1978 [Ogawa et al., 1980]. The scintillation records at these four frequencies were shown in Figure 1.7, together with the relative total electron content (TEC) obtained from Faraday rotation measurement of the 136 MHz radiowave from ETS-2. The maximum scintillation amplitude was 20 dB p-p (peak to peak) at 136 MHz, 14 dB p-p at 1.7 GHz, 7 dB p-p at 4 GHz, and 0.8 dB p-p at 11.5 GHz. The GHz wave scintillations were strongly enhanced when irregular fluctuation of TEC was varying sharply with time, which may indicate that the small scale irregularities producing the scintillations above 1 GHz are formed near the large scale steep gradient of electron density.

Detailed analysis showed that the one-dimensional wavenumber spectrum of irregularities obeys a form of k^{-2} and that the scintillation spectra vary as ν^{-3} (ν is the fluctuation frequency). The scintillation index, S_4 seems to have frequency dependence of $f^{-0.5}$ for 136 MHz < f < 1.7 GHz, f^{-1} for 1.7 < f < 4 GHz, and f^{-2} for 4 < f < 11.5 GHz (f is radiowave frequency). This situation is shown in Figure 1.8. The smaller gradient between 136 MHz and 1.7 GHz seems to be due to the saturation of the scintillation at 136 MHz.

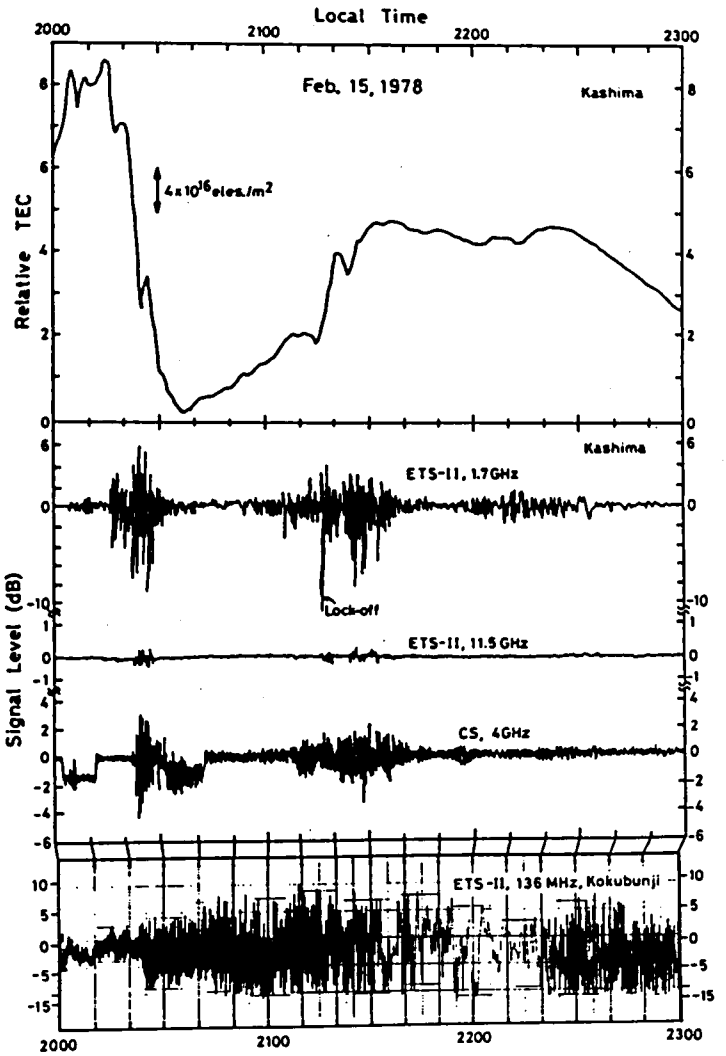

Fig. 1.7. Scintillation recordings at 136 MHz observed at Kokubunji, and of 1.7, 4, and 11.5 GHz observed at Kashima. Decreases of averaged 4 GHz signal level, which are centered at 2005 and 2035 LT are due to the satellite ranging operation. Also shown is the TEC variation measured by the differential phase shift method between 1.7 and 11.5 GHz (after Ogawa et al., 1980).

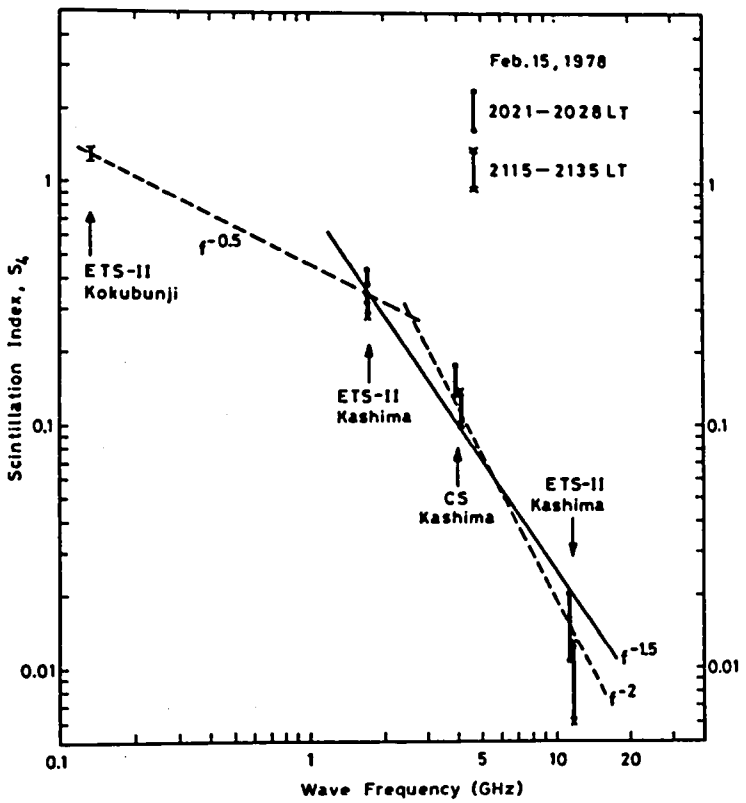

Fig. 1.8. Radiowave frequency dependence of S_4. Vertical bar represents the extent of S_4 during the indicated local time (after Ogawa et al., 1980).

The scintillations of this type have been observed several times since the event mentioned above. Minakoshi et al. [1981] found from the observations at several stations that the area of ionospheric disturbance producing 4-GHz wave scintillation was generated in the limited region of the south of Japan and then moved apparently northward. Karasawa et al., [1985] reported that very severe scintillations with peak-to-peak fluctuations exceeding 10 dB at 1.5 GHz were observed in the equinoctial months. Tanaka [1981] clarified the following conditions necessary for initiating the microwave scintillations of this type; (1) The maximum or recovery phase of the geomagnetic storm should lie within several hours after sunset, and (2) the equatorial anomaly should develop before the scintillations start.

Ogawa and Kumagai [1985] found evidence that severe nighttime GHz scintillations under geomagnetic storm conditions are closely associated with deep depletions of TEC. The TEC depletions amount to $2\text{-}8 \times 10^{16}$ el/m^2 (10-30 % of the background TEC), and their durations range from 10 min to 1 hour. These depletions move northward or eastward with velocities between 60 and 260 m/s. The depletions are not probably counterparts of the equatorial bubbles but seem to be formed in localized regions around Japan under complicated and disturbed ionospheric conditions.

CHAPTER 2

METHOD OF SPACED-RECEIVER SCINTILLATION MEASUREMENTS

2.1. INTRODUCTION

Moving random patterns occur quite commonly in geophysics. In some radio experiments on the upper atmosphere, e.g. ionospheric drifts, ionospheric scintillations, and interplanetary scintillations, moving pattern of radiowave field is measured on the ground using at least three spaced antennas. In the analysis of such moving patterns, the mean drift velocity is one of important quantities to be determined. In addition, parameters describing spatial properties of the pattern and its random changes are also required to be determined. From the scintillation measurements with spaced-receivers, it is possible to obtain the motion and spatial properties of the irregularities. From these results, the mechanism of scintillation and the development of the irregularities can be investigated.

The correlation analysis has been developed over three decades as a suitable analysis for experiments of this type. Since Briggs et al. [1950] and Phillips and Spencer [1955] established the analysis, there is a large number of papers on the subject including several comprehensive reviews [cf. Briggs,

1968, 1977]. Generalized arithmetical method was described by Kent and Koster [1966]. Recently, elaborated analyses of velocity fluctuation or velocity gradient within the scatterer have been made to clarify the physical meaning of random velocity [Wright and Pitteway, 1978; Wernik et al., 1983].

In this chapter, first, the explanation of the correlation analysis is given. The explanation is composed of two parts, which are a basic concept of the analysis and practical procedure for two-dimensional anisotropic pattern. Next, the method of the spaced-receiver scintillation measurements is given. The instruments and their arrangement are described. Finally, examples of results and consideration for the accuracy of the analysis are given.

2.2. BASIC CONCEPT OF CORRELATION ANALYSIS

2.2.1. One-dimensional randomly-changing pattern

The basic concept of the correlation analysis is first given by referring to the classical paper by Briggs et al. [1950]. Consider a one-dimensional pattern, i.e., a pattern is a function of one space variable x and time t. Figure 2.1a illustrates a random function R(x,t) which moves with a velocity V along x axis, and changes form as it moves. Consider first an observer in

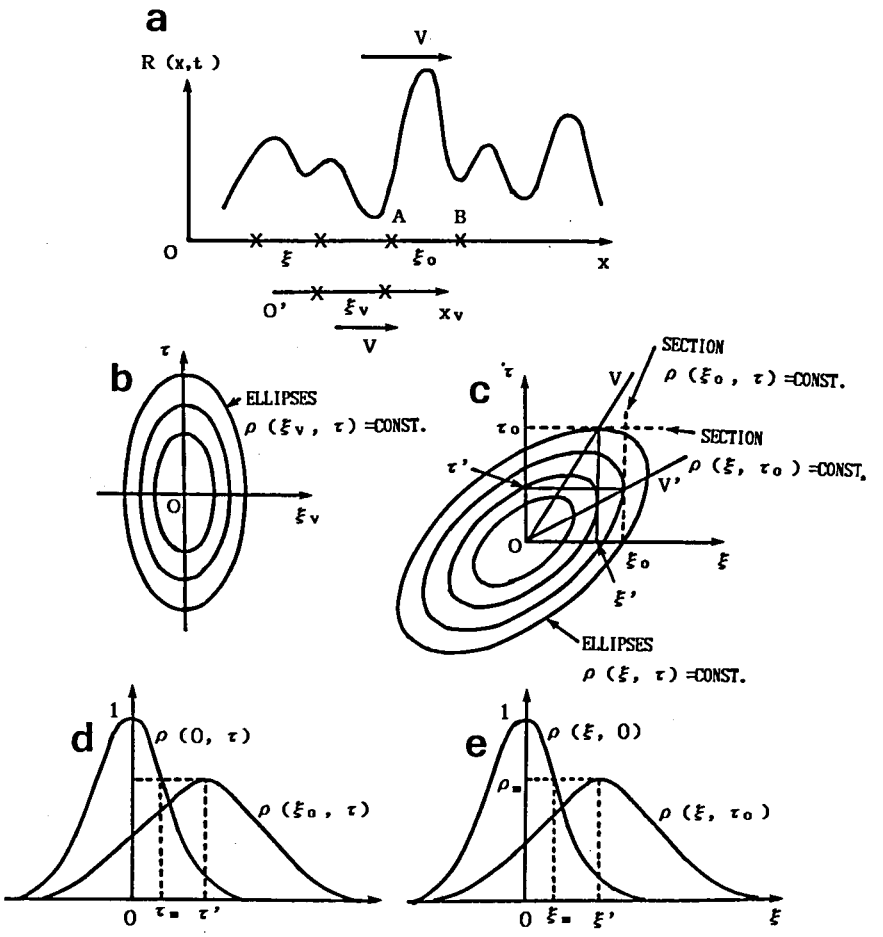

Fig. 2.1. (a) A random one-dimensional pattern, moving with velocity V along the x axis. (b) Correlation ellipses $\rho(\xi_0, \tau) = \text{const.}$ for an observer who 'follows the motion'. (c) Correlation ellipses $\rho(\xi, \tau) = \text{const.}$ for a fixed observer. (d) Auto-and cross-correlation functions for two records continuous in time at points separated by a distance ξ_0. (e) Auto- and cross-correlation functions for two records continuous in space, at two times separated by an interval τ_0.

a coordinates system $O'x_v$ which moves with velocity V in the x direction. Variables with suffix v represent those in this moving frame. The only changes recorded by this observer are those arising from the random changes of the pattern. In this coordinate system, space-time correlation function of the stationary pattern is given as

$$\rho(\xi_v, \tau) = \frac{\langle \{R(x_v, t) - \langle R \rangle\} \{R(x_v + \xi_v, t + \tau) - \langle R \rangle\} \rangle}{\langle \{R(x_v, t) - \langle R \rangle\}^2 \rangle} \quad (2.1)$$

It is assumed that the contours of $\rho(\xi_v, \tau)$=constant in the (ξ_v, τ) plane has the form of similar concentric ellipses as shown in Figure 2.1b [Briggs, 1968]. This assumption seems reasonable because $\rho(\xi_v, \tau)$ has a maximum value (unity) at the origin and equi-value contours of any function of two variables take elliptic forms within relatively small area around the maximum. Therefore, $\rho(\xi_v, \tau)$ must be a function of a quantity of $(\xi_v^2/d^2 + \tau^2/\tau_c^2)$, where d is a characteristic length and τ_c is a characteristic time scale. Contours $\rho(\xi_v, \tau)$=constant are then given by

$$\xi_v^2/d^2 + \tau^2/\tau_c^2 = \text{const.} \quad (2.2)$$

and have the form of similar concentric ellipses. The axial ratio of the ellipses is given by d/τ_c, which has the dimensions of velocity and is denoted by V_c

$$V_c = d/\tau_c \quad (2.3)$$

This is the ratio of the space shift and time shift which produce

the same value of correlation decrease. With this notation, we can write

$$\rho(\xi_v,\tau)=f(\xi_v^2+V_c^2\tau^2) \tag{2.4}$$

where f is a function which decreases from unity at the origin to zero for large values of argument, but is otherwise arbitrary.

We now return to consider an actual observer in the fixed coordinate system Ox, and derive an expression for the space-time correlation function $\rho(\xi,\tau)$ for this observer. Relations between variables in fixed and moving flames are

$$x = x_v + V\tau$$

$$\xi = \xi_v + V\tau$$

Substituting these relations into (2.4) we obtain

$$\rho(\xi,\tau) = f\{(\xi - V\tau)^2 + V_c^2\tau^2\} \tag{2.5}$$

Contours of constant correlation $\rho(\xi,\tau)$=constant now have the form shown in Figure 2.1c. They are still concentric ellipses, but the major and minor axes no longer lie along the coordinate axes.

From (2.5) it is seen that the temporal correlation function is given by

$$\rho(0,\tau) = f(V^2\tau^2 + V_c^2\tau^2) \tag{2.6}$$

The change of the correlation in time at a fixed point is due to two separate effects represented by two terms in the bracket. The drift velocity V produce a correlation decrease $f(V^2\tau^2)$, and the second term represents the effects of the change of the pattern and produces correlation decrease $f(V_c^2\tau^2)$. Therefore, the ratio

V_c/V is a useful measure representing the importance of random change as compared with the effect of drift.

2.2.2. Two types of observations

There are two types of observations which may be made [Briggs, 1968]; one is an observation made at two points separated by a fixed distance ξ_0 being continuously in time. The other is an observation of the whole pattern at two times separated by τ_0. In the observation of the former type, which is usually made in the case of radio wave observations, the cross-correlation function of the two records at separate points is immediately calculated, that is a section $\rho(\xi_0,\tau)$ of the function $\rho(\xi,\tau)$ (Figure 2.1c). In order to find τ', which gives the peak of the cross-correlation function, we make use of (2.5), and setting $\xi=\xi_0$

$$\frac{\partial \rho}{\partial \tau} = 0 \tag{2.7}$$

Then we find

$$\tau' = \frac{\xi_0 V}{(V^2 + Vc^2)} \tag{2.8}$$

Thus the ratio ξ_0/τ' does not give the true velocity V of the pattern but only an 'apparent velocity' V' given as

$$V' = \xi_0/\tau' = V + V_c^2/V \tag{2.9}$$

The apparent velocity is always greater than the true drift velocity.

In Figure 2.1c, the maximum correlation for the section $\rho(\xi_0,\tau)$ will occur when the vertical line $\xi=\xi_0$ is a tangent to an ellipse of the family. If the line is drawn from the origin to the point of contact of the tangent, the slope of this line is 1/V'. In order to complete the analysis, we need to find V and V_c. This can be done in various ways which will be discussed later.

The other type of observation is to make two 'snapshots' at times separated by an interval $\tau=\tau_0$, i.e. observations continuous in space and separate in time. By calculating the cross-correlation between these two snapshots, we obtain the cross section $\rho(\xi,\tau_0)$ of the function $\rho(\xi,\tau)$ (see Figure 2.1c). This will have a peak value for some space shift ξ'. In order to calculate ξ', we make use of (2.5), and setting $\tau=\tau_0$, then

$$\frac{\partial \rho}{\partial \xi} = 0 \tag{2.10}$$

This gives

$$\xi' = V \tau_0 \tag{2.11}$$

Thus even if the pattern changes as it moves, the drift velocity can be found directly from the space shift which gives the maximum cross-correlation. This result is illustrated in Figure 2.1c. The maximum correlation for the section $\rho(\xi,\tau_0)$ occurs where the horizontal line $\tau=\tau_0$ touches an ellipse of the

family. A line from the origin to the point of contact has a slope 1/V.

2.2.3. Definitions of basic quantities

We give definitions of a basic quantity which is newly introduced and give summaries of those which are already introduced in the preceding sections; both are used in the analysis. They are given in one-dimensional formulas, and they are soon applicable to two-dimensional case.

(1) Fading velocity V_c'

This is a measure of the ratio of space shift to time shift necessary to produce the same change in the value of ρ. When we use the spaced receivers with ξ_0 apart, $\rho(\xi_0,0)$ gives the effect of a pure space shift ξ_0. If we find a time lag τ_s which gives $\rho(0,\tau_s) = \rho(\xi_0,0)$, τ_s gives the effect of a pure time shift. Then the definition of V_c' gives

$$V_c' = \xi_0 / \tau_s \tag{2.12}$$

(2) Drift velocity V

This is the velocity of an observer who has so adjusted his motion on the ground that he experiences the speed of fading minimum. Suppose he compares signal amplitudes at times τ_0 apart. His displacement ξ' during this time period should be so adjusted that $\rho(\xi',\tau_0)$ is a maximum, and then

$$V = \xi' / \tau_0 \tag{2.13}$$

This velocity is an unambiguous measure of the movement of the pattern along the ground. For two-dimensional ground V has direction. Assuming axes of x and y on the ground, let the direction be at angle ϕ to the x axis. Then the components of the velocity along the axes are

$$V_x = V \cos \phi$$

$$V_y = V \sin \phi$$

(3) Apparent drift velocity V'

When the fading records are observed at two separate points on the ground (distance is ξ_0), suppose that the cross-correlation function has the peak value at time lag τ'. The apparent velocity of drift is then

$$V' = \xi_0 / \tau' \qquad (2.14)$$

For two-dimensional ground, suppose that we have three receivers at origin (0,0), $(\xi_0,0)$, and $(0,\eta_0)$. Let τ_x' and τ_y' are time lags for best correlation between the first and second, and the first and third receivers, respectively. Then the apparent velocities in the two directions are

$$V_x' = \xi_0 / \tau_x' \quad \text{and} \quad V_y' = \eta_0 / \tau_y'$$

It is noted that these values are not components of a vector V' but both larger than V'.

(4) Characteristic velocity V_c

This is the value of V_c' which is seen by the observer who is moving at velocity V. V_c gives a quantitative measure of random change taking place on the patterns. To this moving

observer the ratio of space shift and time shift necessary to produce a similar change in ρ is

$$V_c = \xi_0 / \tau_c \qquad (2.15)$$

where $\rho(\xi_0,0) = \rho(V\tau_c,\tau_c)$.

2.2.4. Derivation of V and V_c

From the spaced receiver (ξ_0 apart) measurement of the fading records, correlation function $\rho(\xi,\tau)$ is obtained continuously in time, while only at 0 and ξ_0 in space. We can easily derive V' and V_c' from the obtained $\rho(\xi,\tau)$. It is shown in this section how V and V_c are derived from the observed values.

It is imagined that contours of moving pattern (velocity is V) has shapes something like in Figure 2.2a in one-dimensional x and t space. In the frame with velocity V in x direction (X_v,t), we obtain Figure 2.2b, which corresponds to the case that the observer moving with V sees the pattern. It is considered that for such an observer the ratio of the space and time shifts which have the same effects in changing ρ is V_c. Therefore, we make Figure 2.2c, in which the coordinate $V_c t$ is used in place of t, so that the average gradient of the contours is the same along both axes in the diagram, i.e. contours become circle. Change of ρ between any two representative points depend only on their distance regardless of their direction in this diagram.

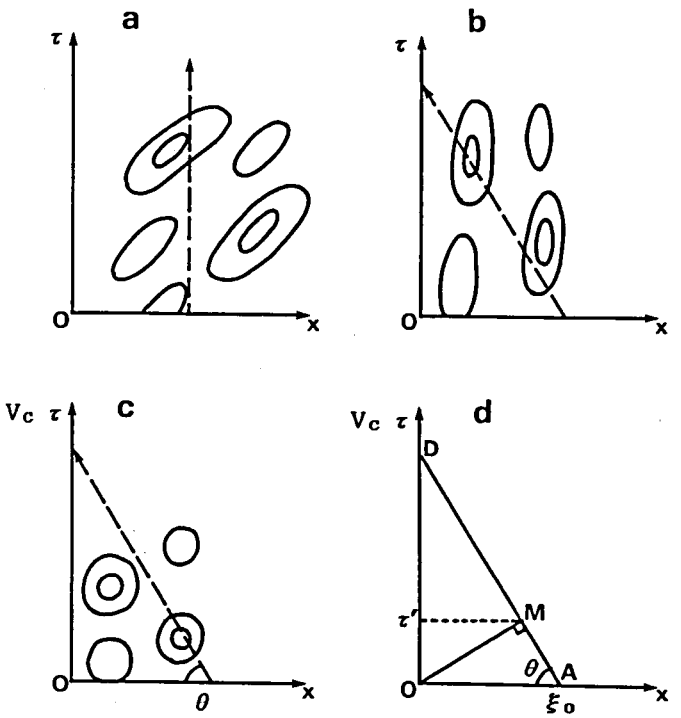

Fig. 2.2. (a) Moving irregularity contours in x-τ space. (b) In the case that the origin of the x coordinate is moved along with velocity V. (c) The coordinate $V_c\tau$ is used in place of τ. The average gradient of the contours is the same along both axes. (d) The (x, $V_c\tau$) diagram, same as (c) but the contours are omitted.

A fixed point on the ground will have velocity -V relative to the axes of Figure 2.2c. This point draws a line tilted to the negative x direction on the diagram as time t increases; the tilted angle of this line is θ, where

$$\cot\theta = x_v / V_c t = V/V_c \tag{2.16}$$

Thus the values of ρ along this line are those experienced at the fixed point on the ground. The (x_v, $V_c t$) diagram is redrawn in Figure 2.2d, in which the contours are omitted. The distance on this diagram corresponds to the total number of fadings. Since a fixed observer feels the speed of fading V_c', he experiences the total fading $V_c' t$ during a certain time period t, then

$$V_c' t = V_c t / \sin\theta \tag{2.17}$$

Combining (2.16) to eliminate

$$V_c'^2 = V_c^2 + V^2 \tag{2.18}$$

We obtain the fading record of the second receiver at distance ξ_0 from the first one. The point of the second receiver moves on line AD in Figure 2.2d with time elapses. It is seen that the highest correlation is obtained between the first receiver at O and the second one when the second receiver is at M($t=\tau'$); M is the nearest point to O on AD. The height of M above the x axis is $V_c\tau'$ and the following relation is derived

$$V_c\tau' = \xi_0 \sin\theta\cos\theta = \xi_0 V_c V/(V_c^2 + V^2) \tag{2.19}$$

in which we make use of (2.17) to eliminate θ. From definition of V',

$$V' = \xi_0 / \tau' = (V_c^2 + V^2)/V \tag{2.20}$$

Then

$$VV' = V_c^2 + V^2 = V_c'^2 \tag{2.21}$$

Note that the determination of τ' gives V' immediately. V_c' is also obtained from the observation (see (2.12)). Consequently, V and V_c are derived using the values of V' and V_c'.

Other method shows more simple relation to give V; using a time lag τ_e at which the auto- and cross-correlation curves cross each other

$$\rho(0, \tau_e) = \rho(\xi_0, \tau_e) \tag{2.22}$$

then

$$V = \xi_0 / 2\tau_e \tag{2.23}$$

Above discussions can be easily extended to the case of two-dimensional ground if the moving pattern is spatially isotropic. Consideration similar to those employed above leads to the results as follows; we consider the simplest case that the three observation points form a triangle AOB with the right angle AOB. OA and OB are along the axes Ox and Oy, respectively.

$$V_x V_x' = V_y V_y' \tag{2.24}$$

$$\tan\phi = V_y / V_x = V_x' / V_y' \tag{2.25}$$

where ϕ is an angle between V and Ox.

2.3. CORRELATION ANALYSIS OF TWO-DIMENSIONAL ANISOTROPIC PATTERN

2.3.1. Anisotropic pattern

In the case of the two-dimensional ground, it is an important objective for the correlation analysis to derive the size or shape of the fluctuating pattern as well as the drift velocity. The fluctuating patterns have anisotropic shapes in many cases, e.g., the ionospheric irregularities are considered to have shapes being extended along the direction of geomagnetic field line. For the anisotropic pattern, the deduction method of the pattern shape and drift velocity was first derived by Phillips and Spencer [1955] in somewhat geometrical manner. They also discussed the error which might occur if the anisotropic pattern was wrongly assumed to be isotropic.

Kent and Koster [1966] showed more generalized and arithmetical method which is applicable to the case of an arbitrary alignment of three receiving points. In the succeeding sections the method of the analysis is described in accordance with their procedure. In the analysis, three auto-correlograms of the receiving records obtained at three fixed receiving points and three cross-correlograms of the three pairs of these receivers are used.

First, we show the method to deduce the correlation ellipsoid which is an extension of the correlation ellipse introduced in 2.2.1 to the three dimensional space (x, y, τ). This ellipsoid can be considered to represent the averaged shape of the fluctuating pattern, i.e., the pattern of the ionospheric irregularities. Figure 2.3 shows the schematic picture of the

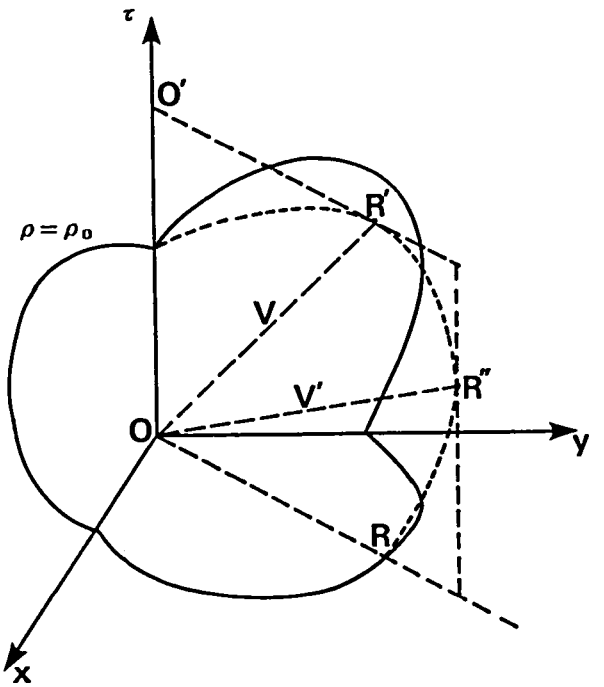

Fig. 2.3. Cross sections of correlation ellipsoid with correlation coefficient $\rho = \rho_0$ in (x, y, τ) space.

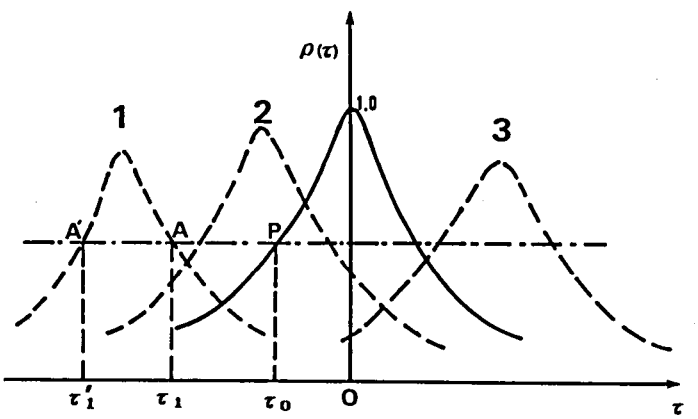

Fig. 2.4. Typical correlograms obtained by the three spaced observation.

ellipsoid. Typical correlograms which may be obtained from the three-spaced observation are shown in Figure 2.4. Crossing points between all correlation functions and a horizontal line, which represents some correlation level, exist on the same ellipsoid.

2.3.2. (ℓ, τ) ellipse on a section of ellipsoid

Consider a pair of receiving points on the ground at a separation ℓ_1. As has been discussed in 2.2.1, correlation ellipse can be drawn in the one-dimensional ground and time coordinate system. This ellipse is shown in Figure 2.5 and is equivalent to a section of the ellipsoid in Figure 2.3. This section is on the vertical plane, of which the foot line on x-y plane represents the direction of the pair of receiving points (antenna base line). Consider the ellipse at some correlation level (ρ_0). Points P, A, and A' in Figure 2.5 correspond to the points in Figure 2.4; they are crossing points between a horizontal line $\rho=\rho_0$, and the mean auto-correlogram and cross-correlogram (No.1). Time shifts of these points τ_0, τ_1, and τ_1' are also shown in both Figures 2.4 and 2.5.

These three values are sufficient to define the equation of the ellipse in the (ℓ,τ) plane, which may be written as

$$a_1\ell^2 + 2h_1\ell\tau + b_1\tau^2 = 1 \qquad (2.26)$$

Where, the coefficients are

$$a_1 = \frac{1}{\ell_1^2}\ (1 + \tau_1\tau_1'/\tau_0^2)$$

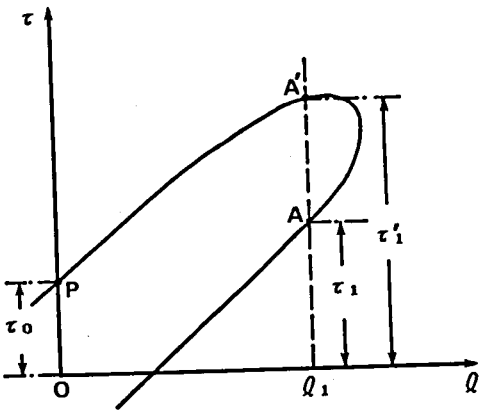

Fig. 2.5. Correlation ellipse in (ℓ , τ) plane.

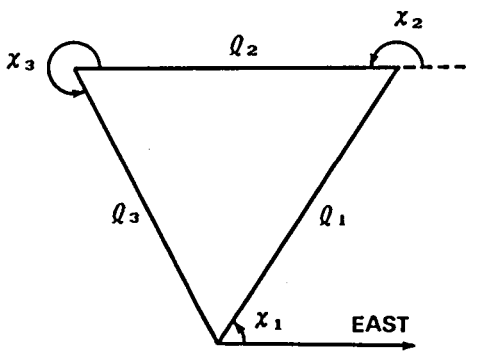

Fig. 2.6. Arrangement of three receiving stations.

$$h_1 = -(\tau_1 + \tau_1') / 2\ell_1\tau_0^2$$

$$b_1 = 1 / \tau_0^2$$

This operation is repeated for every pairs of receivers, i.e. for three (ℓ, τ) planes. A set of values (a_i, h_i, b_0), for i= 1 - 3, are obtained, where we have $b_1 = b_2 = b_3 = b_0$ since τ_0 is common to all planes. This set of values is sufficient to construct the correlation ellipsoid in three-dimensional space.

In the above procedure, the mean auto-correlogram is used under the assumption that the auto-correlograms at three points are very similar to one another. In practice there sometimes appear auto-correlograms relatively different from one another. Since these data may derive poorly reliable results, they should be omitted in the data processing. In addition, in order to improve the reliability, it is necessary to fit the correlograms to some smooth functions of curves in vicinity of the crossing points and to determine the precise crossing points.

2.3.3. Calculation of coefficients of ellipsoid

The equation of the correlation ellipsoid in (x, y, τ) coordinate system is written as

$$ax^2 + 2hxy + by^2 + 2fx\tau + 2gy\tau + c\tau^2 = 1 \qquad (2.27)$$

The coefficients are calculated from the values of (a_i, h_i, b_0) obtained above. Suppose that the receiving points are aligned as in Figure 2.6 where the east is taken as a reference direction.

χ_i is an angle of each side of the triangle measured from east.

Let $\mathbf{r}$ = [a, 2h, b] a column vector,

$\mathbf{a}$ = [a_1, a_2, a_3] a column vector,

and

$$\mathbf{A} = \begin{pmatrix} \cos^2\chi_1, & \sin\chi_1\cos\chi_1, & \sin^2\chi_1 \\ \cos^2\chi_2, & \sin\chi_2\cos\chi_2, & \sin^2\chi_2 \\ \cos^2\chi_3, & \sin\chi_3\cos\chi_3, & \sin^2\chi_3 \end{pmatrix} \tag{2.28}$$

Then $\mathbf{r}$ can be given as (Appendix A)

$$\mathbf{r} = \mathbf{A}^{-1}\,\mathbf{a} \tag{2.29}$$

where $\mathbf{A}^{-1}$ is the inverse matrix of $\mathbf{A}$. It can be calculated from both the alignment of the receiving stations and $\mathbf{a}$. The actual numerical computation is not as formidable as might appear since $\mathbf{A}^{-1}$ is fixed and needs to be calculated once for a particular configuration.

The remaining constants will be found from the following equations (Appendix A)

$$f = \frac{h_2\sin\chi_1 - h_1\sin\chi_2}{\sin(\chi_1-\chi_2)} = \frac{h_3\sin\chi_2 - h_2\sin\chi_3}{\sin(\chi_2-\chi_3)} = \frac{h_1\sin\chi_3 - h_3\sin\chi_2}{\sin(\chi_3-\chi_1)}$$

$$g = \frac{h_1\cos\chi_2 - h_2\cos\chi_1}{\sin(\chi_1-\chi_2)} = \frac{h_2\cos\chi_3 - h_3\cos\chi_2}{\sin(\chi_2-\chi_3)} \tag{2.30}$$

$$= \frac{h_3 \cos\chi_1 - h_1 \cos\chi_3}{\sin(\chi_3 - \chi_1)}$$

$$C = b_1 = b_2 = b_3 = b_0$$

Triplet values of f and g are obtained. They are averaged in use. In fact, they should ideally be equal one another and their coincidence may be a good indicator for the accuracy of the results.

2.3.4. Axial ratio and direction of ground pattern

An equation of the ground pattern ellipse is obtained from (2.27) by setting $\tau = 0$

$$ax^2 + 2hxy + by^2 = 1 \qquad (2.31)$$

The axes of this ellipse are given by

$$1/b_0^2 = \{(a + b) + \sqrt{(a-b)^2 + 4h^2}\}$$
$$1/a_0^2 = \{(a + b) - \sqrt{(a-b)^2 + 4h^2}\} \qquad (2.32)$$

Here, the axial ratio γ and the direction of the major axis ψ are given as follows

$$\gamma = a_0 / b_0 \qquad (2.33)$$

$$\tan 2\psi = 2h / (a - b) \qquad (2.34)$$

The three parameters γ, ψ, and the size of minor radius b_0 are values necessary to describe the ellipse unambiguously.

2.3.5. Derivation of V and V_c

The drift velocity V is found by drawing a horizontal plane tangent to the ellipsoid, in the similar manner as stated in 2.2.2. This is shown in Figure 2.3 in which the contact point is R'. Hence, V is given by a vector OR'. In order to obtain the contact point, we differentiate (2.27) with respect to x and y, respectively

$$\begin{aligned}(ax + hy + f\tau) + \frac{d\tau}{dx}(fx + gy + c\tau) &= 0\\ (hx + by + g\tau) + \frac{d\tau}{dy}(fx + gy + c\tau) &= 0\end{aligned} \tag{2.35}$$

Therefore, the following relations must be filled

$$\begin{aligned}ax + hy + f\tau &= 0\\ hx + by + g\tau &= 0\end{aligned} \tag{2.36}$$

Solving these, we have

$$V = \frac{\sqrt{x^2+y^2}}{\tau} = \left\{\left(\frac{bf-hg}{ab-h^2}\right)^2 + \left(\frac{ag-hf}{ab-h^2}\right)^2\right\}^{1/2} \tag{2.37}$$

and the direction of the drift velocity, ϕ, is given by

$$\tan\phi = \frac{y}{x} = \frac{ag-hf}{bf-hg} \tag{2.38}$$

When the axial ratio of the ground pattern becomes very large, these equations do not lead to accurate results. This is because both the numerator and the denominator of (2.37), as well as (2.38), tend to zero and the values of V and ϕ becomes largely uncertain. In fact, the component along the major axis becomes uncertain while the component along the minor axis is unaffected. Hence, it seems possible to derive the latter

component. In this case, the following approximate formulas are useful; the ellipse with large axial ratio can be approximated to a parabola, for which

$$ab = h^2 \tag{2.39}$$

$$\tan \phi = - (a/h) = - (h/b) \tag{2.40}$$

The direction of minor axis ϕ' is given by

$$\tan \phi' = (h/a) = (b/h) \tag{2.41}$$

In the case of ellipse, the lines with slopes (h/a) and (b/h) do not well coincide with the minor axis but lie on either side of it. The components of V along these directions will not quite be equal to the components along the minor axis but will be very close to,

$$\text{Along } (h/a) : V_a = \frac{1}{\sqrt{a^2+h^2}} \left(\frac{a h g - h^2 f + a b f - a h g}{a b - h^2} \right)$$

$$= \frac{f}{\sqrt{a^2+h^2}} \tag{2.42}$$

$$\text{Along } (b/h) : V_b = \frac{g}{\sqrt{h^2+b^2}} \tag{2.43}$$

2.3.6. Derivation of V/Vc

In Figure 2.3 the ratio (V/Vc) is equal to (O'R'/OR). At R' or R

$$y/x = (hf - ag) / (gh - bf) \tag{2.44}$$

Equation (2.27) may be rewritten as

$$x(ax + hy + f\tau) + y(by + hx + g\tau) + \tau(fx + gy + c\tau) = 1 \tag{2.45}$$

Hence at R'

$$fx + gy + ct = 1/\tau \tag{2.46}$$

Also from the previous equations (2.36) we see that

$$\begin{aligned} x(ag - fh) &= y(bf - gh) \\ x(ab - h^2) &= \tau(gh - bf) \\ y(ab - h^2) &= \tau(hf - ag) \end{aligned} \tag{2.47}$$

Substitution of (2.47) into (2.46) gives

$$x^2 + y^2 = \left(\frac{1}{ab - h^2}\right) \cdot \left\{\frac{(gh - bf)^2 + (hf - ag)^2}{2fgh - bf^2 - ag^2 + c(ab - h^2)}\right\} \tag{2.48}$$

On the other hand at R

$$ax^2 + 2hxy + by^2 = 1 \tag{2.49}$$

Substitution of (2.44) gives

$$x^2 + y^2 = \frac{(gh - bf)^2 + (hf - ag)^2}{(ab - h^2)(ag^2 - 2fgh + bf^2)} \tag{2.50}$$

Comparison of (2.48) and (2.50) gives

$$(V/V_c)^2 = \frac{ag^2 - 2fgh + bf^2}{c(ab - h^2) - (ag^2 - 2fgh + bf^2)} \tag{2.51}$$

It is found that, as in the case of V, (V/V_c) also becomes

inaccurate for large axial ratio. It is however possible to adopt a similar procedure as for V and find approximate formulas for (V/V_c) which give a high degree of accuracy under these conditions. The simple procedure is to calculate (V/V_c) along the directions given by $\tan^{-1}(h/a)$ and $\tan^{-1}(b/h)$. The results are

$$\text{Along } \tan^{-1}(h/a): \quad (V_c/V)^2 = \left\{ \frac{a^3 + 2ah^2 + bh^2}{(hg + af)^2} \right\} c - 1 \tag{2.52}$$

$$\text{Along } \tan^{-1}(b/h): \quad (V_c/V)^2 = \left\{ \frac{b^3 + 2bh^2 + ah^2}{(bg + fh)^2} \right\} c - 1 \tag{2.53}$$

2.4. OBSERVATION INSTRUMENTS AND ARRANGEMENT

2.4.1. Instruments

All necessary for satellite radiowave reception at three-spaced positions are three sets of antenna and receiver, and additional instruments such as an analog data recorder and mini-computer for data storage and processing. The radiowave used is a carrier wave of VHF telemeter signal (136.112 MHz) transmitted from the geostationary satellite ETS-2 (Engineering Test

Satellite Type 2; Kiku-2) stationed at 130°E above the equator.

Two of three antennas are crossed-Yagi type with 12 elements; they were designed to detect the polarization angle of radiowave field as well as its strength. Figure 2.7 shows a photograph of the antenna. The antenna gain and beam width are 12 dB and 35°(HPBW), respectively. Another antenna used is a helical type of which the gain is a little lower than the former. Three narrow band receivers (bandwidth of 1 kHz) are used. Their characteristics are almost similar to one another. The wavefield strengths are obtained by three receivers and the polarization angle is obtained by one of the three receivers.

Figure 2.8 shows the block diagram of the receiving system by which the polarization angle as well as field strength is obtained. The dynamic range and time constant for the wavefield intensity measurement are about 35 dB and 0.1 s, respectively. The polarization angle is derived from two-channel outputs of the crossed-Yagi antenna by using a goniometer. Variation of the polarization angle results from the Faraday rotation which the radiowave suffers during its passage of the ionosphere. Total electron content along the radio path can be derived from this measurement. The wavefield intensity and polarization angle were recorded both on chart recorder and analog magnetic tape.

2.4.2. Arrangement

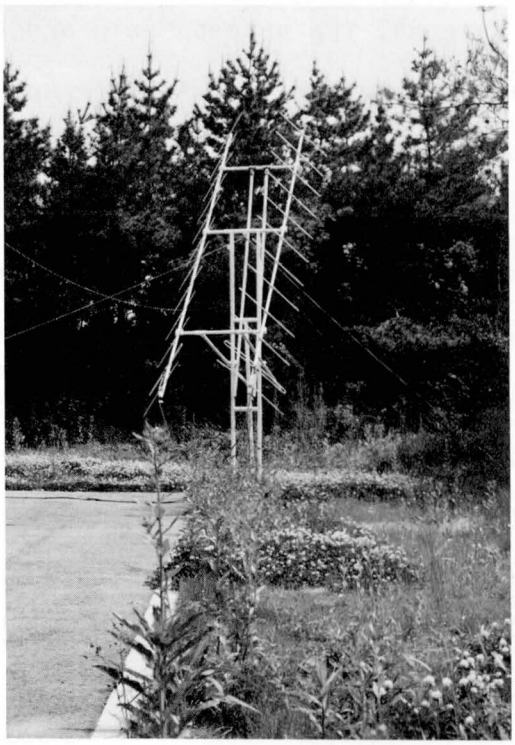

Fig. 2.7. Photograph of crossed-Yagi antenna.

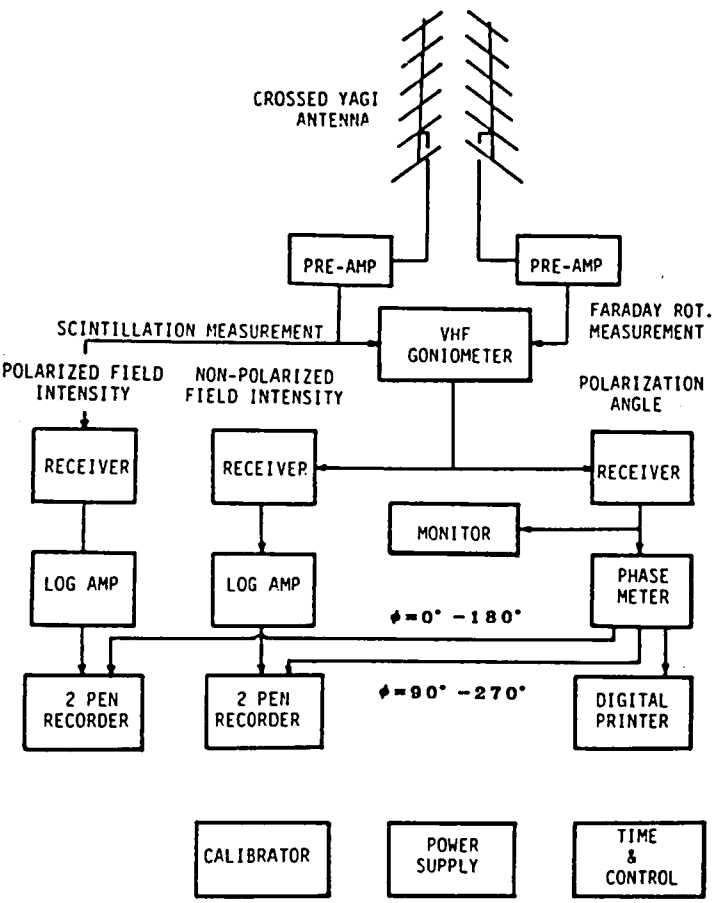

Fig. 2.8. Block diagram of crossed-Yagi antenna and receiver.

The observation site is in the campus of Hiraiso Branch, Radio Research Laboratory. Figure 2.9 shows the location of Hiraiso together with the radio propagation path from the geostationary satellite ETS-2 and sub-ionospheric point P_s at 300-km height on the path. Other observation stations of which data will be cited in the present dissertation are also shown in Figure 2.9. They are Kokubunji, Yamagawa, Okinawa (ionogram), and Kakioka (geomagnetism). The locations of these stations are listed in Table 2.1.

Figure 2.10 shows the relative antenna locations at Hiraiso and the directions of the 136.112 MHz radio path from ETS-2. Crossed-Yagi antennas were located at S (south) and E (east), and a helical antenna at W (west). The separation of each pair of antennas is about 200 m. The polarization angle was measured at S; other two (E and W) were only for wavefield strength measurement. The elevation and azimuth angles of the radio path on the ground are 47° and 197° (south-southwest), respectively. The radio path intersects the geomagnetic field lines with small angles of about 15° at 300 km height, where the dip angle is 46° (49° on the ground).

In a three-antenna measurement, movement of the ionospheric irregularities on a plane perpendicular to the radio path can be determined from time lags among three scintillation records. Therefore, we can obtain drift velocity in the S'E'W' plane (observation plane) which is a projection of the SEW plane onto a

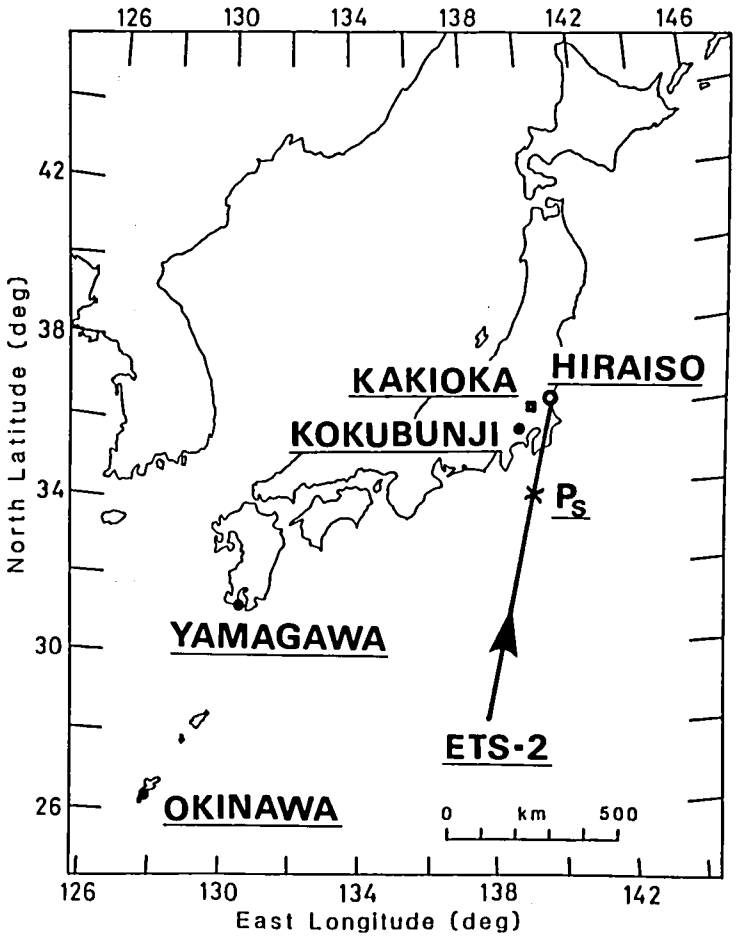

Fig. 2.9. Locations of observation sites. Scintillation observation site Hiraiso is shown together with the radio path from ETS-2 and sub-ionospheric point P_S at 300 km height on the path. Other stations are Kokubunji, Yamagawa, and Okinawa (ionogram), and Kakioka (geomagnetism). The longitudes and latitudes of these points are listed in Table 2.1.

Table 2.1. Longitudes and latitudes of various stations shown in Fig. 2.9.

Station	Geographic Longitude	Geographic Latitude	Geomagnetic Longitude	Geomagnetic Latitude
Hiraiso	140° 37´ E	36° 22´ N	206.8°	26.3° N
Sub-ionospheric point P_S	139° 45´ E	34° 04´ N	205.9°	23.8° N
Kokubunji	139° 29´ E	35° 42´ N	205.8°	25.5° N
Yamagawa	130° 37´ E	31° 12´ N	198.3°	20.4° N
Okinawa	127° 48´ E	26° 17´ N	196.0°	15.3° N
Kakioka	140° 11´ E	36° 14´ N	206.0°	26.0° N

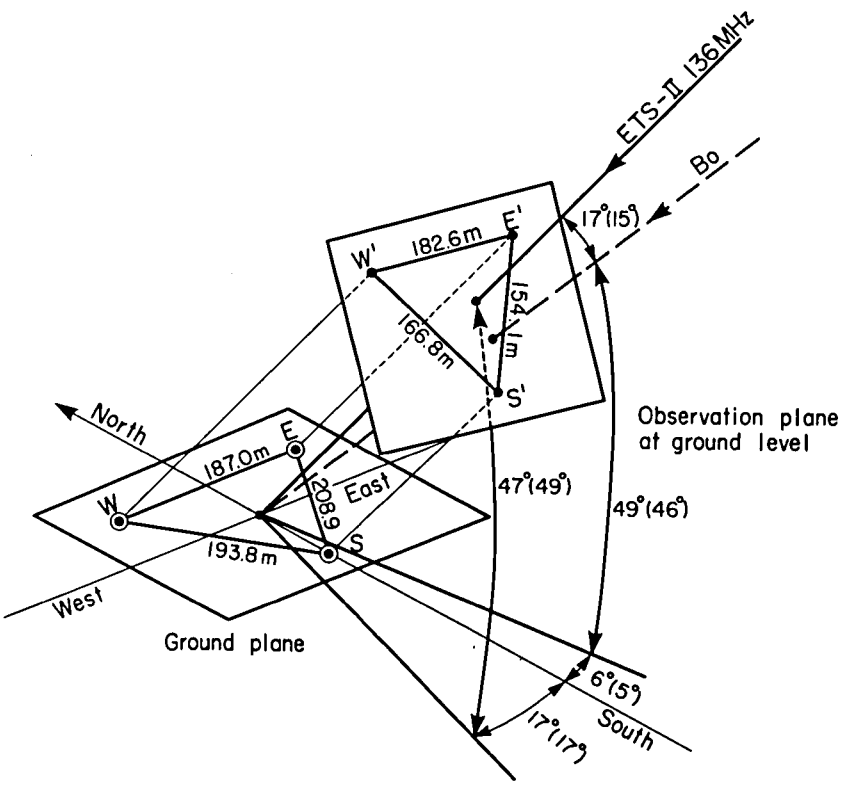

Fig. 2.10. Relative antenna locations (S, E, and W) at Hiraiso, directions of radio path from ETS-2, and geomagnetic field line vector (B_o). Angles of these vectors both on the ground and at 300 km height sub-ionospheric point (in brackets) are shown. N denotes geographic north. Projection of a triangle SEW on the ground onto the plane perpendicular to the radio path makes a triangle S'E'W' in the observation plane.

plane normal to the radio path.

2.5. DATA PROCESSING AND EXAMPLE OF RESULTS

2.5.1. Data processing

Signal levels at 136 MHz received by the three antennas were stored on analog magnetic tape and then digitized every 0.125 s for computer analysis. During scintillations, three auto-correlation and three cross-correlation functions were computed every 4 min (actual data segment is 3.2 min) by means of the conventional method. These sampling time and data segments were properly selected in order to hold the scintillation fluctuations of which the dominant frequency spectra lie between 0.01 and 1 Hz.

The method of data processing was already described in 2.2 and 2.3. Since the ionospheric irregularities are considered to have significant anisotropic feature, it is main objective to obtain the shape of them in the analysis. Following the procedure by Kent and Koster [1966], analysis was made for each data segment (3.2 min). As was discussed previously, it is assumed that a surface of constant correlation coefficient in a space (two-dimensional) and time coordinate system is ellipsoid [Briggs, 1968]. Contours of constant correlation coefficients on

the observation plane at ground level (S'E'W') and then drift velocities and characteristic random velocities were derived. Because of significant anisotropic features of the irregularities, it is sometimes difficult to determine accurately the drift velocity and characteristic velocity. In this case, therefore, the approximate computation method, which has been discussed in sections 2.3.5 and 2.3.6, was employed to derive the velocities. In the following, examples of the data processing and the results are shown. The accuracy of the results and the adequacy of the approximation are also examined.

2.5.2. Example of observational data

An example of scintillation records obtained at three-spaced receivers during 0019 - 0023 LT on July 22, 1982 is shown in Figure 2.11. Three scintillation records at the S, E, and W antennas are shown. The ordinate shows relative received-power in dB. It can be seen that the time variations in three records are almost similar to one another. Namely, it is expected that the correlations among these records are high at the separations of about 200 m. Corresponding points on the records are connected with broken lines. Indeed, there are time shifts of several seconds among them. These time shifts are considered to result from the motions of the ionospheric irregularities.

Figure 2.12 shows example of a set of correlation functions

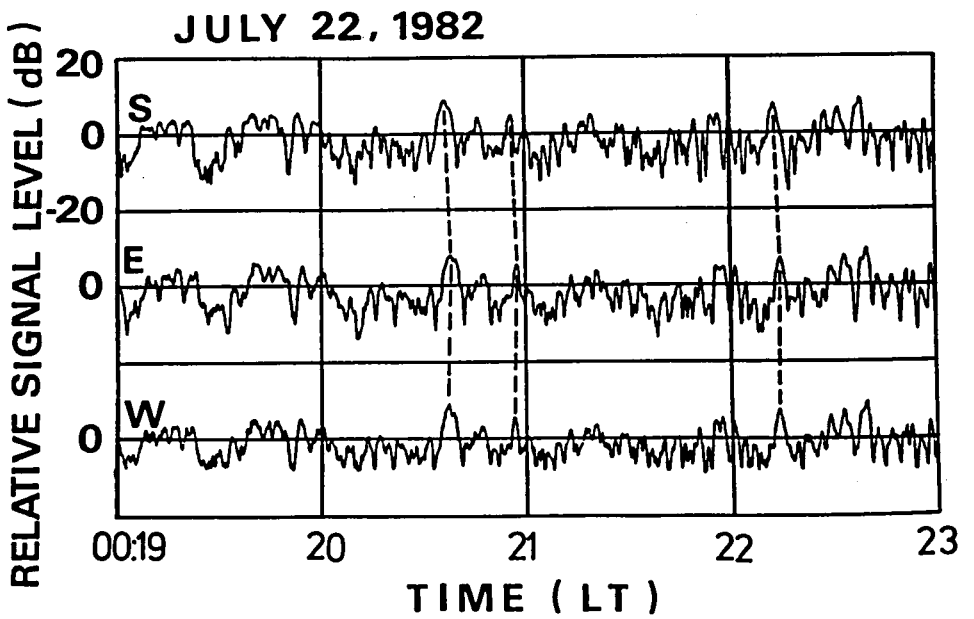

Fig. 2.11. Example of scintillation records obtained at three-spaced receivers (S, E, and W) during 0019-0023 LT on July 22, 1982. Corresponding points on the records are connected one another by broken lines.

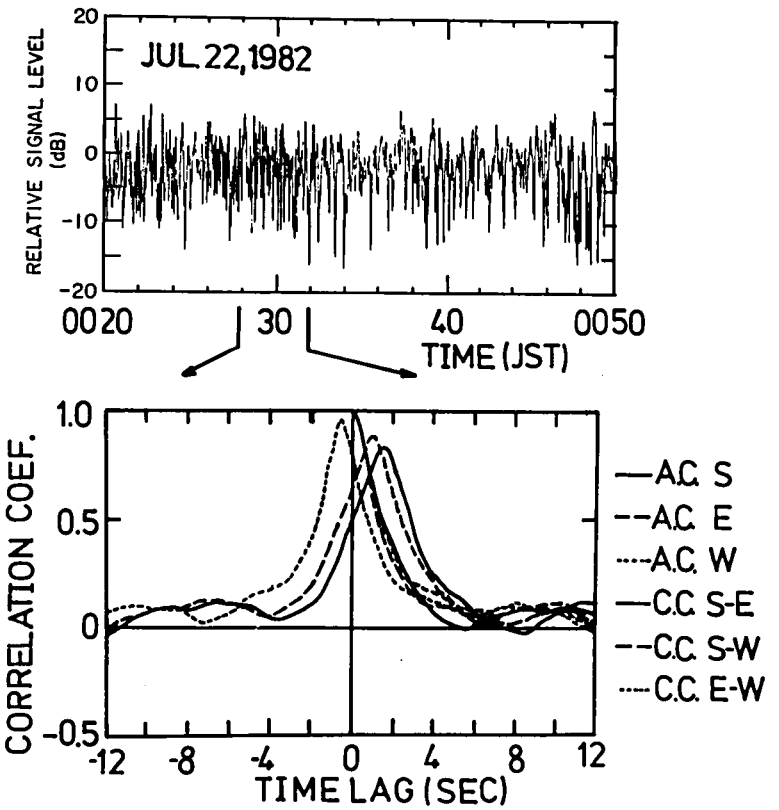

Fig. 2.12. Examples of scintillation record and computed correlation functions. The record was obtained by S antenna during a period 0020-0050 LT on July 22, 1982. Three auto-correlation functions of S, E, and W antennas, and three cross-correlation functions of three pairs of antennas are displayed in the lower panel.

together with scintillation record, which was obtained by the S antenna during a period from 0020 to 0050 LT on July 22, 1982. Six correlation curves are drawn in the lower panel; they are three auto-correlation functions of the S, E, and W antennas, and three cross-correlation functions of pairs of S and E, S and W, and E and W. All correlation functions were computed during the period from 0028 to 0032 LT; the period is indicated on the abscissa in the upper panel. As shown in the lower panel, three auto-correlation functions are almost similar to one another, and the peak values of the cross-correlation functions are larger than 0.7. These are also true for most of other observation periods.

2.5.3. Example of results and estimation of accuracy

Figure 2.13 shows the result of correlation analysis for the scintillations during 00-04 h LT on July 23, 1982. The upper panel shows the chart record of the event. From top to bottom in the lower panel, time variations in S_4 index, axial ratio and minor radius of the irregularity pattern ellipse, pattern ellipse itself, four kinds of velocities relating to the motion of the irregularities, and characteristic random velocity V_c/V are shown every 8 min. Each data point comes from the analysis of 3.2 min data segment and is plotted only when all peak values of three cross-correlation functions are larger than 0.7.

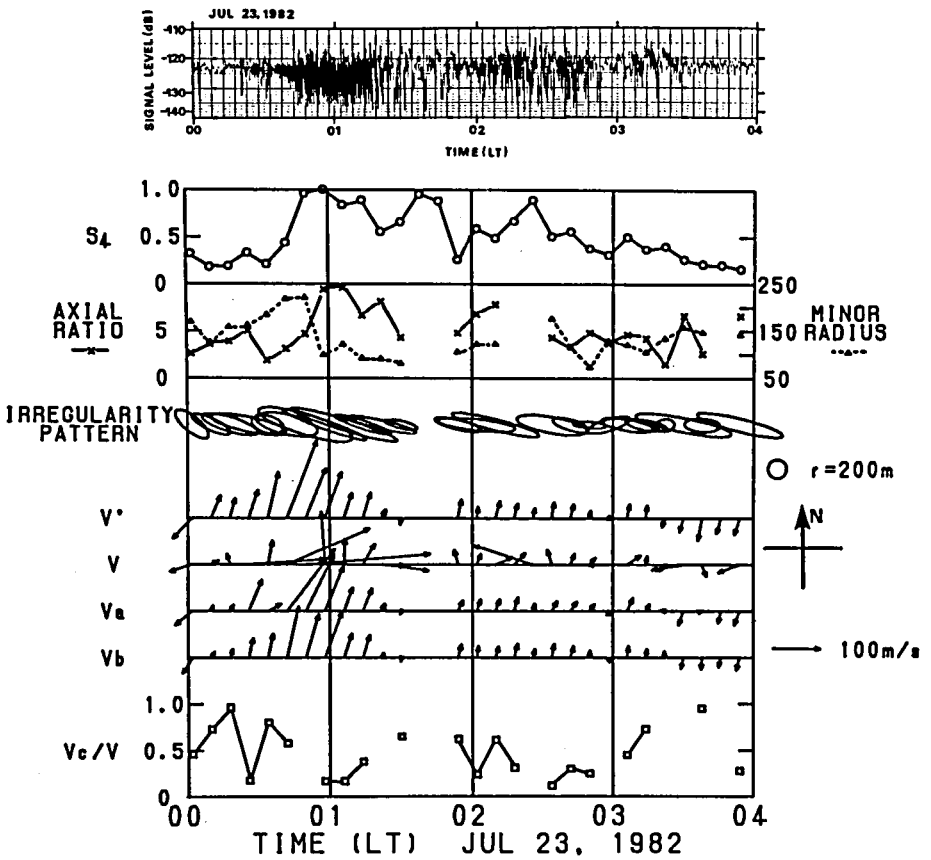

Fig. 2.13. Example of results of the correlation analysis for the scintillations during 00-04 LT on July 23, 1982. From top to bottom, time variations in scintillation chart record, S_4 index, axial ratio and minor radius of the irregularities, irregularity ellipse, four kinds of velocity vectors, and V_c/V are shown. Velocity vectors represent apparent velocity V', drift velocity V, and approximated drift velocity V_a and V_b.

The irregularity pattern ellipse represents the locus at which the spatial correlation coefficient falls to 0.5. This is the irregularity form projected onto the observation plane and is considered to represent also the irregularity form in the ionosphere. This stems from assumptions that the radiowave from the geostationary satellite can be regarded as the plane wave and that the angle of radiowave refraction is negligibly small except a case of extremely intense scintillation. References to the direction (N denotes the geographic north) and scale size of the irregularity pattern are shown in the right side and at the top of panel, respectively. The axial ratio and minor radius of the ellipse are separately shown. Most ellipses seem to be elongated almost in the same direction. Although the interpretation of this result will be given later, it can be noted here that elliptic shapes are determined stably in the data processing. Also noted is that the values of axial ratios themselves are not so reliable in the cases of large axial ratios.

Four kinds of velocities derived from the analysis are explained below. They are the apparent velocity V', drift velocity V, approximate drift components along the minor axis of the ellipse V_a and V_b. The definitions of V_a and V_b were given in equations (2.42) and (2.43), respectively. Three velocities except V show an almost identical and slowly-varying time variation. They are directed northward or northeastward during 0010 to 0314 LT, then directed southward. These directions are

always along the direction perpendicular to the major axis of the ellipse. As has been mentioned previously (see 2.2.2), V' does not represent the real drift velocity of the irregularities but V is the desired quantity. However, V shows large scatter in time variation and seems not reliable.

The algorithm to obtain V is sensitive to the axial ratio and becomes unstable especially for large axial ratio. The reason for this has been already mentioned in the previous chapter. In fact, it is uncertain to say that the drift component of the irregularities themselves parallel to the elongation exists actually when the axial ratio is extremely large. Indeed, it would be meaningless when the axial ratio becomes infinite.

V_a and V_b give approximate components perpendicular to the major axis of the irregularity ellipse. In most cases, these two variables are almost coincident with each other. They are also almost coincident with the apparent velocity V' although the magnitudes of V_a and V_b are a little smaller than that of V'. It seems proper to obtain V_a or V_b in place of V in the analysis. Hence, average value of V_a and V_b is used as a drift velocity hereafter. It is noted that the drift velocity coming from this expression does not have a component along the major axis of the ellipse. The difficulty to obtain the drift component along the major axis was already pointed out in the correlation analysis of elongated irregularities [Kent and Koster, 1966; Bramley and Browning, 1978]. It may be a future problem to derive this

component accurately. In addition, it seems interesting to consider the physical meaning of the drift component along the elongation in a case of significantly large axial ratio.

The bottom panel in Figure 2.13 shows the ratio of the characteristic random velocity to drift velocity, V_c/V; only the cases of $0 < V_c/V < 1.5$ is shown. This ratio is also unstable by the reason similar to the case of V. It is seen that relatively small values of V_c/V (less than 0.5) are obtained during the period of stable scintillations, while large and over-ranged values are obtained mostly during the period with rapidly change of scintillation amplitude and pitch.

2.6. SUMMARY

This chapter is summarized as follows: (1) Basic concept of the correlation analysis for spatially one-dimensional and two-dimensional isotropic irregularities has been reviewed. (2) The practical method of the correlation analysis for two-dimensional anisotropic irregularities has been described. Irregularity forms as well as irregularity drifts can be derived by this method. (3) Arrangement of the instruments has been shown. (4) Practical procedure of the data processing has been introduced. It is shown that the drift velocity V is difficult to be determined accurately for the irregularities with large axial

ratios. It is recommended that for such irregularities average of V_a and V_b should be used instead of V.

CHAPTER 3

RESULTS OF SPACED-RECEIVER SCINTILLATION MEASUREMENTS

3.1. INTRODUCTION

Measurements of ionospheric scintillations using spaced-receivers have provided much information on the structures and movements of irregularities. Many articles describing ionospheric drifts deduced from radio star or satellite radio wave scintillations have been presented. At the equator, eastward drift velocities between 30 and 150 m/s were obtained during nighttime hours [Koster, 1963; Yeh et al, 1981]. In midlatitudes, Bramley and Browning [1978] obtained drift velocity of 90 m/s with a predominant northwest direction.

It has been found that the ionospheric irregularities producing nighttime scintillations are field-aligned and have large axial ratios in the F-region heights; axial ratios obtained are beyond 7 at the equator [Koster, 1963; Kent and Koster, 1966] and beyond 5 in the mid-latitude [Moorcroft and Arima, 1972; Bramley and Browning, 1978; MacDougall, 1981]. In contrast, daytime scintillations are caused by weakly field-aligned irregularities (axial ratio is about 2) in the E-region [Bramley and Browning, 1978]. Sinno and Minakoshi [1983] have certified

that the scintillations over Japan are intensified when the radio path is parallel to the geomagnetic field lines, and have suggested that these scintillations were produced by field-aligned irregularities.

These results are quite useful to investigate the behavior and dynamics of the irregularities. In addition, spatial characteristics of the irregularities can provide valuable information for analyzing the radio scattering mechanism due to the irregularities. From this analysis it will be possible to construct an ionospheric irregularity model and to evaluate the effects of the irregularities on various radiowaves propagating through the ionosphere. In this chapter, two kinds of observational results of the midlatitude F-region irregularities obtained during June-July 1982 are presented; one is under geomagnetically quiet condition [Kumagai and Ogawa, 1986] and the other under disturbed condition [Kumagai et al., 1986]. In the former observation, time evolution of nighttime irregularities and some statistics of both drifts and field-aligned structure of irregularities are presented. It will be shown that these results are useful to interpret the scintillation mechanism and to construct an irregularity model. In the latter observation, some interesting features of the irregularities are presented.

3.2. RESULTS UNDER GEOMAGNETICALLY QUIET CONDITIONS

3.2.1. Data periods

In Japan, nighttime scintillations at 136 MHz appear most frequently in June and July and may last throughout the night [Sinno and Kan, 1980]. The probability of scintillation occurrence in this season is larger for geomagnetically quiet condition than for disturbed condition [Kumagai, 1986a]. We analyzed seven nighttime scintillation events at 136 MHz which occurred in June and July 1982. The data periods are listed in Table 3.1 together with both the averaged geomagnetic K index (three-hour-range) obtained at Kakioka Magnetic Observatory (see Figure 2.9) and the averaged S_4 index corresponding to each period. The K indices were less than or equal to 3 through the whole period except during event No. 5 for which K reached the value 4 once. Therefore, we can investigate the scintillations and irregularity characteristics under almost geomagnetically quiet conditions. During all the data periods, drifts and irregularity pattern parameters were computed every eight minutes (average of two data segments). First, time evolutions of the scintillations and irregularity characteristics of two events (Nos. 4 and 6) are shown, and then some statistical features are given.

Table 3.1. A list of periods of seven scintillation events

No.	Year	Start time(LT)	End time(LT)	$\overline{K}$*	$\overline{S_4}$ *
1	1982	3 June 2100	- 4 June 0440	1.7	0.53
2	1982	7 June 2030	- 8 June 0530	1.7	0.50
3	1982	26 June 2000	- 27 June 0350	2.5	0.69
4	1982	5 July 2110	- 6 July 0500	1.3	0.54
5	1982	6 July 2040	- 7 July 0600	3.3	0.58
6	1982	21 July 1840	- 22 July 0600	2.0	0.56
7	1982	22 July 2100	- 23 July 0500	2.7	0.37

* $\overline{K}$ and $\overline{S_4}$ are the averaged geomagnetic K index obtained at Kakioka and the averaged S_4 index, respectively, during each data period.

3.2.2. Scintillation event on July 21-22, 1982

(a) Scintillation record

Time evolution of the 136 MHz scintillation event on July 21-22, 1982 is shown in Figure 3.1, where from top to bottom, total electron content (TEC) along the radio propagation path, scintillation signal level, h'F observed every 15 min at Kokubunji, drift velocity V, ellipse representing the irregularity form at the ground level (every 16 min), and S_4 index (every 8 min) are displayed. The TEC was obtained from the Faraday rotation method. Note that both V and irregularity pattern ellipse represent those on the observation plane (S'E'W') shown in Figure 2.9. In the second panel, occurrence of spread-F at Kokubunji is also shown by a horizontal bar. It should be noted that Kokubunji is about 200 km north of the presumed scintillation observing point (34.0°N, 139.4°E).

Strong scintillations started at 1845 LT and lasted until 0600 LT. The maximum amplitude of the scintillations is about 20 dB peak-to-peak (S_4 index $\sim$ 1). It is obtained that the scintillation amplitude does not increase without limit but it seems to be saturated around $S_4 \sim 1$. The saturation may be an indication that the multiple scattering plays an important role in the scintillation production [Liu et al., 1974]. Spread-F was observed from 2330 LT through 0430 LT. The scintillation event seems to be composed of two parts, i.e., premidnight and

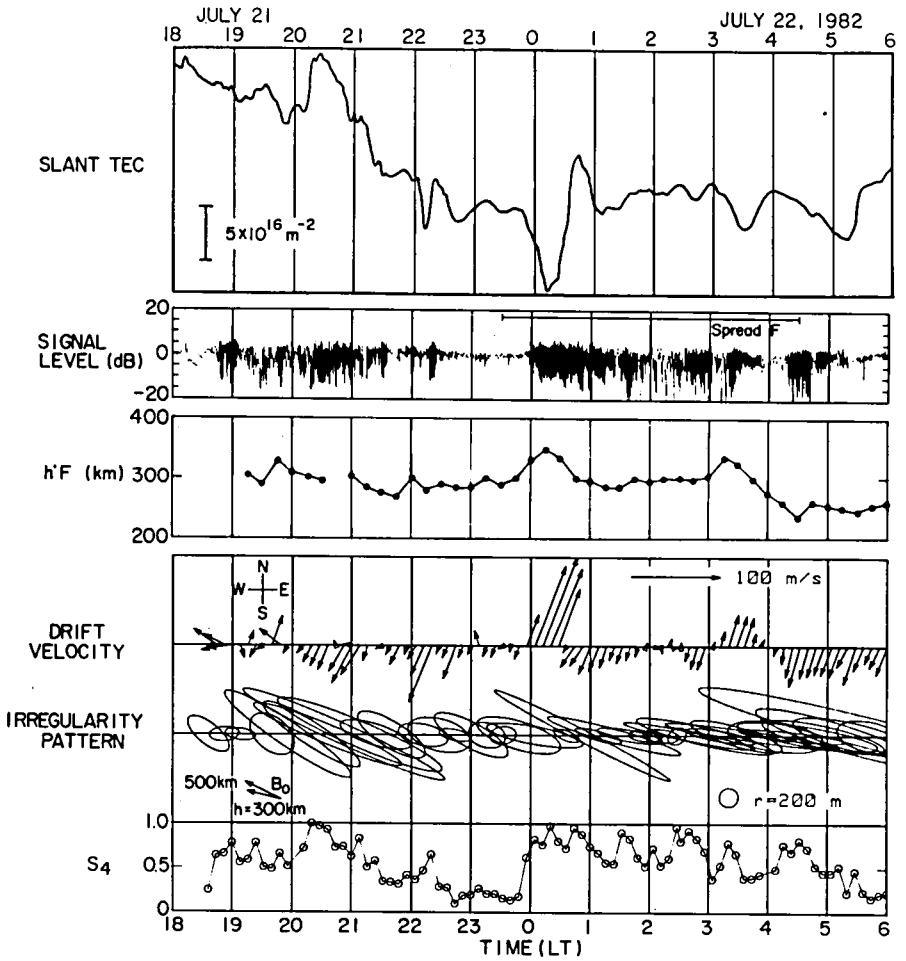

Fig. 3.1. Time evolution of scintillation event on July 21-22, 1982. From top to bottom, time variations in total electron content (TEC) along the radio path, 136 MHz scintillation record, h'F obtained from Kokubunji ionograms, drift velocity vector (every 8 min), irregularity pattern ellipse (every 16 min), and S_4 index (every 8 min) are shown. Occurrence of spread-F at Kokubunji is also shown in the second panel by a horizontal bar.

postmidnight hours. The scintillations in the postmidnight hours correspond well to the appearance of spread-F. However, this is not the case for the premidnight scintillations, possibly due to the absence of irregularities over Kokubunji. Spread-F was surely observed in the area south of Kokubunji, e.g., at Yamagawa during 1930-0545 LT and Okinawa during 2000-2245 LT and 0015-0345 LT. Strong sporadic-E (f_oE_s>12 MHz) was also seen on the Kokubunji ionograms during 1800-1930 and 2030-2100 LT. Therefore, the premidnight scintillations may have been somewhat affected by the sporadic-E layer.

(b) Variations in TEC and drift velocity

TEC fluctuations were observed during the occurrence of scintillations, which is not unusual over Japan [Sinno and Kan, 1978] and over Arecibo [Kersley, et al., 1980]. Especially, a sharp depression of TEC appearing around 0015 LT seems to mark the beginning of the second part of the scintillations. The drift velocity V in Figure 3.1 (N denotes geographical north) is an approximate one and represents a component perpendicular to the major axis of the irregularity ellipse (see 2.5.3). Since the radio paths intersect the geomagnetic field lines with small angles (15°), the drift vector in the Figure can be regarded as a component almost normal to the geomagnetic field lines. From 20 h to 0 h LT, the drifts were essentially directed southwestward and most of the drift velocities are less than 30 m/s. In the

postmidnight hours, there are two periods (0000-0032 LT and 0308-0356 LT) for which the drifts were directed northward. Especially, high northward drift velocities (about 100 m/s) in association with both the strong and high-pitch scintillations, and the deep depression of TEC were observed during 0000-0032 LT. The northward drifts during 0308-0356 LT had a mean velocity of 23 m/s. Outside these periods in the postmidnight hours, the drifts were directed southward or southwestward with velocities essentially less than 40 m/s.

Prominent reversals of the drift directions appeared four times; twice from southward to northward and twice from northward to southward. Among them, three reversals at 2356, 0304, and 0400 LT happened when the scintillations became temporarily weak. Around these times, the irregularity motion was decelerated first, then stopped, and finally accelerated in a reverse direction. On the contrary, the reversal from northward to southward at 0036 LT happened in the midst of strong scintillations. The sharp increase in TEC observed around this time may be related to this reversal. This kind of reversal will be further discussed in 3.2.4. For the two periods when the drifts were directed northward, h'F is certainly lifted up and TEC is depressed, suggesting that the derived north-south drift velocity may partly reflect a vertical movement of the ionosphere [Basu et al., 1981].

Characteristic velocity V_c, which represents a random motion

or a random change of the irregularities, was also calculated in the analysis. The mean value of V_c/V was 0.34 during the whole scintillation event in Figure 3.1.

(c) Irregularity characteristics

Most ellipses shown in Figure 3.1 have long major axes which are essentially aligned along the same direction. Figure 3.2 presents a schematic picture showing the relation between the ellipses in Figure 3.1 and the ionospheric irregularity configuration. We can observe a projection of the irregularity onto the observation plane in Figure 2.9. The directions of the geomagnetic field lines projected onto the observation plane at 300 km and 500 km heights are indicated in Figure 3.1; their azimuth (from north to east) are 283.3° (300 km) and 296.1° (500 km). Most of the major axis directions of the ellipses coincide with the projected geomagnetic field lines, indicating that the irregularities in the ionosphere extend along the geomagnetic field lines. The axial ratio of the ellipse in Figure 3.1 amounts to 7 during strong scintillations. In order to obtain the actual axial ratio of the field-aligned irregularities, a factor of 3.9 (=1/sin15°) should be multiplied.

Table 3.2 compares the averaged parameters of the irregularity pattern ellipses for premidnight and postmidnight hours. The value of axial ratio is shown for two cases: on the observation plane and in the ionosphere. Considerable differences

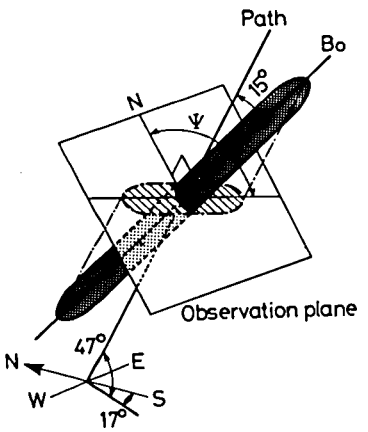

Fig. 3.2. Relation between actual field-aligned irregularity configuration (dotted area) and irregularity pattern projected onto the observation plane; plane perpendicular to the radio path (hatched area). The angle between the radio path and the geomagnetic field lines B_o is 15°. Ψ represents azimuth angle in the observation plane.

Table 3.2. Mean values of diffraction pattern parameters on 21-22 July and 5-6 July, 1982.

	21-22 July		5-6 July	
	Premidnight	Postmidnight	Premidnight	Postmidnight
Axial ratio	3.9 (15.0)*	7.5 (28.9)*	9.1 (35.3)*	6.6 (25.5)*
Minor radius(m)	230.9	173.4	145.4	158.6
Azimuth angle of major axis(deg)	106.6	101.2	106.7	100.9

* Actual axial ratio.

are discernible; axial ratio is larger and minor radius is smaller in the postmidnight than in the premidnight. Namely, the irregularities in the postmidnight hours are more field aligned than those in the premidnight hours. The azimuth angle of major axis becomes a little smaller in the postmidnight than in the premidnight hours, which may suggest that under an assumption of a strict field-aligned nature for the irregularities, their height decreased in the postmidnight hours.

Since the axial ratio of the irregularity pattern is large, it may be impossible to obtain the accurate drift velocity using this correlation analysis. Therefore, only the components perpendicular to the major axes of the ellipses have been shown here. Under this restriction, drifts are along the north-south direction. In reality, we do not know whether a drift component parallel to the major axis of the irregularities with extremely large axial ratio is meaningful or not. It is necessary to measure east-west drift components by using a different technique and to clarify whether they are important or not.

3.2.3. Scintillation event on July 5-6, 1982

Results of the scintillation event on July 5-6, 1982 are shown in Figure 3.3 using the same format as that of Figure 3.1. Strong scintillations occurred during several periods and lasted until 0430 LT. Although spread-F was observed on the Kokubunji

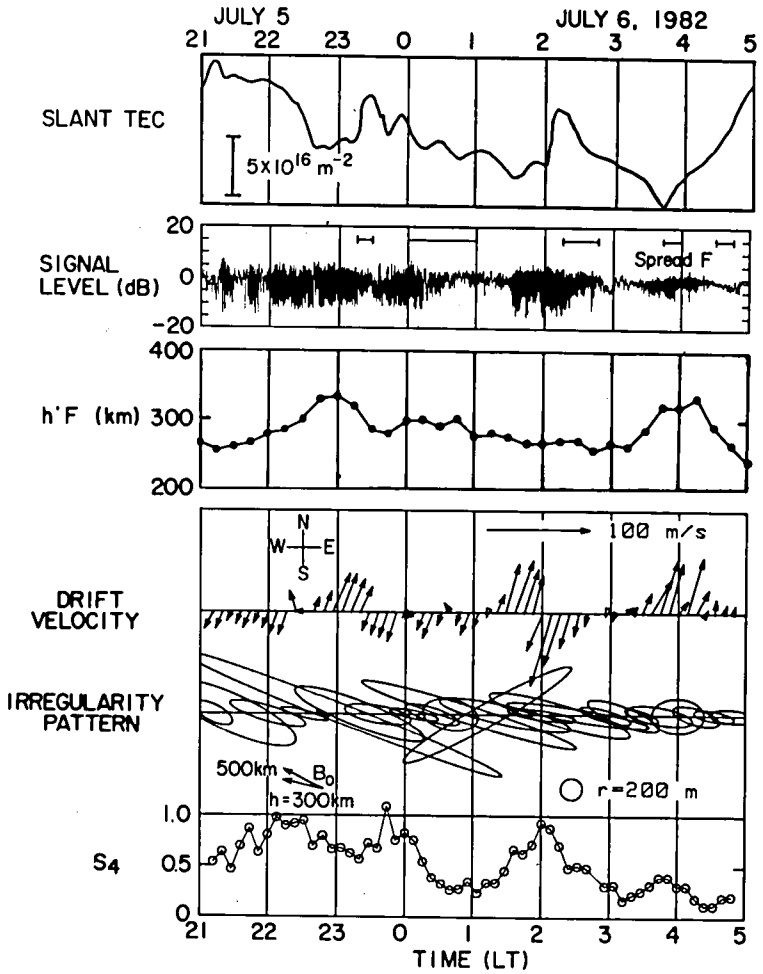

Fig. 3.3. Same as Fig. 3.1, but for scintillation event on July 5-6, 1982.

ionograms, it was sporadic and did not always correspond to the appearance of strong scintillations. The lack of correspondence may be due to the long distance (200 km) between the two observing points: Kokubunji and ETS-2 sub-ionospheric point. Sporadic-E was also observed at Kokubunji at 2100 and 2115 LT but f_oE_s was less than 9 MHz.

The drift velocities changed their direction in a quasi-periodic manner. The magnitude of the drift velocities are essentially less than 50 m/s. It is interesting to note that the correspondence between the northward drifts and the uplift of h'F was seen for two periods: 2336-2324 LT and 0308-0500 LT. However, this is not true for the period 0120-0200 LT. It is supposed that the northward drifts during this period happened only in a localized area around the sub-ionospheric point of ETS-2. At 0200 LT, the drift direction changed from northward to southward in the midst of strong scintillations. At the same time, a steep increase in TEC started. This situation is similar to the reversal at 0036 LT on July 22 (Figure 3.1). From Figure 3.1 and 3.3, it can be pointed out that the northward drifts are associated with the depletion of TEC and vice versa.

The mean value of the normalized characteristic velocity V_c/V_o for the whole scintillation event in Figures 3.1 and 3.3 is 0.32, with upper and lower quartile values of 0.45 and 0.20. These values are almost similar to or a little larger than those obtained previously (Koster, 1963; Bramley and Browning, 1978).

Thus, we can conclude that in most cases the random motions of the irregularities, although non-negligible, do not play an important role in giving rise to the scintillations.

The ellipses of the irregularity patterns shown in Figure 3.3 also indicate that the irregularities have well-developed field-aligned structures. Some parameters of the ellipses are listed in Table 3.2. In contrast to the event on July 21-22, the differences in axial ratio and minor radius between premidnight and postmidnight hours are not large. The azimuth angle of the major axis decreases from 106.7° in the premidnight hours to 100.9° in the postmidnight hours. This change is similar to the event on July 21-22 and suggests a lowering of the irregularity height with time.

3.2.4. Abrupt reversal of drift

Reversals of the drift direction from southward to northward or from northward to southward were often observed during the nighttime scintillations. Most of them appeared when the scintillations became temporarily weak (2356, 0304, and 0400 LT on July 21-22, and 2324, 0116, and 0308 LT on July 5-6, 1982). There occasionally happened abrupt reversals of the drifts (0036 LT on July 22 and 0200 LT on July 6) in the midst of the strong scintillations. Salient features of these abrupt reversals are as follows: (1) reversal from northward to southward, (2) reversal

during strong and high-pitch scintillations, and (3) reversal accompanied by steep increase in TEC.

Figure 3.4 shows the enlarged scintillation record and the cross-correlation functions obtained every two minutes from S and E antenna signals during 0140-0220 LT on July 6, 1982 (see Figure 3.3). A negative lag time of the peak of the cross-correlation function corresponds to northward drift and vice versa. The reversal occurred between 0200 and 0206 LT. The cross-correlation curves at 0202 and 0204 LT are disturbed while others have a clear peak in the correlation. In the upper panel of Figure 3.4, no peculiar change or discontinuity in the scintillation record can be seen during the reversal. These situations are also applicable to the abrupt reversal around 0036 LT on July 22 (not shown).

As has been pointed out above, the rapid reversal of the drift direction from northward (upward) to southward (downward) is accompanied by a rapid increase in TEC. This association seems to be similar to the midnight collapse over Arecibo described by Basu et al. [1981]. We have also noted that the northward (upward) drifts are associated with the depletion of TEC. Basu et al. [1981] interpreted that the variation in TEC in the midnight collapse observed by the Faraday rotation method was caused by the up-down movement of the F-layer. Namely, the Faraday rotation is controlled by the local magnetic field strength. However, TEC variations observed here are much larger than those observed in

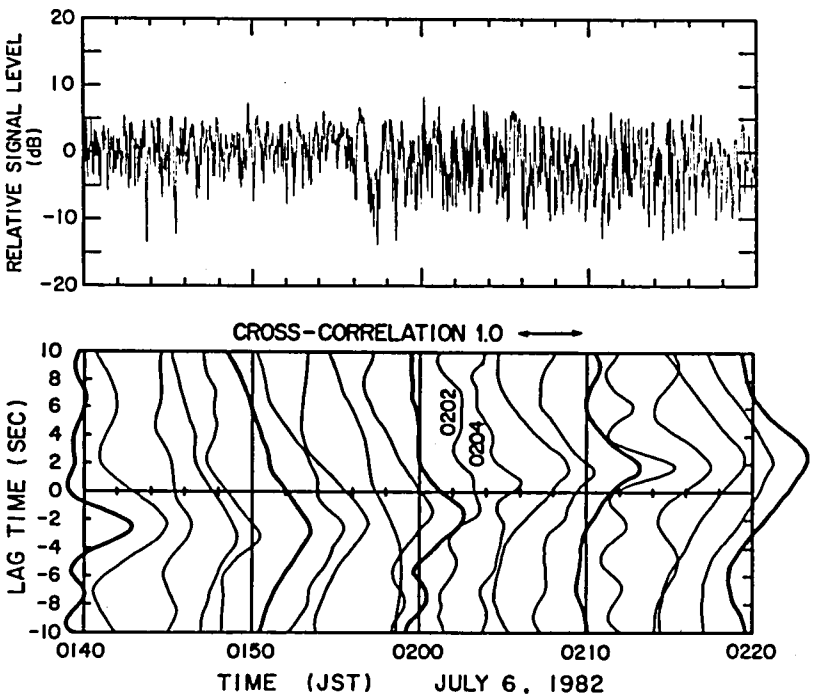

Fig. 3.4. Scintillation record at S antenna and time variation of cross-correlation function of signals at S and E antennas during 0140-0220 LT on July 6, 1982. Cross-correlation functions are shown every 2 min (thick line for every 10 min). Negative lag time corresponds to northward drift and vice versa.

the midnight collapse. In order to interpret these variations, it seems more important to consider the large scale structure in which high-density region moves downward and the low-density region does upward. A mechanism for driving these movements may be similar to that in the equatorial bubbles [Woodman and La Hoz, 1976; Fejer and Kelley, 1980].

Perkins [1973] proposed a mechanism for explaining midlatitude spread-F. In the presence of north-south electric field in addition to the eastward electric field (or equatorward neutral wind), a plasma instability grows resulting in the formation rising and falling sheet of ionization. The Perkins instability seems applicable to a part of our observations because, as shown in Figures 3.1 and 3.3, strong scintillations appear for the upward (northward in our case) motion, which can be related to the eastward electric field. However, the irregularities (scintillations) appear during for the downward (southward) motion corresponding to the westward electric field. The role of medium-scale gravity waves may also be important for explaining these irregularities [Kersley et al., 1980].

3.2.5. Distribution of drift velocity

Using the whole data obtained during the seven events listed in Table 3.1, statistical distributions of the drift velocities were investigated. A total of 436 drift velocity values was

computed (every 8 min). Figure 3.5 shows the azimuthal distributions of the drift velocities on the observation plane for premidnight hours (Figure 3.5a) and postmidnight hours (Figure 3.5b). Azimuths are divided into intervals of 15° and velocities into intervals of 20 m/s.

Before midnight, 47 % of the drifts concentrate in the azimuths of 195°-210° while the percentage of the northward drifts (0°-45°) is fairly small (14 %). The mean value of the drift velocities in the premidnight is 22.7 m/s for the northward drifts and 25.9 m/s for the southward drifts. The maximum velocity is less than 80 m/s. On the other hand, in the postmidnight hours, the percentage of the northward drifts (0°-45°) increases up to 36 % whereas that of the southward drifts (195°-210°) decreases to 41 %. The northward drifts are observed mainly during strong scintillations. Although high velocities (>80 m/s) appear at times, the mean value of the drift velocities in the postmidnight hours is almost similar to that in the premidnight hours: 26.3 m/s for the northward drifts and 19.6 m/s for the southward drifts. By considering that the north-south drifts may stem from vertical drifts, these averaged values of the velocities are essentially consistent with previous observations of vertical drifts using incoherent scatter radars [Evans, 1971; Taylor, 1974].

3.2.6. Statistics of irregularities

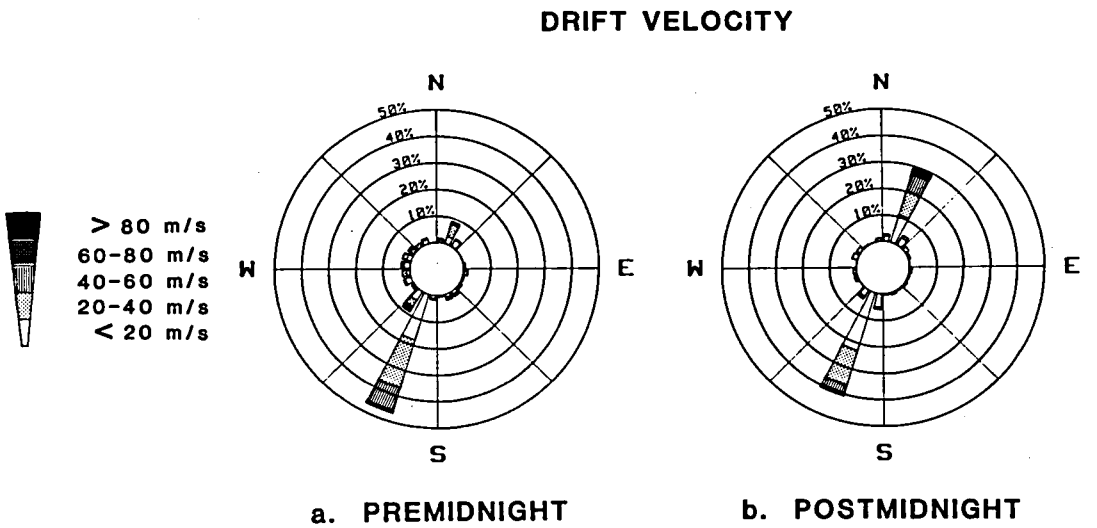

Fig. 3.5. Distributions of drift directions and drift velocities in the observation plane: (a) premidnight hours; (b) postmidnight hours. N denotes geographic north.

(a) Distribution of irregularity form

Azimuthal distributions of major axis directions (0°-180°) and axial ratios of the irregularity ellipses on the observation plane are shown in Figure 3.6. Azimuths are divided into intervals of 15° and axial ratios into intervals of 2.5. Most of the major axis angles lie within azimuths of 90°-135° for both premidnight hours (Figure 3.6a) and postmidnight hours (Figure 3.6b). However, the number of data with the azimuths nearer to 90° increases in the postmidnight hours. Mean azimuth angle of major axes is 106.8° in the premidnight hours and 102.3° in the postmidnight hours. The decrease in the major axis angle means the decrease in the irregularity height if the irregularities are field-aligned. According to the azimuths of the geomagnetic field lines projected onto the observation plane (examples at 300 km and 500 km heights are shown in Figures 3.1 and 3.3), the mean height of the irregularities is roughly estimated to be 350 km in the premidnight hours and to be lower than 300 km in the postmidnight hours. Mean axial ratios are 5.7 in the premidnight hours and 6.7 in the postmidnight hours. Namely, mean actual axial ratios of the field-aligned irregularities amount to 22 and 26, respectively.

(b) Dependence of irregularity form and drift velocity on S_4 index

Dependences of the axial ratio, minor radius and drift

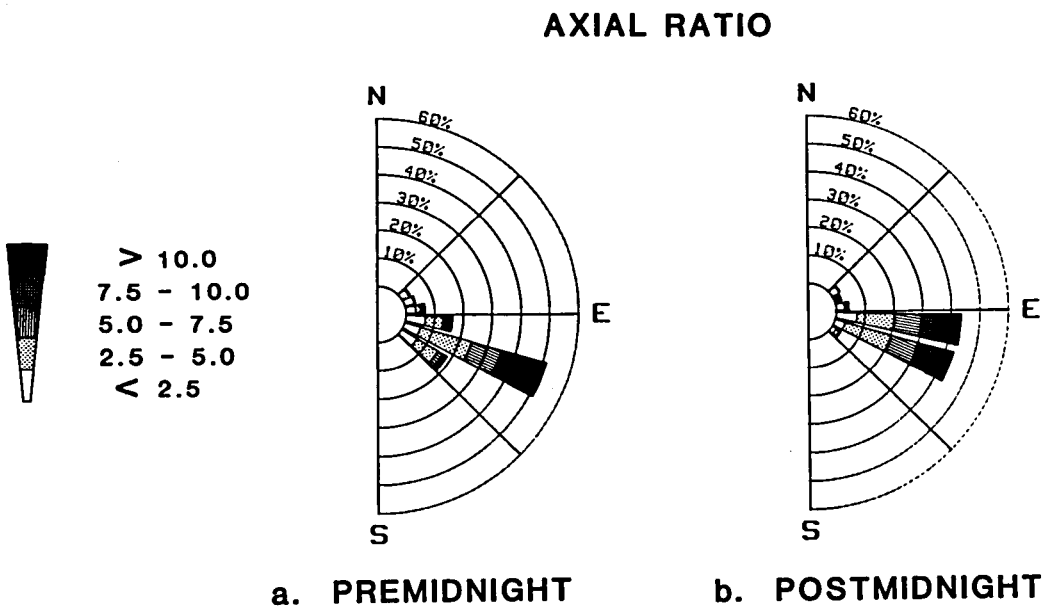

Fig. 3.6. Distributions of major axis directions and axial ratios of the irregularity pattern on the observation plane: (a) premidnight hours; (b) postmidnight hours.

velocity of the irregularities on S_4 index are shown in Figure 3.7. Where, S_4 indices are classified into six groups (every 0.2), and the mean value (full circle) and standard deviation (vertical bar) of each data set are shown. At the top of Figure 3.7, numbers of data in each class of S_4 are indicated. The mean axial ratio (Figure 3.7a) increases with increasing S_4 until S_4=1.0 where saturation seems to occur (the decrease in axial ratio for $1.0 < S_4 < 1.2$ seems meaningless because of small number of data). The average value of the axial ratio is 6.2, which corresponds to 24 for the actual field-aligned irregularities.

The minor radius (Figure 3.7b) tends to decrease with increasing S_4. The minor radius represents the transverse correlation distance. The decrease in the correlation distance with increasing scintillation intensity may be interpreted as a decorrelation effect resulting from the multiple scattering which becomes effective with increasing S_4 [Yeh et al., 1975]. The average value of the minor radius is 182 m. Values of the axial ratios and minor radii are essentially consistent with previous results obtained by Koster [1963] and Bramley and Browning [1978].

Figure 3.7c shows the S_4 dependence of the drift velocity. Although the standard deviation is large, a tendency of velocity to become faster with increasing S_4 (<1.0) is observed. Since the drifts are primarily derived from the electric field, this tendency may be an indication that stronger electric field exists

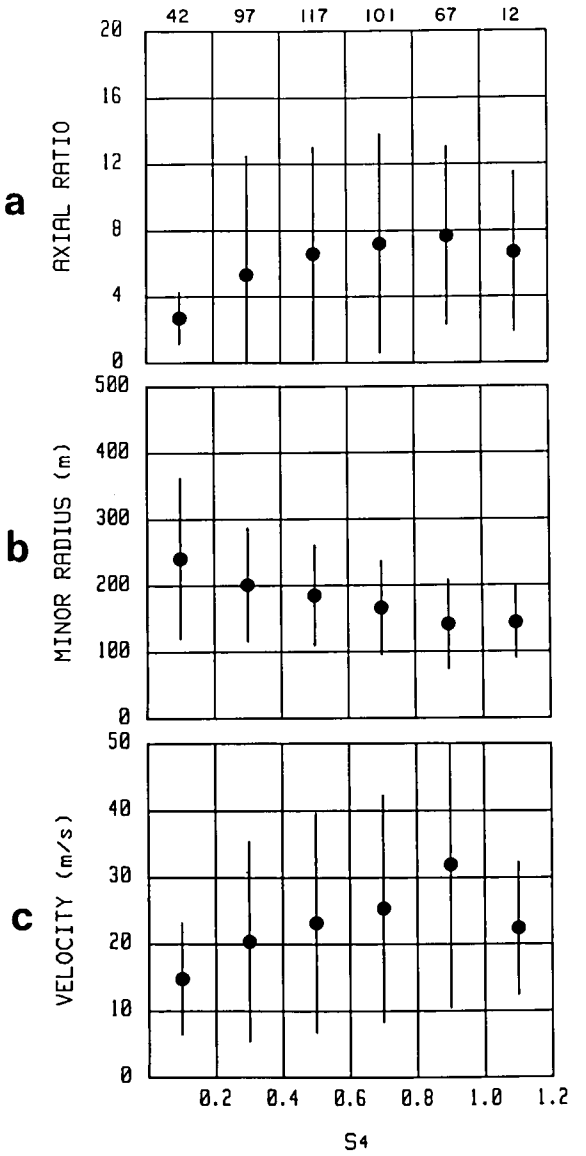

Fig. 3.7. Dependences of (a) axial ratio, (b) minor radius, and (c) drift velocity on S_4 index. Data are classified into six groups of S_4. Mean value (full circle) and standard deviation (vertical bar) are shown. Number of data points in each class is indicated at the top of the figure.

for stronger scintillations.

Consequently, our results suggest a tendency that stronger scintillations are produced by more elongated irregularities with both smaller minor radius and faster drift velocity. In the present study, the shape and size of the F-region irregularities have been made clear. In addition, two peculiar observation results have been brought out; namely, the scintillation saturation and the decrease in the correlation distance with increasing S_4, which suggests that the multiple scattering plays an important role in the production of the intense scintillation. Hence, these results will provide a clue to the investigation of the scintillation mechanism, especially of the radio scattering mechanism. Indeed, it has not been understood well in the intense scintillations until now. Further, by utilizing the observation results, a realistic irregularity model can be constructed. In order to solve these problems, numerical computations and additional considerations are necessary. These subjects will be given in Chapter 4.

3.3. RESULTS UNDER GEOMAGNETICALLY DISTURBED CONDITION

3.3.1. Scintillation observed on July 14, 1982

Observational results of the scintillations and the

related phenomena associated with a major geomagnetic storm on July 14, 1982 are described. This event has features somewhat different from those under geomagnetically quiet conditions (see 3.2). Figure 3.8 shows time variations of the geomagnetic H-component at Kakioka, total electron content (TEC) along the radio propagation path, drift velocity vector (apparent drift velocity), radio signal intensity, and S_4 index during 0 h to 11 h LT on July 14, 1982.

The scintillation intensity increased gradually from 0 h and reached a maximum near 5 h, and kept a relatively high level until about 0930 LT. Oscillations of long period (about 1 h) are seen in the received signal strength. They are not the fluctuations associated with the scintillations but those caused by the variation in antenna sensitivity for the rotating radiowave polarization. Strong scintillations which appeared just after 10 h are considered not to be a continuation of long-lasting scintillations but were produced by a sporadic-E layer. Scintillations produced by sporadic-E are often observed in summer daytime almost regardless of geomagnetic activity [Sinno and Kan, 1980]. As shown at the top of this Figure, the maximum excursion of the geomagnetic H-component was -630 nT. This storm was one of the most significant storms ever observed in Japan [Ogawa, 1986]. The scintillation happened during the decreasing phase of the geomagnetic H-component after the SSC (Storm Sudden Commencement) at 0117 LT.

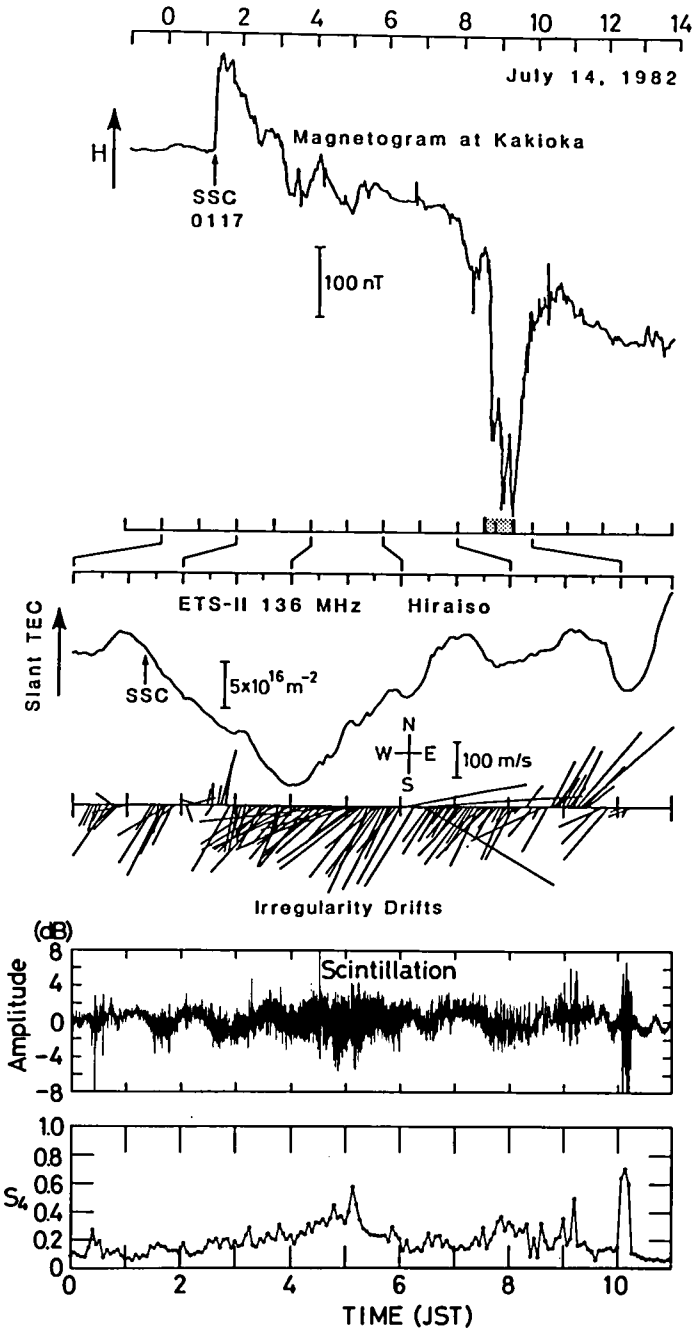

Fig. 3.8. Scintillation event on July 14, 1982. From top to bottom, time variations in geomagnetic H-component at Kakioka, total electron content (TEC) along the radio propagation path, irregularity drift (apparent velocity) represented by vector of which starting point is on the time axis, relative received power, and S_4 index are shown.

The morphology of VHF scintillations observed in Japan was investigated by Sinno and Kan [1980], who pointed out that usual nighttime scintillations start around 20 h in the evening and end around 5 h in the morning. However, the scintillations in Figure 3.8 started after midnight (0130 LT: S_4 reached 0.2) and lasted till about 0930 LT in the morning. In addition, the intensity was considerably weaker than the typical scintillations appearing in summer nighttime. The scintillation intensity attains a maximum of about 10 dB peak-to-peak (S_4=0.56) around 5 h. Even in geomagnetically quiet summer nighttime, scintillations over 20 dB peak-to-peak (or $S_4 \geq 1$) were frequently observed at 136 MHz around Japan. Another interesting feature in Figure 3.8 is that the scintillations lasted for long hours with an almost constant intensity. These are very different aspects when compared with the scintillations described in 3.2.

A steep depression of the H-component, which was one of the marked points of this geomagnetic storm, started at 0840 LT as shown in the top of Figure 3.8. During the depression, the scintillation amplitudes did not change clearly compared with those observed before and after the depression. After 0730 LT, however, the scintillation pitch, which is expressed by the number of crossings of an average level per unit time, became much slower than before. This indicates that the spatial scales of the irregularities became larger than before. By the way, in the event shown in Figure 3.8, no scintillations were observed at

4-GHz wave from CS (Medium Capacity Communications Satellite for Experimental Purposes, Sakura).

3.3.2. Movement of irregularities

For this scintillation event, full correlation analysis could not be made because the scintillations were not so strong (as compared with the results in the previous sections) that the computed correlation functions were not enough reliable. Therefore, only the apparent velocities obtained from the peak points of the cross-correlation functions are shown in Figure 3.8. Though the magnitude of the apparent velocity is always larger than that of the real drift velocity, the apparent velocity can give roughly the motion of the irregularities. It is noted that the difference between apparent and real drift velocities arises from the magnitude of characteristic random velocity V_c (see equation (2.20)).

As shown in Figure 3.8, the irregularity drifts were directed southwestward in most periods of the scintillations. Their velocities were between 100 and 200 m/s throughout the scintillations. During two periods of 0230-0250 LT and 0850-0930 LT, the drifts reversed and were directed northward or northeastward. During these periods, the geomagnetic H-component decreased steeply. The magnitude of drifts were 50-100 m/s in the first period and about 200 m/s in the second period.

Drift directions obtained during geomagnetically quiet nighttime were often along the southwest and northeast direction (see Figure 3.5), which is similar to the results in Figure 3.8. Abrupt reversals of drift directions were also observed in quiet night. However, the magnitudes of drifts in Figure 3.8 are much larger than those in quiet times. Note that the magnitudes of apparent velocities are slightly larger than those of real drift velocities in quiet times; they are typically between 50 and 100 m/s. Therefore, two possibilities are suggested from these results; the drift velocities and/or characteristic random velocities were much larger in the storm condition than in the quiet condition. In fact, it is reported that fast westward drifts were observed during geomagnetic storms by IS radar [Blanc, 1983]. Large characteristic random velocities mean a large variability of real drift velocities in time and/or in space.

One of the interesting features to be noted for this scintillation event is the reversal of drift corresponding to the abrupt decrease in the H-component. Especially, the decrease in the H-component near 9 h (LT) is supposed to have been caused by the auroral substorm-associated currents which extended toward Japan [Ogawa, 1986]. It is strongly inferred that the drift reversal is closely related with this peculiar current system.

3.3.3. Scintillation power spectra

Power spectrum of scintillation can give information of the structures of ionospheric irregularities. Figure 3.9 shows power spectra at 0500 (a) and 0852 LT (b) on July 14. They were obtained by the FFT (Fast Fourier Transform) analysis of the data for 256 s with a sampling period of 0.25 s. According to the weak scintillation theory, power spectra are usually composed of two parts: the higher frequency part showing a power-law type decrease with increasing frequency and the lower frequency part showing almost constant magnitude not depending on frequency [Rufenach, 1972]. In fact, both spectra in Figures 3.9a and b are composed of these two parts. However, the slopes at higher frequency parts are evidently different from each other; the slope in Figure 3.9a is very steep and is proportional to ν^{-7} (ν is the fluctuation frequency). Namely, the spectral index=7. On the other hand, the spectral index in Figure 3.9b is about 3. The spectral indices were 5-7 during the period of 4 h-6 h (LT) on July 14. They became 3-4 near the drift reversal which appeared around 9 h.

Spectral indices are about 3 for usual scintillations [Rufenach, 1972; Crane, 1977] and indices over 5 are rare. The spectral index reflects wavenumber spectrum of the irregularities (see section 1.3.2). When frequency spectrum is proportional to ν^{-p}, one-dimensional wavenumber spectrum should be proportional to $k^{-(p-1)}$ (k is the wavenumber) [Rufenach, 1972]. Therefore, the one-dimensional wavenumber spectra of the irregularities

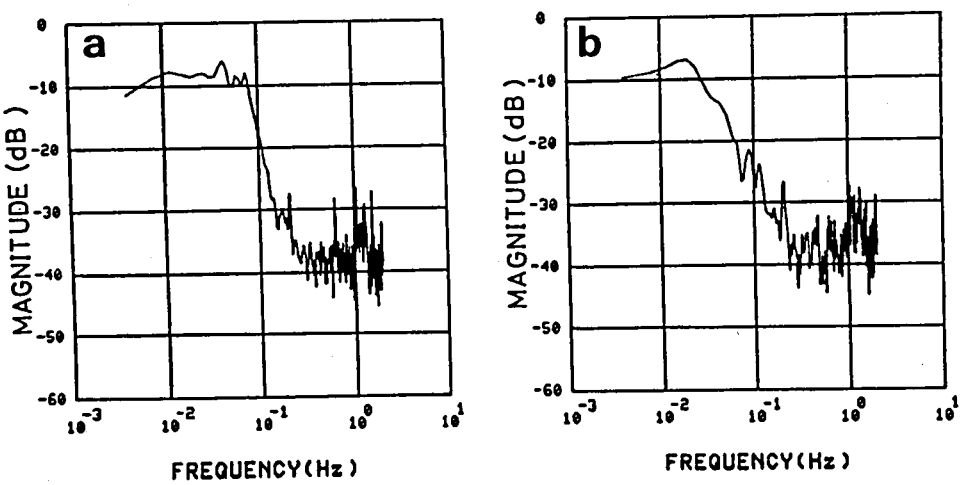

Fig. 3.9. Scintillation power spectra observed on July 14, 1982. (a) 0500 LT and (b) 0852 LT.

around 5 h (LT) on July 14 are considered to be proportional to k^{-6}. Namely, the irregularities had unusual structures which might be affected by some storm effects. For the scintillations around 9 h, these unusual structures seem to have been diminished in terms of the wavenumber spectrum of the irregularities.

3.3.4. Total electron content (TEC) and traveling ionospheric disturbances (TIDs)

Time variation in total electron content (TEC) is also shown in Figure 3.8. The TEC decreased until 4 h and then increased. During scintillations wave-like variations of TEC having periods from several to ten minutes are often observed [Sinno and Kan, 1978]. This kind of variation in TEC is also seen in this Figure. Systematic relations between the irregularity drifts and the TEC are not clear as compared with those in 3.3.

Wave-like variations in TEC from 4 h to 8 h, in spite of small amplitude, was also observed at Kokubunji and Yamagawa in the same 136-MHz Faraday rotation observations. The TEC variations obtained at the three stations are shown in Figure 3.10. The locations of the stations were shown in Figure 2.8. The distance between Hiraiso and Kokubunji (120 km) is much smaller than that between Hiraiso and Yamagawa (1020 km). That is the reason why the correlation between Hiraiso and Kokubunji

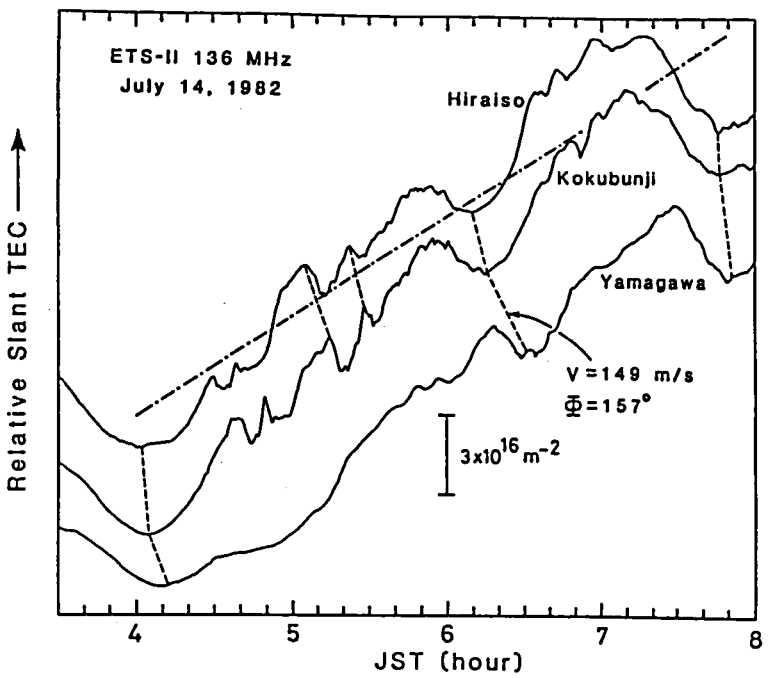

Fig. 3.10. Time variations in TECs obtained at Hiraiso, Kokubunji, and Yamagawa on July 14, 1982. The ordinate represents relative TEC along the radio path. In order to make clear time lags among them, corresponding points on wave forms are connected by broken lines. Propagation speed and direction of TEC variations are also shown. As for a chain line, see the caption of Fig. 3.11.

is good, while that between Hiraiso and Yamagawa is worse. By comparing the TEC wave forms, it seems clear that the TEC variations were propagated roughly southward as a TID (Traveling Ionospheric Disturbance). It may be somewhat difficult to obtain the accurate speed and direction of the TID because Yamagawa is far from two other stations and because the correlations between Yamagawa and other stations are worse. By the correspondences (broken lines in Figure 3.10) among three wave forms, the propagation speed and its direction are estimated to be 149 m/s and 157° (from north to east), respectively. Namely, the TID was propagated from the northwest to the southeast.

Figure 3.11 shows the power spectrum of the TEC time variations obtained at Hiraiso during 0400-0815 LT. This was calculated by FFT after subtracting the general trend shown in Figure 3.10 by a chain line. Although prominent frequency components cannot be seen, the components of periods of 51, 28, 13 min are discernible. Taking account of the above-derived propagation velocity of the TID, the wavelengths of these components are between 100 and 500 km. This kind of TID is considered to belong to the so-called medium-scale TID.

3.4. CONCLUSION

Using three spaced-antennas, the mid-latitude nighttime

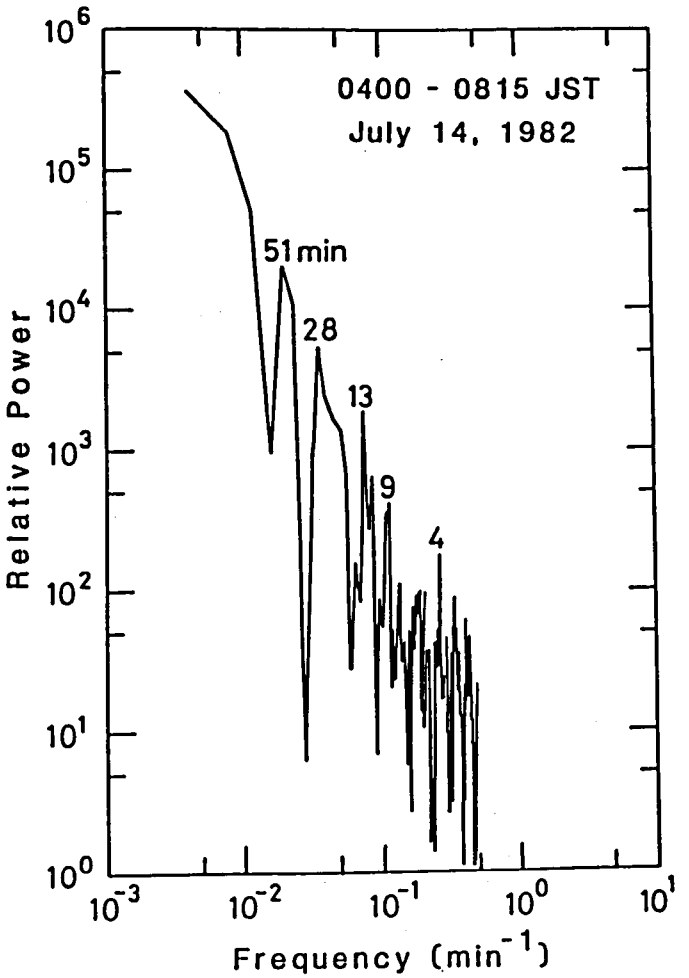

Fig. 3.11. Power spectrum of TEC variation from 0400 to 0815 LT on July 14, 1982 at Hiraiso. This was obtained after removing a general trend shown by chain line in Fig. 3.10.

scintillations at 136 MHz were observed during June-July, 1982. By means of correlation analysis, characteristics of ionospheric irregularities, such as drift velocities, sizes and shapes of the irregularities were investigated. First, analysis was made for seven scintillation events under geomagnetically quiet conditions. Since the irregularities were mostly elongated significantly along the geomagnetic field lines, only drift components perpendicular to the elongation were obtained.

Results are summarized as follows: (1) Most drift directions were southward or southwestward. In the postmidnight hours, the northward drifts sometimes appeared. Although high northward drifts exceeding 80 m/s were occasionally observed, mean northward and southward drift velocities were almost equally 25 m/s and 23 m/s, respectively. (2) Reversal of the drift direction from southward to northward or northward to southward occurred occasionally. Peculiar and abrupt drift reversals from northward to southward were observed in the midst of strong and high-pitch scintillations. They were accompanied by a sharp increase in TEC, which may be due to the downward motion of the irregularity height. (3) The shape and size of the irregularity pattern (ellipse) projected onto the plane perpendicular to the radio path were examined. The directions of major axes of the ellipses were coincident with those of the geomagnetic field lines at F-region height, which suggests that the irregularities are well field-aligned. From time variation of the direction of

the major axis, decrease in irregularity height with time is suggested. (4) The axial ratio of the irregularities increased and the minor radius of them decreased with increasing S_4. The latter result suggests that the multiple scattering plays an important role in the production of the intense scintillations.

Second, observational results of a scintillation event which occurred on July 14, 1982 during severe geomagnetic storm were described. These results have the following features which are somewhat different from those observed under geomagnetically quiet conditions: (1) The occurrence hour was too late; they started after midnight and lasted until 0930 LT. (2) The irregularity drifts (the apparent velocities) were very high (100-200 m/s). (3) When the geomagnetic H-component was steeply decreasing, the drift direction reversed from southwestward to north or northeastward. (4) The spectral indices of the scintillation spectra were larger ($\sim$7) than usual, which means that the slopes of wavenumber spectra of the irregularities were also steep. (5) TID-like fluctuations propagated southeastward were observed on the time variation in TEC. Consequently, these results suggest that the scintillations in this event were produced by the ionospheric irregularities which were considerably controlled and modified by the geomagnetic storm effect. Further investigations are necessary to clarify the causal relationship among above five items.

CHAPTER 4

ANALYSIS OF RADIOWAVE SCATTERING FOR INTENSE SCINTILLATIONS BY FOURTH-MOMENT EQUATION METHOD

4.1. INTRODUCTION

In recent years, much attention has been paid to the intense scintillation phenomena appearing on transionospheric radio waves. It is considered that the multiple-scattering mechanism may play an important role in these ionospheric scintillations [Vats, 1981]. In fact, amplitude scintillations have been observed in the GHz band of satellite radio waves often in the equatorial latitude in association with plasma bubbles [Basu and Basu, 1981; Basu et al., 1983], and sometimes in midlatitudes [Ogawa et al., 1980]. In both cases, it is observed that very intense scintillations, which may reach saturation levels, appear also in the VHF band.

In order to study the intense scintillations and their generation mechanism, several analyses have been made in respect to the frequency dependence of scintillation intensity and the scintillation power spectra [Umeki et al.,1977a; Vats, 1981; Basu et al., 1983; Franke and Liu, 1983]. Auto-correlation time (i.e., coherence time) is known to decrease for intense

scintillations [Umeki et al., 1977b; Vats, 1981; Basu et al., 1983; Franke and Liu, 1983]. Franke and Liu [1985] pointed out that the decrease in coherence time can be a good indicator of the perturbation strength in intense scintillations even when the S_4 index reaches its saturation value of unity.

Solving the fourth-moment equation (parabolic equation) is one of the powerful theoretical approaches to treat the intense scintillation problem involving multiple-scattering effects [Tatarskii, 1969; Brown, 1972a; Liu et al., 1974; Yeh et al., 1975; Booker et al., 1985; Gozani, 1985]. Liu et al. [1974] showed a numerical scheme to solve this equation for a two-dimensional transionospheric propagation model. Using this scheme, the decorrelation effects in space and frequency domains were investigated for a power-law spectrum of ionospheric irregularities [Yeh et al., 1975; Liu and Yeh, 1975; Yeh and Liu, 1982]. Vats [1981] showed a good consistency between the multi-frequency scintillation observations and the results obtained by this theory, with respect to both the frequency dependence of S_4 index and the coherence time.

Measurement of a spatial correlation function can provide another, and more direct, way to compare measurement results with theoretical ones and to investigate the scattering process. The three spaced-receiver measurements of ionospheric scintillations described in the previous chapter can contribute to this kind of study.

Two peculiar results which have been found in Chapter 3, i.e., the scintillation saturation and the decrease in the correlation distance with increasing S_4, suggest that the multiple-scattering plays an important role in the production of intense scintillations. In this chapter, in order to interpret the observational results in terms of multiple-scattering, numerical computations are made by applying the fourth-moment equation method [Kumagai, 1987]. First, the method of computation and the numerical model are outlined. Second, results of numerical computations are shown. Third, comparisons between the observational and computational results are presented, and then a model of the ionospheric density irregularities is considered together with the frequency dependence of the scintillations.

4.2. COMPUTATION OF FOURTH-MOMENT EQUATION

4.2.1. Computational model

A vertical-incidence ionospheric model shown in Figure 4.1 is used in the numerical computation. A plane wave is assumed to be incident on the top of the irregularity slab (z=0), which is statistically homogeneous and confined between z=0 and z=L. In addition, the irregularities are assumed to be anisotropic; the anisotropy axis is parallel to the incident radio path. The

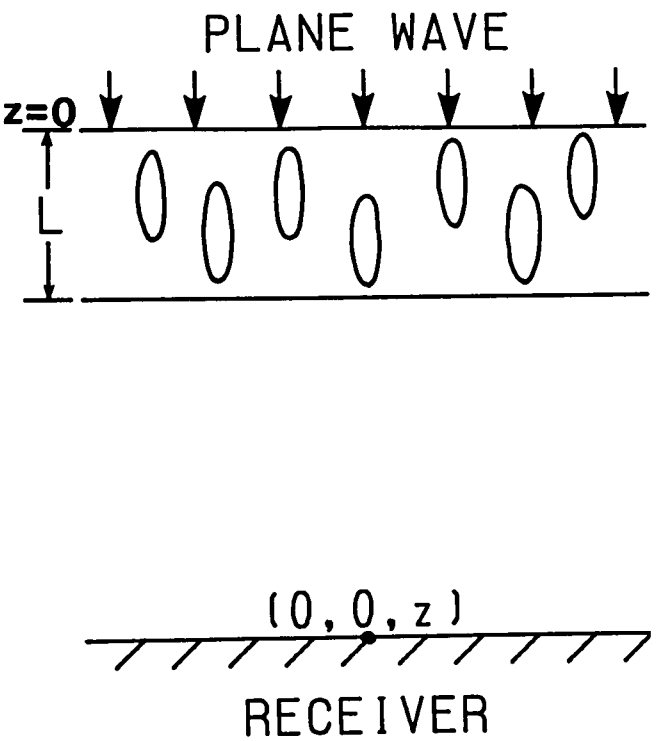

Fig. 4.1. Geometry of ionospheric scintillation model. A plane wave is vertically incident on the top of the irregularity slab, which is confined $0 \leq z \leq L$. Anisotropic irregularities are also considered, their anisotropic axis is parallel to the radio path.

irregularity slab is characterized by the dielectric permittivity

$$\varepsilon = <\varepsilon> [1 + \varepsilon_1(r)] \tag{4.1}$$

were < > denotes an ensemble average and $\varepsilon_1(r)$ is a random function of position. After the wave emerges from the irregularity slab, it propagates in free space until it arrives at the receiver on the ground.

The assumption of vertical incidence may be inconsistent with the observation geometry for which the incidence angle to the irregularity slab is about 45° (see Figure 2.9). However, it has been shown that the dependence of the incidence angle on the scattering characteristics becomes weak when the slab thickness is much larger than the correlation distance normal to the slab [Rino and Fremouw, 1977]. This is the case for the ionospheric irregularities concerned here. The angle between the radio path and the anisotropy axis (direction of elongation) seems to be a more important factor to control the diffraction effects [Briggs and Parkin, 1963]. In fact, the assumption that the radio path is parallel to the anisotropy axis is rather approximate to the actual value of 15°. Therefore, to a first approximation, the model geometry in Figure 4.1 will give meaningful results to interpret the observational results shown in 3.2. It is remarked here that the path length in the computation will represent the slant path length in the actual observation geometry.

It has been found from ground-based scintillation

observations [Rufenach, 1972] and in-situ measurements [Dyson et al., 1974] that the ionospheric density irregularities have power-law spectra for which the three-dimensional spectral index is nearly 4, i.e.,

$$\Phi(k) \propto k^{-4} \tag{4.2}$$

where, Φ and k are the three-dimensional spectrum and wavenumber, respectively. In our observation described above, the frequency spectra for relatively weak scintillations ($S_4 \leq 0.4$) also showed power-law type, for which the mean value of spectral index q was 3.1 (q=p-1) with the standard deviation of 0.8.

For a spectral index of 4, the correlation function $B(\rho, z)$ is given by [Yeh and Liu, 1982]

$$B(\rho, z) = \frac{\langle (\Delta n / n_0)^2 \rangle}{\sqrt{k_0 r_i}\, K_{1/2}(k_0 r_i)} \left(k_0 \sqrt{\rho^2 + z^2/\gamma^2 + r_i^2}\right)^{1/2} \cdot K_{1/2}\left(k_0 \sqrt{\rho^2 + z^2/\gamma^2 + r_i^2}\right) \tag{4.3}$$

where ρ is the transverse coordinate, r_i the inner scale, k_o ($=2\pi/r_o$) the wavenumber corresponding to the outer scale r_o, and $k_o r_i \ll 1$ is always implied. $K_{1/2}$ and $\langle (\Delta n/n_o)^2 \rangle$ denote the modified Bessel function of 1/2 th order and the mean square value of electron density fluctuation, respectively. γ is the anisotropic factor representing that the scale length in the z direction is γ times as large as that in the transverse

direction. Recently, the two-component power-law spectrum model (in which the spectral index is not unique for all wavenumbers) is considered to be a plausible model of the ionospheric irregularities [Franke and Liu, 1983, 1985]. The present computation can be easily applicable to this model.

4.2.2. Fourth-moment equation

We first give the basic assumptions which are usually used in the wave propagation in random media [Liu et al., 1974; Yeh and Liu, 1982]:

(i) $\langle \varepsilon_1^2 \rangle k\ell \ll 1$, (ii) $\langle \varepsilon_1^2 \rangle kz \ll 1 \ll k\ell$, (iii) $z \gg \ell$

where $\langle \varepsilon_1^2 \rangle$ is the mean square value of fluctuating part of the dielectric permittivity, and k, ℓ, and z are the wave number, the characteristic length of the random medium, and the distance that the wave has traveled in the random medium, respectively. Even if the anisotropy is introduced, these relations are assumed to be still satisfied.

The fourth moment of the field is expressed as

$$\Gamma_4(\alpha, \beta, z) = \langle u(\rho_1, z)\, u^*(\rho_2, z)\, u(\rho_3, z)\, u^*(\rho_4, z) \rangle \qquad (4.4)$$

where ρ_i is the transverse coordinate, $\alpha = \rho_1 - \rho_2$, $\beta = \rho_2 - \rho_3$,* and u is the random complex amplitude of the wave propagating in the z direction. The asterisk denotes complex conjugate. The

*Contribution of ρ_4 to Γ_4 can be ignored [Brown, 1972b].

partial differential equation that governs the propagation of the fourth moment of a plane wave in a two-dimensional, random and homogeneous medium is [Brown, 1972a; Brown, 1972b; Liu et al., 1974; Yeh and Liu, 1982]

$$\left\{ \frac{\partial}{\partial \zeta} + j \frac{\partial^2}{\partial \xi \partial \eta} - g(\xi, \eta) \right\} \Gamma_4(\alpha, \beta, z) = 0 \tag{4.5}$$

where the coordinates are normalized to non-dimensional values

$$\xi = \alpha / r_0, \quad \eta = \beta / r_0, \quad \zeta = z / k r_0^2 \tag{4.6}$$

and

$$g(\xi, \eta) = -2\sigma(0) + 2\sigma(\xi) + 2\sigma(\eta) - \sigma(\xi+\eta) - \sigma(|\xi-\eta|) \tag{4.7}$$

$$\sigma(\xi) = \tfrac{1}{4} k^3 r_0^2 (f_p^4 / f^4) \langle (\Delta n / n_0)^2 \rangle d(\xi) \tag{4.8}$$

Where f and f_p are radio frequency and plasma frequency, respectively. $d(\xi)$ is an integrated correlation function over z, which is given by

$$d(\xi) = \frac{1}{\langle (\Delta n / n_0)^2 \rangle} \int_{-\infty}^{\infty} B(\xi, z)\, dz = 2\gamma r_0 \sqrt{\xi^2 + (r_i / r_0)^2}\, K_1\left(2\pi \sqrt{\xi^2 + (r_i / r_0)^2}\right) \tag{4.9}$$

where K_1 is the modified Bessel function of the first order.

The numerical method used here is an implicit difference scheme, which was outlined by Liu et al., [1974] (see Appendix B). The initial condition is

$$\Gamma_4(\xi, \eta, 0) = 1 \tag{4.10}$$

and the boundary conditions at $\xi \to \infty$ or $\eta \to \infty$ are

$$\begin{aligned} \Gamma_4(\xi \to \infty, \eta, \zeta) &= \exp\{g(\xi \to \infty, \eta)\zeta\} \\ \Gamma_4(\xi, \eta \to \infty, \zeta) &= \exp\{g(\xi, \eta \to \infty)\zeta\} \end{aligned} \tag{4.11}$$

Once Γ_4 is known, one can compute the scintillation index S_4 and the transverse correlation function C_I immediately from (Appendix C)

$$S_4^2 = \Gamma_4(0, 0, \zeta) - 1 \tag{4.12}$$

$$C_I = \{\Gamma_4(0, \eta, \zeta) - 1\} / S_4^2 \tag{4.13}$$

The transverse correlation distance d_c is defined as the length from the origin to a point at which C_I falls to 0.5. S_4 and d_c are directly compared with those obtained by the observation.

4.2.3. Parameters for computation

In the computation, (ξ, η) space is divided into two-

dimensional meshes. The full area to be treated in the computation should be large enough as compared with the fluctuation scale because the boundary conditions are applied at $\xi, \eta = \infty$. On the other hand, the mesh size must be small enough to maintain accuracy of the difference computation. By making a compromise between these requirements and the computer resources available, the computation area and mesh size were selected to be 2.4 r_o and 0.025 r_o, both being equal in ξ and η directions. Hence, the number of mesh elements is 191 x 191.

The Fresnel scale is one of the characteristic scale sizes which rule field fluctuations taking place. The size of the first Fresnel zone is given by $d_F = \sqrt{\lambda(z - L/2)}$, where λ is the wave length and L is the thickness of irregularity slab [Yeh and Liu, 1982]. The Fresnel-zone size increases with the propagation distance. By setting the wave frequency of 136 MHz and the propagation distance of 600 km (F-region irregularities), the first Fresnel-zone size is about 1100 m. In order to handle the fluctuation of this size, r_o should be much larger than d_F [Booker et al., 1985]. In view of the foregoing, r_o is taken to be 3000 m. It is ascertained beforehand that for this value of r_o the fluctuations with the Fresnel scale can be taken up properly up to the propagation distance of, at least, 600 km. The validity test of r_o will be shown later. In the present computation, the inner scale r_i was not introduced [Yeh et al., 1975]. In this case, the practical inner scale is considered to be the same as

the mesh size, i.e. $r_i = 0.025\ r_o$ [Booker et al., 1985].

The computations are made for two cases: thin and thick irregularity slabs, both for various values of density fluctuation amplitude. We express the propagation path length by h (= z - L/2) uniformly in both cases. A parameter C is introduced to represent the density fluctuation

$$C = \frac{1}{4} k^3 r_o^3 \left(f_p^4 / f^4 \right) < (\Delta n / n_0)^2 > \tag{4.14}$$

The numerical parameters are tabulated in Table 4.1, in which both normalized and actual values are shown. h_o represents the path length at which the computational results are compared with the observational ones. A glance at (4.9) makes clear that the anisotropy factor γ acts as if the density fluctuation C increases γ times that in the case of $\gamma = 1$, with no any other changes. Therefore, the computation is carried out only in the isotropic case ($\gamma = 1$) and then the effect of anisotropy is evaluated by combining the results of different density fluctuations. The accuracy of the computation is examined by the conservation law [Tatarskii, 1971]

$$\frac{\partial}{\partial \zeta} \int_{-\infty}^{\infty} \{ \Gamma_4 (0, \eta, \zeta) - 1 \} \, d\eta = 0 \tag{4.15}$$

In the worst case, the error throughout the computation amounted to 10^{-2} at most.

Table 4.1. Parameters for computation. Both normalized and actual values are listed.

Parameter		Normalized	Actual
Wave frequency	f		136 MHz
Plasma frequency	f_P		7 MHz
Outer scale	r_o		3000 m
Mesh size	$\Delta\xi = \Delta\eta$	0.025	75 m
Boundary	$\xi_{max} = \eta_{max}$	± 2.375	± 7125 m
Integration step	$\Delta\zeta$	0.0001	2.56 km
Path length	h_o	0.0175	450 km
Slab thickness	L (thin)	0.001	25.6 km
	(thick)	0.01	256 km

4.3. COMPUTATIONAL RESULTS

4.3.1. Thin irregularity model

First, computational results for the thin and isotropic irregularity slab model are shown. Figure 4.2 depicts the evolution of the scintillation index S_4, which increases with the path length. Several values of density fluctuation are assumed through the range from C=100 to 30000, which correspond to the fluctuation level from 1% to 17 % in terms of $<(\Delta n/n_o)^2>^{1/2}$. The origin of h is the center of the slab. The abscissa shows the actual value of path length in km. The left side (h = -12.8 km) corresponds to the incident point into the slab; the thickness of the irregularity slab is 25.6 km (dotted range). As is well known, S_4 soon reaches a saturation level ($S_4 \sim 1$) for high density fluctuations. In the case of the highest fluctuation, an oscillation appears at the early stage of the saturation. In the case of lower fluctuations, after a relatively rapid increase, S_4 still keeps slow increase until the end of computation. Attainable S_4 value at a path length depends on the density fluctuation level.

The transverse correlation function C_I is shown in Figure 4.3 in the case of C=100, the weakest density fluctuation case in Figure 4.2. The correlation functions seen at four different path lengths, i.e., at h= 90, 295, 500, 705 km are shown. The abscissa

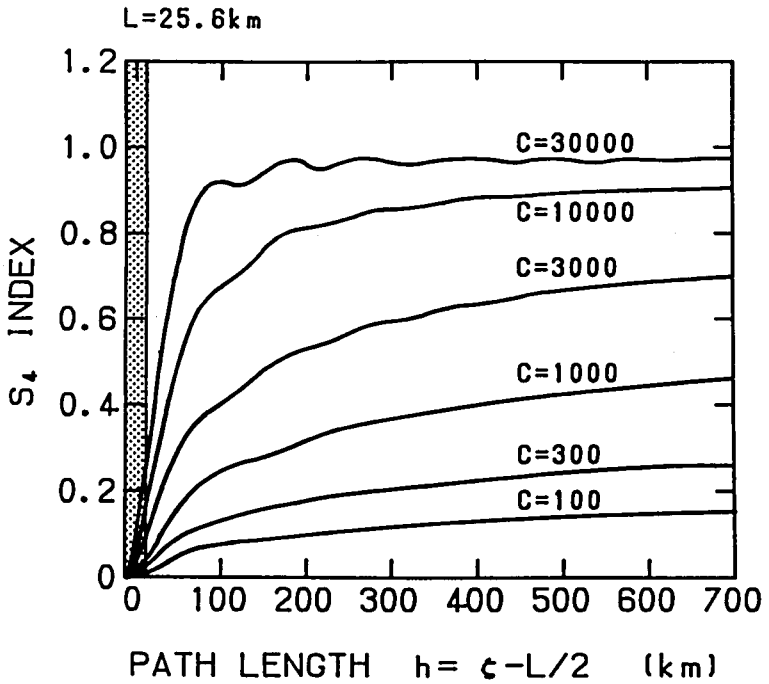

Fig. 4.2. Evolution of S_4 index with path length in the thin slab model; slab range is dotted (L=25.6 km). Results for six C values are shown.

shows the actual transverse distance in m. The outer scale r_o is 3000 m. With increasing path length, the width of C_I becomes larger and C_I oscillates resulting in the appearance of the second peak. The transverse correlation distance d_c, i.e., the distance at which C_I falls to 0.5, proves to increase almost in proportion to $\sqrt{h}$. d_c is 240 m at h=500 km. Since the Fresnel-zone size is proportional to $\sqrt{h}$, it is considered that the fluctuation of the field with the Fresnel scale is stimulated. In fact, d_c is about one fourth of the first Fresnel-zone size. This result is consistent with the theoretical results obtained by Crane [1977] although he computed the distance for logarithmic fluctuation amplitude.

The variation in d_c with increasing path length is shown in Figure 4.4. Each curve corresponds to the different outer scale r_o. These were all computed under the condition of the thin and weak irregularities. The S_4 indices are less than 0.17 at the end points of all curves. Since these curves remain in the weak scintillation range (i.e., the decorrelation effect seems not effective), d_c would increase with the path length in accordance with the Fresnel distance ($\propto\sqrt{h}$) and should change along a straight line in this Figure. The deviation from the straight line is considered to result from the insufficiency of r_o against the Fresnel distance. Hence, this Figure may be used for a validity test of r_o. In the case of r_o=4000 m, d_c lies almost on a straight line throughout the range of h. r_o of 3000 m is also

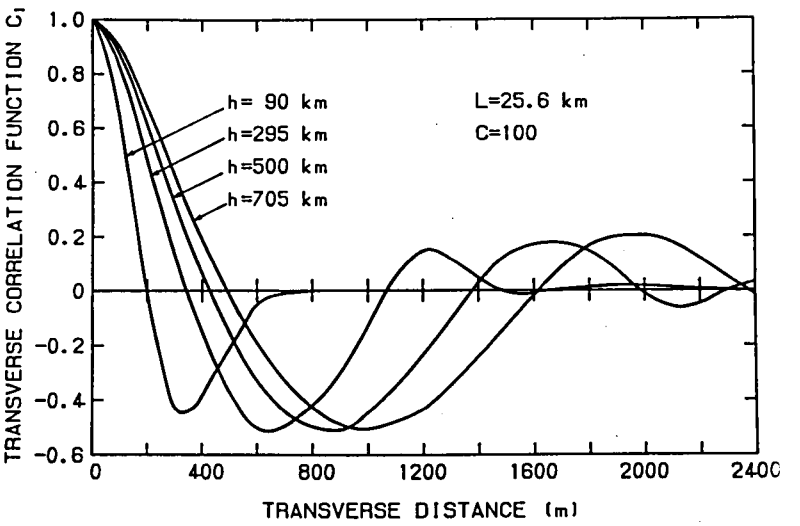

Fig. 4.3. Transverse correlation function C_I for the thin and weak irregularity slab. Abscissa is transverse distance in m. C_I at four path lengths is shown.

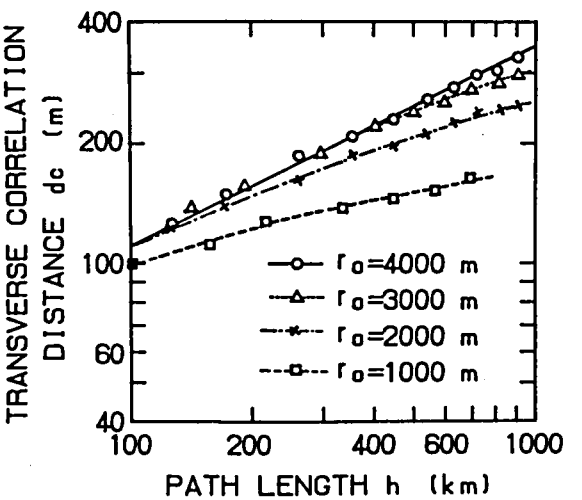

Fig. 4.4. Variation in transverse correlation distance d_c with path length under the condition of thin and weak irregularities. Each curve corresponds to different outer scale r_o from 1000 to 4000 m.

valid for h≤500 km; deviation from the straight line is less than 2% until this point. Values of r_o less than 3000 m seems inadequate in our computations. Therefore, r_o of 3000 m is used in the whole computation. However, this validity test is essentially effective in the weak scintillation range. Since the irregularities with scale sizes larger than the Fresnel scale may contribute to intense scintillations [Booker and MajidiAhi, 1981], it may be necessary to examine further the effect of r_o in the intense scintillations.

C_I in intense scintillation is shown in Figure 4.5. The density fluctuation C is 100 times as large as that in Figure 4.3, C=10000, corresponding to $<(\Delta n/n_o)^2>^{1/2}$=9.5 %. C_I is shown for the same four path lengths as in Figure 4.3. The evolution of S_4 with increasing path length has been already shown in Figure 4.2, in which S_4 reaches 0.9 and is almost in saturation level at the path length of 500 km. d_c in Figure 4.5 decreases obviously compared with that in Figure 4.3; d_c=140 m at 500 km. In addition, the curves except one at the smallest path length are significantly smoothed out and are nearly flat after the first minimum points. These behaviors are considered to be caused by the decorrelation effects associated with the strong scattering.

Variation in C_I at 500 km path length is shown in Figure 4.6 for various values of C. The S_4 index for each case is also indicated in the Figure. It is clearly shown that the transverse correlation distance d_c decreases with increasing S_4 (or C). In

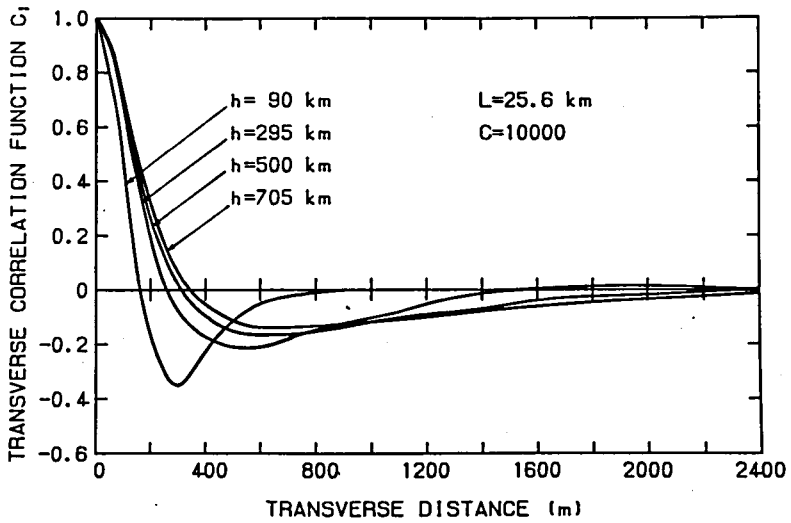

Fig. 4.5. Transverse correlation function C_I for thin and dense irregularity slab. Other explanations are the same as those in Fig. 4.3.

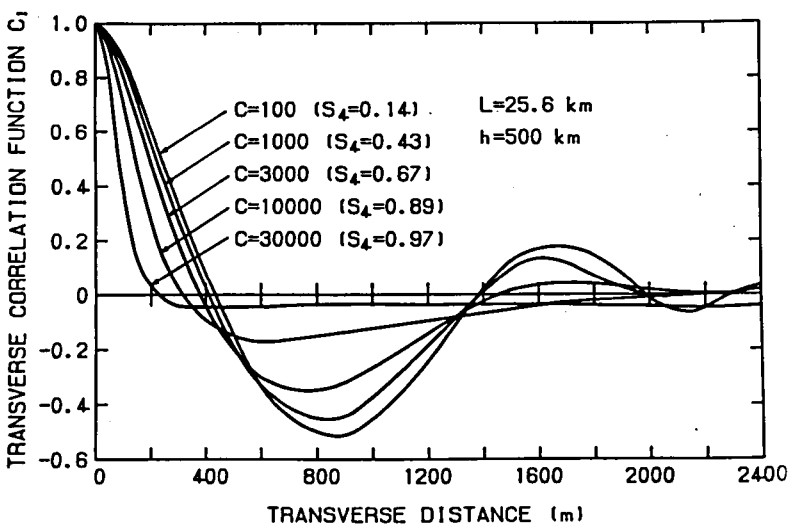

Fig. 4.6. Variation in transverse correlation function C_I with density fluctuation C at path length of 500 km for thin irregularity slab.

the case of the highest density fluctuation level, d_c becomes 80 m which is one third of that for the weak scintillation. These results suggest that the decrease in the minor radius observed in Figure 3.7b is successfully interpreted by the present computations and moreover that actual ionospheric irregularity model can be constructed.

4.3.2. Thick and anisotropic irregularity model

Next computation is made for the thick irregularity model. The evolution of the S_4 index with path length is shown in Figure 4.7 using the same format as Figure 4.2. The irregularities are still assumed to be isotropic, and the slab thickness (L=256 km) is 10 times as large as that for the thin model. Six curves are drawn, for each of which the density fluctuation C is 0.1 times the corresponding one in Figure 4.2. The behavior of each S_4 curve is almost identical to that shown in Figure 4.2, except at the early stage of the computation.

This similarity between thin and thick irregularity slabs is explained as follows. Scattering characteristics are governed by the mean square value of total phase fluctuation $<\Delta\phi^2>$ which the radiowave experiences during the slab. $<\Delta\phi^2>$ obeys [Yeh et al., 1975; Booker et al., 1985]

$$<\Delta\phi^2> \propto L\,C \qquad (4.16)$$

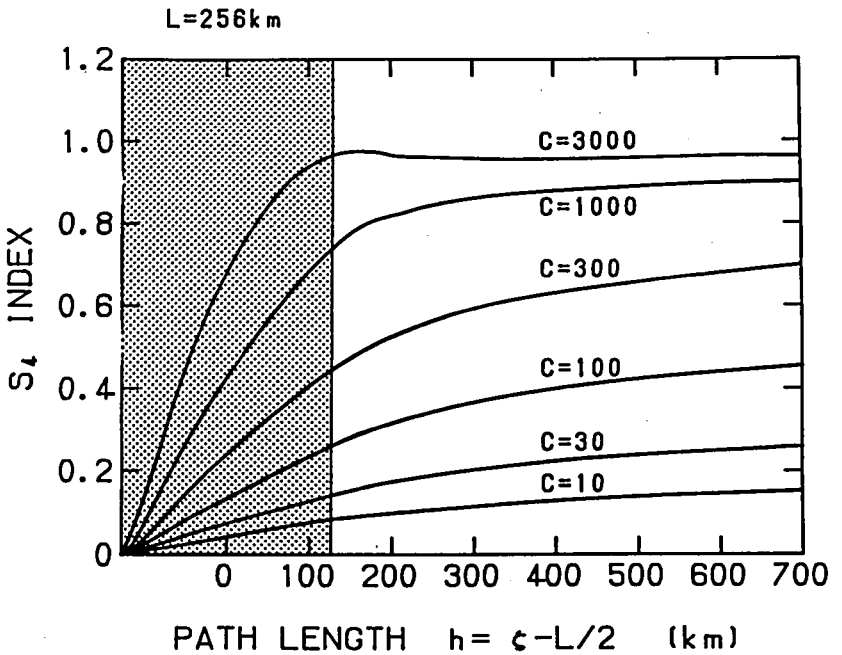

Fig. 4.7. Evolution of S_4 index with path length for the thick slab model; slab range is dotted (L=256 km). Results for six C values are shown.

Therefore, the identical results are obtained for the same $<\Delta\phi^2>$ even if C and L are different from each other. However, at the early stage the evolution of the S_4 index in the thick case is different from that in the thin case; the oscillations seen in Figure 4.2 do not appear in Figure 4.7, and moreover a focusing-like phenomenon, although faint, appears in the case of the highest density fluctuation in Figure 4.7.

The transverse correlation function C_I is shown in Figure 4.8 in the case of the weakest fluctuation (C=10). C_I is shown at four path lengths, three of which are nearly the same as those in Figure 4.3. Variations in C_I and d_c seen in Figure 4.8 are somewhat similar those for the thin one (C=100; Figure 4.3) at the same path lengths. This result also supports the view that $<\Delta\phi^2>$ is an ultimate parameter describing the scattering property. In addition, it is certified that the expression for the Fresnel zone, $d_F=\sqrt{\lambda(z-L/2)}$, is valid in the case where the irregularity slab is rather thick. Therefore, it is possible to treat the path length uniquely by h=z-L/2 regardless of the slab thickness. Thus, the behavior of C_I in the case of thick and intense scintillation is estimated from the results obtained from thin slab case by considering the factors representing slab thickness (L) and density fluctuation level (C).

As was mentioned in 4.2.3, the effects resulting from anisotropic irregularities are evaluated as follows: the effective value of C in the anisotropic case is considered to be

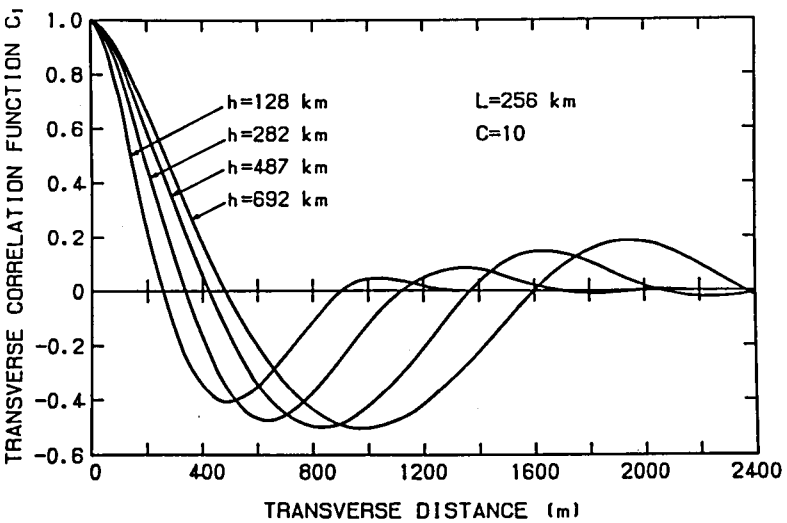

Fig. 4.8. Transverse correlation function C_I for thick and weak irregularity slab. Other explanations are the same as those in Fig. 4.3.

γC. Similarly, the effective density fluctuation and the total phase fluctuation are $\sqrt{\gamma}<(\Delta n/n_o)^2>^{1/2}$ and $\gamma<\Delta\phi^2>$, respectively. These effects will be considered in the next section in relation to the actual irregularity model.

4.4. DISCUSSION

4.4.1. Comparison with observation results

From the computations described above, it is confirmed that the S_4 index at a particular path length is almost uniquely determined by $<\Delta\phi^2>$ and that the correlation distance at a certain path length has a one-to-one correspondence to the S_4 index. Figure 4.9 shows the relation between the S_4 index and the transverse correlation distance d_c. Comparison is made between the computational and observational results. The observed mean values of the minor radius of the irregularities (50% decorrelation distance; Figure 3.7b) are shown in Figure 4.9 together with the numerical results of d_c at 450 km path length. It is seen from the numerical results that d_c depends weakly on S_4 in the weak scintillation range ($S_4 \leq 0.4$), while it steeply decreases with increasing S_4 in the intense scintillation range. Since d_c varies with the Fresnel-zone size, the d_c curve shifts upward or downward with the path length especially in the weak

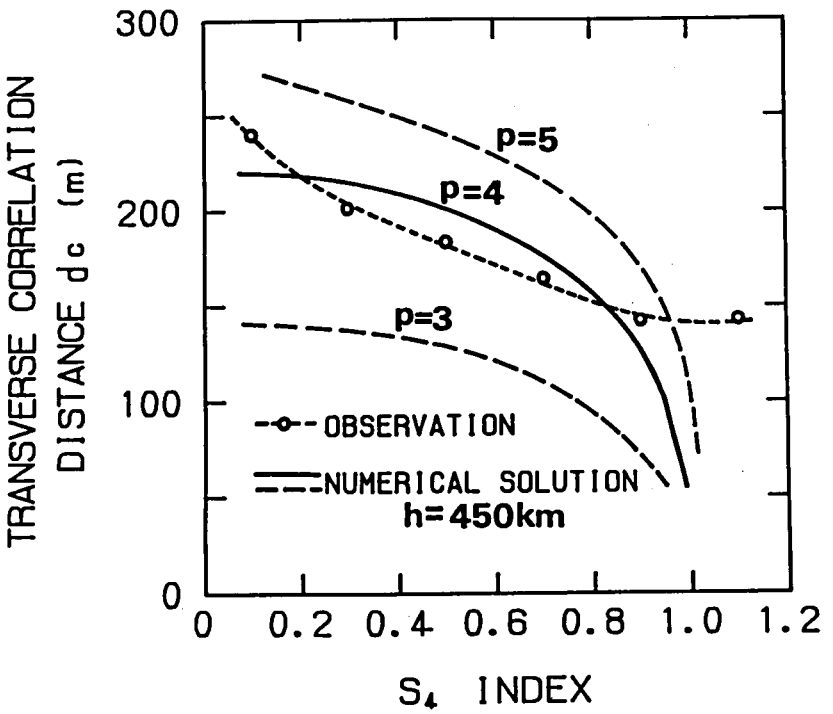

Fig. 4.9. Transverse correlation distance d_c as a function of S_4 index. Both observed and numerical results are shown. Three curves of numerical results are drawn; they are for power-law spectrum indices of irregularities, p=3, 4 and 5 at 450 km path length.

scintillation range. The variation in d_c at 450 km path length is fairly consistent with that from the observation, especially in the middle range of S_4. Therefore, it is found that the observed decrease in correlation distance with increasing S_4 can be explained by the decorrelation effect associated with multiple scattering. Moreover, it is estimated that the distance between the receiver and the slab center is about 450 km, i.e., the irregularity height of 320 km.

However, the curvature of the observed d_c is not consistent with that from the computation. Especially, the observed d_c does not decrease but remains almost constant in the range of $S_4 \sim 1$. This discrepancy may stem from the characteristics of intense scintillations themselves because they are so variable in time that they scarcely continues steadily during a data segment for processing (3.2 min). Therefore, actual value of d_c may have not been detected; the observed value may become larger than the actual one. Also in the range of very weak scintillation, the numerical and observed values are rather different from each other. The reliability of the observed value is low in this range because there are much data for which the cross-correlation coefficients between two antenna signals are not high enough for the correlation analysis.

Another possible explanation for this discrepancy is as follows. Numerical results for three power-law indices of the irregularity spectrum are also shown in Figure 4.9. The d_c curve

considerably shifts upward for the spectral index p=5 and downward for p=3. This variability in d_c with p is roughly explained in terms of the correlation distance of irregularity model; the expression of the correlation function for p=4 was given in (4.3). It is noted that the discrepancy between the observed and numerical results may be resolved if the spectral index varies around the value of p=4 during the scintillations, namely, p becomes a little larger than 4 in two S_4 ranges: $S_4<0.2$ and $S_4>0.8$. However, this discussion is not based on the observation results. Recently, a two-component power-law spectrum model for the ionospheric irregularities was proposed and considered to be valid to explain the scintillations over a wide intensity range [Franke and Liu, 1983, 1985]. It seems necessary to examine this model in the computations in future. Another explanation is that the model of the present computations might not be realistic enough. It may be necessary to compute with an oblique incidence model.

4.4.2. Electron density fluctuation model

Electron-density fluctuation necessary to produce the scintillations varies depending on the slab thickness and irregularity anisotropy factor. Three curves representing the relation between the density fluctuation $<(\Delta n/n_o)^2>^{1/2}$ and the S_4 index at a path length of 450 km are shown in Figure 4.10.

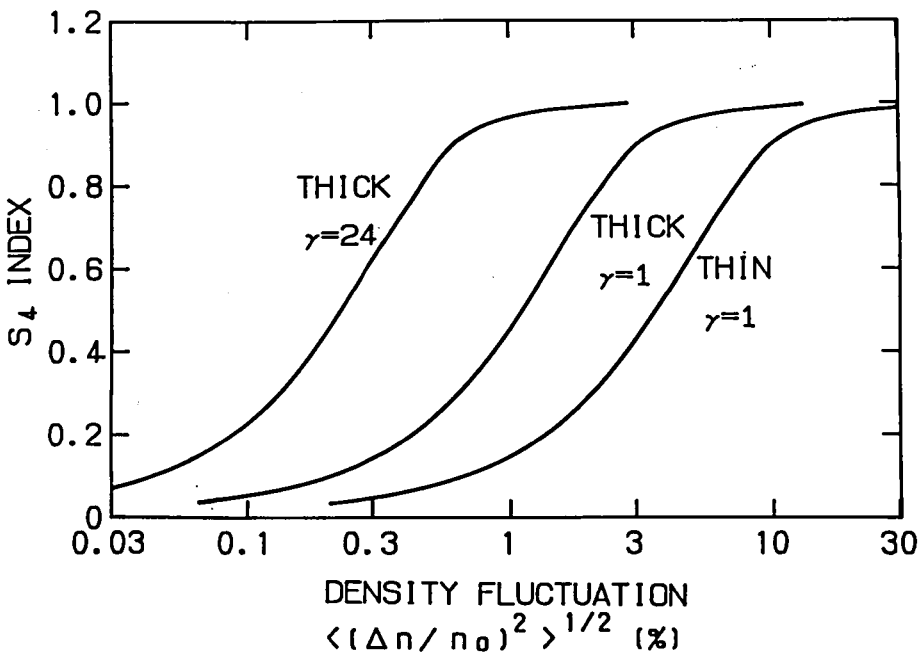

Fig. 4.10. Electron density fluctuation necessary to produce the scintillation of some S_4 index. Three cases are shown; thin and isotropic, thick and isotropic, and thick and anisotropic γ =24.

They are thin and isotropic, thick and isotropic, and thick and anisotropic cases. The spectral index of the irregularities p is 4 for these three models. The anisotropy factor, i.e. the axial ratio, is assumed to be 24, which is the mean value observed (see 3.2). A density fluctuation over 10 % is necessary for the scintillation to reach the saturation level in the thin and isotropic case. In the thick and anisotropic case, the magnitude of density fluctuation necessary for saturation decreases over one order relative to that in the former case. The observed axial ratio was not constant but increased with increasing S_4 (see Figure 3.7a). When this effect is taken into account in Figure 4.10, the slope of the curve becomes steeper.

4.4.3. Frequency dependence of scintillation

Using the irregularity models described above, it is possible to investigate the frequency dependence of scintillation intensity. This is especially useful to estimate the scintillation intensities at higher frequency radiowaves because radiowaves above UHF band are being used in many satellite communications and control links. Figure 4.11 shows the scintillation index S_4 at three frequencies, 136 MHz, 400 MHz, and 1.5 GHz versus density fluctuation. The thick (L=256 km) and isotropic irregularity model (see Figure 4.10) is assumed. In the range of small density fluctuation, S_4 for all the three

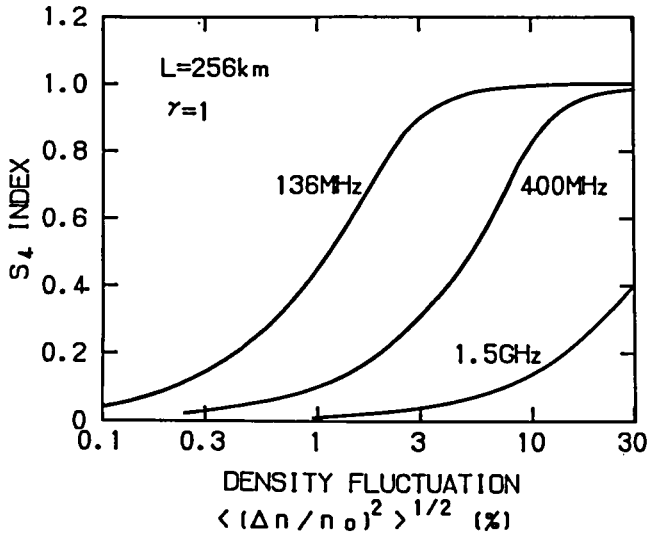

Fig. 4.11. Scintillation index S_4 as a function of electron density fluctuation $<(\Delta n/n_o)^2>^{1/2}$ computed for frequencies 136, 400 MHz, and 1.5 GHz. Thick (256 km) and isotropic irregularity slab is assumed.

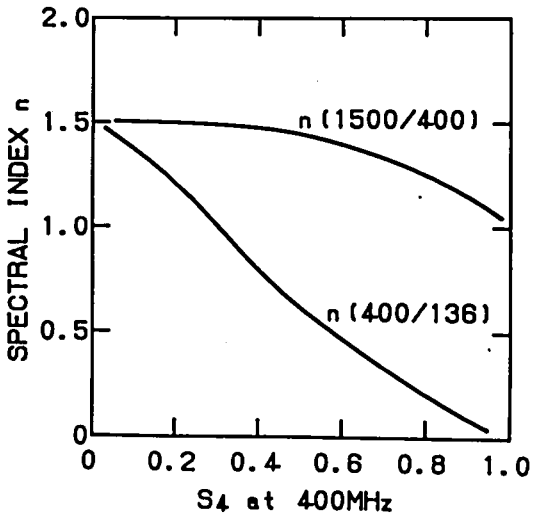

Fig. 4.12. Spectral indices n for two frequencies against the scintillation index S_4. The irregularity conditions are the same as those in Fig. 4.11.

frequencies increase with increasing density fluctuation. As density fluctuation increases, the saturation of the scintillation index becomes apparent, first at lower frequency. When S_4 reaches the saturation level, the frequency dependence of S_4 becomes weak; the difference between S_4s at 136 and 400 MHz becomes small in the range of density fluctuation above 10%. The S_4 index at 1.5 GHz does not reach the saturation but is about 0.4 at the density fluctuation of 30%.

The frequency dependence of S_4 is predicted by the weak scintillation theory, viz., $S_4 \propto f^{-n}$, $n=-(2+p)/4$ (see (1.27)). Where f is the radio frequency and p is the index of the three-dimensional wavenumber spectrum of the irregularities. Namely, the scintillation spectral index n is 1.5 when p=4. Figure 4.12 shows the spectral index n obtained from the difference of S_4 indices between two frequencies in Figure 4.11; two curves of n represent the S_4 ratios between 400 and 136 MHz, and between 1.5 GHz and 400 MHz, respectively. The abscissa is the S_4 index at 400 MHz. The spectral index n of two curves approach 1.5 at the limit of the weak scintillation (S_4=0), in accordance with the above theory. However, n decreases with increasing S_4 at 400 MHz. This means the breakdown of the weak scintillation theory, i.e., the multiple scattering becomes effective. The breakdown appears sooner and more significantly at the lower frequencies (400/136 MHz) than at the higher ones (1500/400 MHz). The spectral index n at 400/136 MHz becomes almost 0 at S_4 (at

400 MHz)=1, which means that S_4s at these two frequencies are almost the same and equal to 1. Namely, the frequency dependence vanishes.

4.5. CONCLUSION

The fourth-order moment equation has been numerically solved for the ionospheric scintillation with a fairly realistic irregularity model. Evolutions of the S_4 index and transverse correlation function were computed and compared with those obtained by spaced-receiver measurement of VHF satellite radiowave scintillations. For power-law irregularities with a spectral index of 4, both thin and thick slabs and both isotropic and anisotropic models were considered. It is found that the effects of these various models on radiowave scattering can be uniquely evaluated by introducing the total phase fluctuation that the radiowave experienced throughout the slab.

In the computation, the decrease in transverse correlation distance due to multiple scattering appeared in the intense scintillation case. This tendency is almost consistent with that obtained from the observation, which suggests that the multiple scattering is also effective in the observed intense scintillations. However, the coincidence between two results was not necessarily complete. In order to resolve the discrepancy

between them, it seems necessary not only to consider the power-law spectrum model of the irregularities with the index around 4, but also to consider two-component spectrum model. In addition, it is necessary to construct a more realistic computation model such as an oblique incidence model to simulate the observation.

The electron density fluctuations necessary for producing a strength of scintillations were estimated. Combining these results with the observed value of the axial ratio, it may be possible to build up a more complete model of fluctuation density. In addition, the frequency dependence of the scintillation intensity was investigated. For the intense scintillation, the frequency dependence of S_4 index becomes weaker than that predicted by the weak scatter theory. The frequency dependence almost vanishes in the frequency range below UHF band for very intense scintillation. These results are useful to evaluate and to predict the effects of the scintillations on the satellite links in practical use.

CHAPTER 5

SUMMARY AND CONCLUSION

The present thesis deals with the observation and analysis of the mid-latitude ionospheric scintillations on VHF satellite radiowave. The emphasis was put on the study of the spatial characteristics of the ionospheric irregularities by means of spaced-receiver observation. In addition, analysis was made for clarifying the mechanism of the radiowave scattering for intense scintillations. In the analysis, comparisons between the strong scatter theory and the observation results were made to construct a possible scintillation model.

In chapter 2, (1) the method of the correlation analysis in the case of two-dimensional anisotropic irregularities was introduced. The form of the irregularities as well as the irregularity drifts can be derived through this analysis. (2) The arrangement of the observation instruments and the practical method of data processing were also shown. (3) It is concluded that accurate drift velocity can not be determined for the irregularities with large axial ratio. In this case, only the component of drift velocity perpendicular to the elongation axis of the irregularities is obtained.

In chapter 3, some results of scintillation measurements

were discussed. (4) The drift velocities obtained were directed mostly northward or southward since the elongation axes of the irregularities projected onto the plane perpendicular to the radio path (the observation plane) were almost always along east-west direction. Mean northward and southward velocities were equally about 25 m/s. (5) The irregularity pattern projected onto the observation plane was ellipse with large axial ratio. The directions of the major axes were coincident well with that of the geomagnetic field line at the F-region height, which suggests that the irregularities are well field-aligned. Mean axial ratio and mean minor radius of the actual ionospheric irregularities were 24 and 180 m, respectively. (6) With increasing S_4, axial ratio increased while minor radius decreased. The latter result suggests that the multiple scattering plays an important role in the production of intense scintillations. (7) In addition, through the observation during a geomagnetic storm, much faster drift velocities and larger indices of the irregularity wavenumber spectrum compared with those under quiet conditions were obtained. Also, it was shown that the drift direction is associated with time variation in the geomagnetism; when the geomagnetic H-component was steeply decreasing, the drift direction reversed from southwestward to north or northeastward.

In chapter 4, the fourth-order moment equation method was applied to the ionospheric scintillation problem and solved numerically. This method proved to be useful to investigate the

intense ionospheric scintillation in which multiple scattering may take place. Some features peculiar to the intense scintillation was successfully interpreted by this theory. Main conclusions in chapter 4 are: (8) decrease in the transverse correlation distance observed during the intense scintillation is well reproduced by the model computation. It is concluded that the multiple scattering effect plays an important role in the intense scintillations observed. (9) The electron density fluctuation necessary to produce a certain degree of scintillation was estimated. It is possible to construct a reasonable model of the irregularities which describes the development of the scintillation. (10) The frequency dependence of the scintillation intensity was investigated in the case that the multiple scattering effect is taken into account. The frequency dependence observed during intense scintillation became weaker than that predicted by the weak scatter theory. These results are useful to evaluate and to predict the effects of the scintillations on satellite links in practical use.

The followings are the future problems to be solved: (1) due to significant elongation of the irregularities along the geomagnetic field lines, it was impossible to obtain irregularity drift component parallel to the elongation in this study. In order to obtain this component more accurately and to clarify the behavior of the irregularities, observations coordinated with other techniques such as radar are necessary. (2) Investigation

of the mechanism of both generation and behavior of the irregularities is left beyond the scope of the present study. It seems an important problem to study the generation mechanism of mid-latitude irregularities and how they relate with equatorial ones. The irregularity characteristics obtained here will give a great help to such studies. (3) In the analysis of the correlation distance using the fourth-order moment equation, a consistency between the theory and observation was not complete enough. It is necessary to examine carefully the observed data and also to construct more realistic computation model such as the two-component spectrum model of the irregularities and oblique incidence model.

REFERENCES

Aarons, J., Global morphology of ionospheric scintillations, Proc. IEEE, 70, 360-378, 1982.

Aarons, J., J.P. Mullen, J.P. Koster, R.F. DaSilva, J.R. Medeiros, R.T. Medeiros, A. Bushby, J. Pantoja, J. Lanat, and M.R. Paulson, Seasonal and geomagnetic control of equatorial scintillations in two longitudinal sectors, J. Atmos. Terr. Phys., 42, 861-866, 1980.

Barabanenkov, Y. N, Y.A. Kravtsov, S.M. Rytov, and V.I. Tatarskii, Status of the theory of propagation of waves in a randomly inhomogeneous medium, Sov. Phys. Uspekhi, 13, 551-575, 1971.

Basu, S. and M.C. Kelley, A review of recent observations of equatorial scintillations and their relationship to current theories of F-region irregularity generation, Radio Sci., 14, 471-485, 1979.

Basu, S. and S. Basu, Equatorial scintillations - a review, J. Atmos. Terr. Phys., 43, 473-489, 1981.

Basu, S., S. Basu, S. Ganguly, and J.A. Klobuchar, Generation of kilometer scale irregularities during the midnight collapse at Arecibo, J. Geophys. Res., 86, 7607-7616, 1981.

Basu, S., S. Basu, J.P. McClure, W.B. Hanson, and H.E. Whitney, High resolution topside in situ data of electron densities and VHF/GHz scintillations in the equatorial region, J. Geophys.

Res., 88, 403-415, 1983.

Behnke, R., F layer height bands in the nocturnal ionosphere over Arecibo, J. Geophys. Res., 84, 974-978, 1979.

Bischoff, K. and B. Chytil, A note on scintillation indices, Planet. Space Sci., 17, 1059-1066, 1969.

Blanc, M., Magnetospheric convection effects at mid-latitudes 1. Saint-Santin observations, J. Geophys. Res., 88, 211-223, 1983.

Booker, H.G. and G. MajidiAhi, Theory of refractive scattering in scintillation phenomena, J. Atmos. Terr. Phys., 43, 1199-1214, 1981.

Booker, H.G., J.A. Ferguson, H.O. Vats, Comparison between the extended-medium and the phase-screen scintillation theories, J. Atmos. Terr. Phys., 47, 381-399, 1985.

Bramley, E.N. and R. Browning, Mid-latitude ionospheric scintillation of geostationary satellite signals at 137 MHz, J. Atmos. Terr. Phys., 40, 1247-1255, 1978.

Briggs, B.H., On the analysis of moving patterns in geophysics-I. Correlation analysis, J. Atmos. Terr. Phys., 30, 1777-1788, 1968.

Briggs, B. H., Ionospheric irregularities and radio scintillations, Contemp. Phys., 1975, 469-488, 1975.

Briggs, B. H., Ionospheric drifts, J. Atmos. Terr. Phys., 39, 1023-1034, 1977.

Briggs, B. H., G.J. Phillips, and D. H. Sinn, The analysis of

observations on spaced receivers of the fading of radio signals, Proc. Phys. Soc., B63, 106-121, 1950.

Briggs, B.H. and I.A. Parkin, On the variation of radio star and satellite scintillations with zenith angle, J. Atmos. Terr. Phys., 25, 339-365, 1963.

Brown, W.P., Jr., Moment equations for wave propagated in random media, J. Opt. Soc. Am., 62, 45-54, 1972a.

Brown, W.P., Jr., Fourth moment of a wave propagating in a random medium, J. Opt. Soc. Am., 62, 966-971, 1972b.

Costa, E. and M. C. Kelley, Linear theory for the collisionless drift wave instability with wavelengths near the ion gyroradius, J. Geophys. Res., 83, 4365-4368, 1978.

Crain, C. M., H. G. Booker, and J. A. Ferguson, Use of refractive scattering to explain SHF scintillations, Radio Sci., 14, 125-134, 1979.

Crane, R. K., Spectra of ionospheric scintillation, J. Geophys. Res., 81, 2041-2050, 1976.

Crane, R.K., Ionospheric scintillation, Proc. IEEE, 65, 180-199, 1977.

Cronyn, W. M., The analysis of radio scattering and space-probe observations of small-scale structure in the interplanetary medium, Astrophys. J., 161, 755-763, 1970.

Das Gupta, A. and L. Kersley, Summer daytime scintillation and sporadic-E, J. Atmos. Terr. Phys., 38, 615-618, 1976.

Dyson, P.L., J.P. McClure, and W.B. Hanson, In situ measurements

of the spectral characteristics of F region ionospheric irregularities, J. Geophys. Res., 79, 1497-1502, 1974.

Evans, J. V., Observation of F region vertical velocities at Millstone Hill, 1, evidence for drifts due to expansion, contraction, and winds, Radio Sci., 6, 609-626, 1971.

Fejer, B. G. and M. C. Kelley, Ionospheric irregularities, Rev. Geophys. Space Phys., 18, 401-454, 1980.

Franke, S.J. and C.H. Liu, Observations and modeling of multi-frequency VHF and GHz scintillations in the equatorial region, J. Geophys. Res., 88, 7075-7085, 1983.

Franke, S.J. and C.H. Liu, Modeling of equatorial multifrequency scintillation, Radio Sci., 20, 403-415, 1985.

Fujita, M., K. Sinno, and T. Ogawa, Frequency dependence of ionospheric scintillations and its application to spectral estimation of electron density irregularities, J. Atmos. Terr. Phys., 44, 13-18, 1982.

Gozani, J., Numerical solution for the fourth-order coherence function of a plane wave propagating in a two-dimensional Kolmogorovian medium, J. Opt. Soc. Am., A2, 2144-2151, 1985.

Karasawa, Y., K. Yasukawa, and M. Yamada, Ionospheric scintillation measurements at 1.5 GHz in mid-latitude region, Radio Sci., 20, 643-651, 1985.

Kent, G.S. and J.R. Koster, Some studies of night-time F-layer irregularities at the equator using very high frequency signals radiated from earth satellites, Ann. Geophys., 22,

405-417, 1966.

Kersley, L., J. Aarons, and A. Klobuchar, Nighttime enhancements in Total electron content near Arecibo and their association with VHF scintillations, J. Geophys. Res., 85, 4214-4222, 1980.

Koster, J. R., Some measurements of the irregularities giving rise to radio-star scintillations at the equator, J. Geophys. Res., 68, 2579-2590, 1963.

Kumagai, H., Mid-latitude ionospheric scintillations and geomagnetic activity, J. Geomag. Geoelectr., 38, 267-274, 1986.

Kumagai, H., Spatial correlations in intense ionospheric scintillations: comparison between numerical computation and observation, Radio Sci., 22, 439-448, 1987.

Kumagai, H. and T. Ogawa, Behavior of mid-latitude F-region irregularities deduced from spaced-receiver VHF scintillation measurements, J. Atmos. Terr. Phys., 48, 221-230, 1986.

Kumagai, H., T. Ogawa, and T. Hori, Solar-terrestrial disturbances of June-September 1982, IV.12. Ionospheric scintillations of geostationary satellite radio waves, J. Radio Res. Lab., 33, Special Issue No. 1, 257-268, 1986.

Liu, C.H., A.W. Wernik, K.C. Yeh, and M.Y. Youakim, Effects of multiple scattering on scintillation of transionospheric radio signals, Radio Sci., 9, 599-607, 1974.

Liu, C.H. and K.C. Yeh, Frequency and spatial correlation

functions in a fading communication channel through the ionosphere, Radio Sci., 10, 1055-1061, 1975.

MacDaugall, J. W., Distributions of the irregularities which produce ionospheric scintillations, J. Atmos. Terr. Phys., 43, 317-325, 1981.

Minakoshi, H., K. Sinno, M. Kan, H. Kurihara, and O. Furuta, Severe ionospheric scintillations associated with magnetic storm on March 22, 1979, J. Radio Res. Lab., 28, 1-9, 1981.

Moorcroft, D. R. and K.S. Arima, The shape of the F-region irregularities which produce satellite scintillations - evidence for axial asymmetry, J. Atmos. Terr. Phys., 34, 437-450, 1972.

Ogawa, T., Solar-terrestrial disturbances of June-September 1982, III. Solar flares, flare particles and geomagnetic storms, J. Radio Res. Lab., 33, Special Issue No. 1, 23-48, 1986.

Ogawa, T., K. Sinno, M. Fujita, and J. Awaka, Severe disturbances of VHF and GHz waves from geostationary satellite during a magnetic storm, J. Atmos. Terr. Phys., 42, 637-644, 1980.

Ogawa, T. and H. Kumagai, Deep depletions of total electron content associated with severe mid-latitude gigahertz scintillations during geomagnetic storms, J. Geophys. Res., 90, 6652-6656, 1985.

Oyama, K. I., T. Kaneko, K. Hirao, and T. Okuzawa, Study of equatorial scintillation using equator-orbiting satellite HINOTORI, Bul. Insti. Space Astronautical Sci., S.P. No. 9,

27-44, March, 1984 (in Japanese).

Perkins, F., Spread-F and ionospheric currents, J. Geophys. Res., 78, 218-226, 1973.

Phillips, G.J. and M. Spencer, The effects of anisometric amplitude patterns in the measurement of ionospheric drifts, Proc. Phys. Soc., B68, 481-492, 1955.

Reddi, C. R., K. K. Moorthy, and B.V.K. Murthy, Signal statistics of equatorial nighttime ionospheric scintillations, Radio Sci., 15, 1001-1007, 1980.

Rino, C. L. and E. J. Fremouw, Statistics for ionospherically diffracted VHF/UHF signals, Radio Sci., 8, 223-233, 1973.

Rino, C.L. and E.J. Fremouw, The angle dependence of singly scattered wavefields, J. Atmos. Terr. Phys., 39, 859-868, 1977.

Rino, C. L. and S. J. Matthews, On the morphology of auroral zone radio wave scintillation, J. Geophys. Res., 85, 4139-4151, 1980.

Rufenach, C.L., Power-law wavenumber spectrum deduced from ionospheric scintillation observations, J. Geophys. Res., 77, 4761-4772, 1972.

Salpeter, E. E., Interplanetary scintillations. I. theory, Astrophys. J., 147, 433-448, 1967.

Sinno, K. and M. Kan, Mid-latitude ionospheric scintillations of VHF radio signals associated with peculiar fluctuations of Faraday rotation, J. Atmos. Terr. Phys., 40, 503-506, 1978.

Sinno, K. and M. Kan, Ionospheric scintillation and fluctuation of Faraday rotation caused by spread-F and sporadic-E over Kokubunji, Japan, J. Radio Res. Lab., 27, 53-77, 1980.

Sinno, K. and H. Minakoshi, Experimental results on satellite scintillations due to field-aligned irregularities at mid-latitudes, J. Atmos. Terr. Phys., 45, 563-567, 1983.

Tanaka, T., Severe ionospheric disturbances caused by the sudden response of evening subequatorial ionospheres to geomagnetic storms, J. Geophys. Res., 86, 11335-11349, 1981.

Tatarskii, V. I., Wave propagation in a turbulent medium, Eq. (6-34), McGraw-Hill Book Co., New York, 1961.

Tatarskii, V.I., Light propagation in a medium with random refractive index inhomogeneities in the Markov random process approximation, Sov. Phys. JETP, 29, 1133-1138, 1969.

Tatarskii, V.I., The effects of the turbulent atmosphere on wave propagation, 426 pp., US Department of Commerce, National Technical Information Service, Springfield, Va., 1971.

Taylor, G. N., Meridional F2-region plasma drifts at Malvern, J. Atmos. Terr. Phys., 36, 267-286, 1974.

Ueda, S., M. Matuo, M. Sato, Y. Momoi, T. Abe, K. Ide, K. Tachibana, Ionospheric scintillation which disturbed the GMS-2 communication link, Meteorological Satellite Center Tech. Note, No. 7, 29-38, 1983 (in Japanese).

Umeki, R., C.H. Liu, and K.C. Yeh, Multifrequency spectra of ionospheric amplitude scintillations, J. Geophys. Res., 82,

2752-2760, 1977a.

Umeki, R., C.H. Liu, and K.C. Yeh, Multifrequency studies of ionospheric scintillations, Radio Sci., 12, 311-317, 1977b.

Vats, H.O., On the multiple scattering of VHF/UHF waves in the equatorial ionosphere, Radio Sci., 16, 393-398, 1981.

Wernik, A. W., and C. H. Liu, Ionospheric irregularities causing scintillation of GHz frequency radio signals, J. Atmos. Terr. Phys., 36, 871-879, 1974.

Whitney, H. E. and S. Basu, The effect of ionospheric scintillation on VHF/UHF satellite communications, Radio Sci., 12, 123-133, 1977.

Wernik, A. W., C. H. Liu, and K. C. Yeh, Modeling of spaced-receiver scintillation measurements, Radio Sci., 18, 743-764, 1983.

Woodman, R. F. and C. La Hoz, Radar observations of F region equatorial irregularities, J. Geophys. Res., 81, 5447-5466, 1976.

Wright, J. W. and M.L.V. Pitteway, Computer simulation of ionospheric radio drift measurements, and their analysis by correlation methods, Radio Sci., 13, 189-210, 1978.

Yeh, K.C., C.H. Liu, and M.Y. Youakim, A theoretical study of the ionospheric scintillation behavior caused by multiple scattering, Radio Sci., 10, 97-106, 1975.

Yeh, K. C., J. P. Mullen, J.R. Medeiros, R. F. DaSilva, and R.T. Medeiros, Ionospheric scintillation observations at Natal, J.

Geophys. Res., 86, 7527-7532, 1981.

Yeh, K.C. and C.H. Liu, Radio wave scintillations in the ionosphere, Proc. IEEE, 70, 324-360, 1982.

APPENDIX A. DERIVATION OF EQUATIONS (2.29) AND (2.30)

The general equation of an ellipsoid centered on the origin is given by (2.27) as

$$ax^2 + 2hxy + by^2 + 2fx\tau + 2gy\tau + c\tau^2 = 1 \qquad (A.1)$$

This ellipsoid is shown in Figure 2.3. We require the equation of the ellipse which intersects the ellipsoid with a plane containing the τ-axis and making an angle χ with τOx. Let the coordinate of length in this plane be ℓ. Then

$$\begin{aligned} x &= \ell \cos\chi \\ y &= \ell \sin\chi \end{aligned} \qquad (A.2)$$

Substituting (A.2) into (A.1) we have

$$\ell^2(a\cos^2\chi + 2h\cos\chi\sin\chi + b\sin^2\chi) + 2\ell\tau(f\cos\chi + g\sin\chi) + c\tau^2 = 1 \qquad (A.3)$$

The equations of three ellipses which are formed on the plane containing τ-axis and three pairs of antenna baselines are given by (2.26)

$$a_i\ell^2 + 2h_i\ell\tau + b_i\tau^2 = 1 \qquad (A.4)$$

where i=1- 3. Comparison between (A.3) and (A.4) gives

$$\begin{cases} a_1 = a\cos^2\chi_1 + 2h\cos\chi_1\sin\chi_1 + b\sin^2\chi_1 \\ a_2 = a\cos^2\chi_2 + 2h\cos\chi_2\sin\chi_2 + b\sin^2\chi_2 \\ a_3 = a\cos^2\chi_3 + 2h\cos\chi_3\sin\chi_3 + b\sin^2\chi_3 \end{cases} \qquad (A.5)$$

$$\begin{cases} h_1 = f\cos\chi_1 + g\sin\chi_1 \\ h_2 = f\cos\chi_2 + g\sin\chi_2 \\ h_3 = f\cos\chi_3 + g\sin\chi_3 \end{cases} \qquad (A.6)$$

Using matrix notation, (A.5) may be rewritten as

$$\mathbf{a} = \mathbf{A}\,\mathbf{r} \tag{A.7}$$

where

$\mathbf{a} = [a_1, a_2, a_3]$ a column vector

$\mathbf{r} = [a, 2h, b]$ a column vector

The elements of **A** are shown in (2.28). (2.30) can be derived from (A.6).

APPENDIX B. SOLUTION OF EQUATION (4.5)

A method to solve the equation (4.5) is described following Liu et al. [1974]. The subscript 4 attached to Γ_4 is omitted hereafter. First, (4.5) is integrated over ζ, then

$$\Gamma(\xi, \eta, \zeta) = \exp[g(\xi, \eta)\zeta] - j\int_0^{\zeta} \exp[-g(\xi, \eta)(\zeta' - \zeta)\frac{\partial^2 \Gamma}{\partial \xi \partial \eta} d\zeta' \qquad (B.1)$$

This is a solution inside the irregularity slab, where $0 < \zeta < \zeta_0$ ($\zeta_0 = L / k r_0^2$). Let

$$\xi = i\Delta\xi, \quad \eta = k\Delta\eta, \quad \zeta = n\Delta\zeta, \quad \text{and } g(i\Delta\xi, k\Delta\eta) = a_{ik}$$

Using a trapezoidal rule in the integration over ζ', the second term ($= I_n$) in the right hand of (B.1) at (i,j,k) is expressed as (i and k are omitted if no confusion)

$$I_n = -j \exp[a_n \Delta\zeta] \cdot [\tfrac{1}{2}\Delta\zeta (h_n + h_{n-1}) + \tfrac{1}{2}\Delta\zeta (h_{n-1} + h_{n-2}) + \tfrac{1}{2}\Delta\zeta (h_{n-2} + h_{n-3}) + \cdots\cdots\cdots + \tfrac{1}{2}\Delta\zeta (h_2 + h_1)] \qquad (B.2)$$

where

$$h_n = \exp[-a\,n\Delta\zeta]\,\frac{\partial^2\Gamma_n}{\partial\xi\,\partial\eta} \tag{B.3}$$

Similarly, at (i,k,n-1)

$$\begin{aligned} I_{n-1} &= -j\exp[a\,(n-1)\,\Delta\zeta] \\ &\quad\cdot[\tfrac{1}{2}\Delta\zeta\,(h_{n-1}+h_{n-2}) + \tfrac{1}{2}\Delta\zeta\,(h_{n-2}+h_{n-3}) \\ &\quad + \cdots\cdots\cdots + \tfrac{1}{2}\Delta\zeta\,(h_2+h_1)] \end{aligned} \tag{B.4}$$

Combination of (B.2) with (B.4) makes

$$\begin{aligned} & I_n - I_{n-1}\exp[a\Delta\zeta] \\ &= -j\exp[a\,n\Delta\zeta]\;[\tfrac{1}{2}\Delta\zeta\,(h_n+h_{n-1})] \\ &= -j\,\tfrac{1}{2}\Delta\zeta\,\left[\frac{\partial^2\Gamma_n}{\partial\xi\,\partial\eta} + \exp(a\Delta\zeta)\,\frac{\partial^2\Gamma_{n-1}}{\partial\xi\,\partial\eta}\right] \end{aligned} \tag{B.5}$$

(B.5) can be rewritten as

$$I_n + j\,\tfrac{1}{2}\Delta\zeta\,\frac{\partial^2\Gamma_n}{\partial\xi\,\partial\eta} = \exp(a\Delta\zeta)\;\left(\Gamma_{n-1} - j\,\tfrac{1}{2}\Delta\zeta\,\frac{\partial^2\Gamma_{n-1}}{\partial\xi\,\partial\eta}\right) \tag{B.6}$$

Using the difference notation

$$\frac{\partial^2\Gamma_n}{\partial\xi\,\partial\eta} = \frac{1}{4\Delta\xi\Delta\eta}\,[\Gamma_{i+1,k+1,n} - \Gamma_{i-1,k+1,n} - \Gamma_{i+1,k-1,n} + \Gamma_{i-1,k-1,n}] \tag{B.7}$$

$\dfrac{\partial^2\Gamma_{n-1}}{\partial\xi\,\partial\eta}$ can be also expressed in the similar form. Substitution

of them into (B.6) yields

$$j\mu\Gamma_{i+1,k+1,n} - j\mu\Gamma_{i+1,k-1,n} + \Gamma_{i,k,n} - j\mu\Gamma_{i-1,k+1,n} + j\mu\Gamma_{i-1,k-1,n}$$
$$= \exp(-a_{ik}\Delta\zeta)\ [j\mu\Gamma_{i+1,k+1,n-1} - j\mu\Gamma_{i+1,k-1,n-1} - \Gamma_{i,k,n-1}$$
$$- j\mu\Gamma_{i-1,k+1,n-1} + j\mu\Gamma_{i-1,k-1,n-1}] \qquad (B.8)$$

where

$$\mu = \Delta\zeta / 8\Delta\xi\Delta\eta$$

Here, the initial condition is

$$\Gamma(\xi, \eta, 0) = 1 \qquad (B.9)$$

The boundary conditions are

$$\Gamma(\xi\to\infty, \eta, \zeta) = \exp[g(\xi\to\infty, \eta)\zeta]$$
$$\Gamma(\xi, \eta\to\infty, \zeta) = \exp[g(\xi, \eta\to\infty)\zeta] \qquad (B.10)$$

Next, the solution in the neutral atmosphere ($\zeta > \zeta_0$) is considered. The integration of (4.5) over ζ gives

$$\Gamma(\xi, \eta, \zeta) = \Gamma(\xi, \eta, \zeta_0) - j\int_{\zeta_0}^{\zeta} \frac{\partial^2\Gamma}{\partial\xi\,\partial\eta}\, d\zeta' \qquad (B.11)$$

By using the similar procedure, the final form corresponding to (B.8) becomes

$$j\mu\Gamma_{i+1,k+1,n} - j\mu\Gamma_{i+1,k-1,n} + \Gamma_{i,k,n} - j\mu\Gamma_{i-1,k+1,n} + j\mu\Gamma_{i-1,k-1,n}$$

$$= - [\, j\mu \Gamma_{i+1,k+1,n-1} - j\mu \Gamma_{i+1,k-1,n-1} - \Gamma_{i,k,n-1} + j\mu \Gamma_{i-1,k+1,n-1}$$

$$+ j\mu \Gamma_{i-1,k-1,n-1} \,] \qquad \text{(B. 12)}$$

The initial condition in this case is

$$\Gamma^N(\xi,\ \eta,\ \zeta_0) = \Gamma^I(\xi,\ \eta,\ \zeta_0) \qquad \text{(B. 13)}$$

where N and I mean Γ in the neutral atmosphere and ionosphere, respectively. The boundary conditions are the same as those in the former case.

Define a vector $\boldsymbol{\Gamma}$ by

$$\boldsymbol{\Gamma} = [\Gamma_{1,1,n}\ \ \Gamma_{1,2,n}\ \cdots\cdots\ \Gamma_{1,k,n}\ \ \Gamma_{2,1,n}\ \cdots\cdots$$

$$\Gamma_{2,k,n}\ \cdots\cdots\ \Gamma_{i,1,n}\ \cdots\cdots\ \Gamma_{i,k,n}\,] \qquad \text{(B. 14)}$$

Equation (B.8) or (B.12) together with (B.10) can be rearranged in the matrix form as

$$\mathbf{A}\boldsymbol{\Gamma} = \mathbf{D} \qquad \text{(B. 15)}$$

where $\mathbf{A}$ is a tridiagonal block matrix given as

$$\mathbf{A} = \begin{pmatrix}
\mathbf{a} & \mathbf{c} & 0 & & & & & & & & \\
\mathbf{b} & \mathbf{a} & \mathbf{c} & 0 & & & & & & & \\
0 & \mathbf{b} & \mathbf{a} & \mathbf{c} & 0 & & & & 0 & & \\
 & 0 & \mathbf{b} & \mathbf{a} & \mathbf{c} & 0 & & & & & \\
 & & \cdot & \cdot & \cdot & \cdot & \cdot & & & & \\
 & & & \cdot & \cdot & \cdot & \cdot & \cdot & & & \\
 & & & & \cdot & \cdot & \cdot & \cdot & \cdot & & \\
 & & & & & 0 & \mathbf{b} & \mathbf{a} & \mathbf{c} & 0 & \\
 & & 0 & & & & 0 & \mathbf{b} & \mathbf{a} & \mathbf{c} & 0 \\
 & & & & & & & 0 & \mathbf{b} & \mathbf{a} & \mathbf{c} \\
 & & & & & & & & 0 & \mathbf{b} & \mathbf{a}
\end{pmatrix} \qquad \text{(B. 16)}$$

and

$$\mathbf{a} = \mathbf{I}$$

$$\mathbf{b} = \begin{pmatrix} 0 & -j\lambda & 0 & & & & & & & & & & \\ j\lambda & 0 & -j\lambda & 0 & & & & & & & & & \\ 0 & j\lambda & 0 & -j\lambda & 0 & & & & & & 0 & & \\ & 0 & j\lambda & 0 & -j\lambda & 0 & & & & & & & \\ & & \cdot & \cdot & \cdot & \cdot & \cdot & & & & & & \\ & & & \cdot & \cdot & \cdot & \cdot & \cdot & & & & & \\ & & & & \cdot & \cdot & \cdot & \cdot & \cdot & & & & \\ & & & & & 0 & j\lambda & 0 & -j\lambda & 0 & & & \\ & & 0 & & & & 0 & j\lambda & 0 & -j\lambda & 0 & & \\ & & & & & & & 0 & j\lambda & 0 & -j\lambda & & \\ & & & & & & & & 0 & j\lambda & 0 & & \end{pmatrix} \qquad \text{(B.17)}$$

$$\mathbf{c} = -\mathbf{b}$$

The dimensions of $\mathbf{a}$, $\mathbf{b}$, $\mathbf{c}$ and hence $\mathbf{A}$ depend on both mesh sizes and boundary limits along ξ and η directions. In the present computation, for ξ and η extending to ± 2.4 and mesh sizes of $\Delta\xi = \Delta\eta = 0.025$, $\mathbf{a}$, $\mathbf{b}$, and $\mathbf{c}$ become 191×191 matrices. $\mathbf{D}$ in (B.15) is a vector that includes both the solution of Γ at the (n-1)th step, $\Gamma_{i,k,n-1}$, and the boundary values. (B.15) is solved by the recursion technique valid for tridiagonal block matrices.

APPENDIX C. DERIVATION OF EQUATIONS (4.12) AND (4.13)

$u(\boldsymbol{\rho},z)$ is a random complex amplitude of the wave propagating in z direction. $\boldsymbol{\rho}$ is relative transverse coordinate [Brown, 1972b]. If one consider two-dimensional space, $u(\boldsymbol{\rho},z) = u(\rho,z)$ without loss of generality. As is given in (1.25), S_4 is defined by

$$S_4^2 = \frac{\langle I^2\rangle - \langle I\rangle^2}{\langle I\rangle^2} \tag{C.1}$$

where, I is the signal intensity. S_4 is evaluated at $(0,\zeta)$ and is given by

$$S_4^2 = \frac{\langle (u(0)\,u^*(0))^2\rangle - \langle u(0)\,u^*(0)\rangle^2}{\langle u(0)\,u^*(0)\rangle^2} \tag{C.2}$$

where we use $u(0)$ in place of $u(0,\zeta)$. In the present study, only the case of $\langle u(\rho)u^*(\rho)\rangle=1$ is taken into consideration, namely, u is the normalized amplitude. Comparison between (4.4) and (C.2) makes $\rho_1=\rho_2=\rho_3=\rho_4=0$, which is reduced to $\alpha=\beta=0$. Then, the following equation is derived

$$S_4^2 = \Gamma_4(0,0,\zeta) - 1 \tag{4.12}$$

Next, the cross-correlation function between two points $(0,\zeta)$ and (ξ,ζ) is given as

$$C_1 = \frac{\langle \{u(0)u^*(0) - \langle u(0)u^*(0)\rangle\}\{u(\xi)u^*(\xi) - \langle u(\xi)u^*(\xi)\rangle\}\rangle}{\langle \{u(0)u^*(0) - \langle u(0)u^*(0)\rangle\}^2\rangle} \tag{C.3}$$

Comparison with (4.4) makes $\rho_1=\rho_2=0$ and $\rho_3=\rho_4=\xi$, which is reduced to $\alpha=0$ and $\beta=\xi$. Therefore, following relation is derived.

$$C_1 = \{\Gamma_4(0, \xi, \zeta) - 1\} / S_4^2 \tag{4.13}$$